Dissertation
submitted to the
Combined Faculties for the Natural Sciences and for Mathematics
of the Ruperto-Carola University of Heidelberg, Germany
for the degree of
Doctor of Natural Sciences

presented by

Robert Fischer
born in Kenzingen, Germany

Oral examination: July 4$^{\text{th}}$, 2007

Optimization of high-order harmonic generation in laser-driven atomic and molecular systems

Referees: Prof. Dr. C. H. Keitel
Prof. Dr. P. Schmelcher

Zusammenfassung

Wenn ein Atom oder ein Molekül einem starken Laserpuls ausgesetzt wird, führt ein Rekollisions-Rekombinationsmechanismus zur Emission Hoher-Harmonischer-Strahlung, die Vielfache der eingestrahlten Laserfrequenz enthält. Diese Strahlung ist heutzutage die Grundlage für das hochaktuelle Forschungsgebiet der Attosekundenphysik. Das Lasermagnetfeld ist verantwortlich für eine Driftbewegung in Laserpropagationrichtung von ionisierten Wellenpaketen. Im Zusammenhang mit einem ersten Projekt dieser Arbeit hat sich herausgestellt, dass sich die harmonische Strahlung, die aufgrund dieser Driftbewegung entsteht, leicht mit Hilfe eines zusätzlichen, relativ schwachen statischen Magnetfeldes beeinflussen lässt.
In einem zweiten Projekt wird ein neuartiger Mechanismus vorgeschlagen, der in der Kombination der Driftbewegung in Laserpropagationsrichtung mit Eigenschaften antisymmetrischer Orbitale besteht. In einem Bereich hoher Laserintensitäten wird gezeigt, dass eine effiziente Hohe-Harmonische-Erzeugung ohne die gängigen Einschränkungen aufgrund der Driftbewegung in Laserpropagationsrichtung möglich ist. Aus einem anderen Blickwinkel heraus kann man sagen, dass zum ersten Mal gezeigt wurde, dass diese Driftbewegung zu einem Anstieg der Intensität der Harmonischen führen kann. Die wichtigsten Ergebnisse sind durch numerische Integration der zeitabhängigen Schrödinger-Gleichung erhalten worden.

Abstract

When an atom or a molecule is subject to a strong laser pulse a recollision-recombination mechanism gives rise to the emission of high-order harmonic radiation containing frequency multiples of the irradiating laser field. This radiation is nowadays the basis for the highly active research field of attosecond physics. The laser magnetic field is responsible for the drift of ejected electron wave packets in the laser propagation direction. In the context of the first project of this thesis, it has been found that the harmonic radiation which is induced by this drift motion can be sensitively influenced by means of an additional relatively weak static magnetic field.
In the second project, a novel mechanism is proposed which combines the drift in the laser propagation direction with the properties of antisymmetric orbitals. In a regime of high laser intensities, efficient high-order harmonic generation is proven to be possible without the common limitations due to the drift in the laser propagation direction. From a different viewpoint, it has been shown for the first time that this drift leads to an increase in harmonic intensity. The main results have been obtained by numerical integration of the time-dependent Schrödinger equation.

In connection with this thesis, the following articles were published in refereed journals:

- R. Fischer, M. Lein, and C. H. Keitel: *Enhanced recollisions for antisymmetric molecular orbitals in intense laser fields*
  Phys. Rev. Lett. **97**, 143901 (2006).
- R. Fischer, M. Lein, and C. H. Keitel: *Strongly enhanced high-harmonic generation via antisymmetric ionic states*
  J. Phys. B **40**, F113 (2007).
- R. Fischer, C. H. Keitel, R. Jung, G. Pretzler, and O. Willi: *Impact of a static magnetic field on high-order harmonic spectra*
  Phys. Rev. A **75**, 033401 (2007).

Accepted article:

- R. Fischer, M. Lein, and C. H. Keitel: *Enhanced recollision dynamics via the combination of antisymmetric wave functions and beyond-dipole effects*
  accepted by J. Mod. Opt. (2007).

Contents

Chapter 1

Introduction

In recent years laser technology has made tremendous progress. Novel laser systems permit the generation of short laser pulses with intensities in the range of $10^{14}\,\mathrm{W/cm^2}$-$10^{19}\,\mathrm{W/cm^2}$ as a standard [1]. Two technical advances with respect to the generation of high-intensity pulses were the development of the chirped pulse amplification [2] and the self-mode-locked Ti:sapphire laser [3]. In the near future, novel free-electron-laser technology is expected to provide intense laser pulses in the high-frequency (keV) regime [4]. In addition to higher intensities, there have also been accomplishments with respect to the tailoring of short pulses (only few cycles) [5]. Recently, the generation and characterization of attosecond light pulses has made tremendous progress [6]. Conceivable applications of attosecond pulses consist of the time-resolved monitoring of atomic and molecular processes [7].
The enormous development in laser technology has given impetus to many fields.
For example, it has pushed the field of laser-plasma interactions [8]. The investigation of very intense laser pulses with clusters [9] and solids [10] has been possible. Much progress has been made in understanding the fundamental interactions of intense laser fields with atoms [11] and molecules [12]. As a result, prominent nonlinear phenomena, which are still of current interest, like *above-threshold-ionization (ATI)* [13] and *high-order harmonic generation (HHG)* [14] could be experimentally investigated. Also electron-electron correlation effects which are due to the interaction of several electrons, like nonsequential double ionization, could be studied [15].

From a theoretical point of view, a variety of methods has been developed to describe laser-matter interactions. These methods include time-dependent Hartree-Fock computations [16], density functional theory [17], classical approaches [18] and Floquet methods [19].

The focus of this theoretical thesis is on high-order harmonic generation. HHG has turned out to provide a coherent light source, in which multiples of the irradiating laser frequency are gained - even attaining the sub-Ångström regime [20]. This possibility to generate radiation of extremely short wavelengths has potential to investigate biological, chemical,

molecular and atomic reactions with unprecedented resolution [21]. At present, high-harmonic radiation is employed as a tool to generate attosecond pulses [6]. This renders new fundamental pump-probe experiments possible.

HHG occurs upon the ionization of an atom or a molecule in the laser field. Ionized electrons may be driven back towards the mother ion by the laser field. The electron may then recollide with its mother ion. During this recollision the electron can recombine into the initial bound state under emission of radiation which contains multiples of the irradiating laser frequency. In the context of the theoretical investigation of HHG, there are mainly two established approaches. One is the Lewenstein model which is based on the strong-field approximation (SFA) [22]. The other consists in the direct numerical integration of the time-dependent Schrödinger equation (TDSE). This method is applied in this thesis. Pioneering work for the direct numerical solution of the TDSE can be found in [23]. Besides these two methods, there is a simple intuitive semi-classical picture of the three-step process behind HHG [24].
However, despite the success of the direct numerical integration of the TDSE this approach is still not viable if all three space dimensions are to be taken into account for low-frequency high-intensity laser pulses for which large grids are required. In spite of the enormous developments of computer technology, a full 3D solution for all regimes of laser parameters even for one particle (electron) is still not feasible. Nonetheless, work towards a full three-dimensional integration (but still for high-frequency pulses) has been recently carried out in [25]. As an alternative to full 3D simulations, reducing the dimensions of the corresponding physical model has turned out to be efficient. One-dimensional models have been successfully applied in order to describe ionization of hydrogen-like atoms for lower laser intensities [26].
For increasing laser intensities, however, ionized electrons do not move only in the laser polarization direction of the applied laser pulse but also exhibit a drift in the laser propagation direction. This means that a one-dimensional model is not sufficient anymore for the numerical integration.
Therefore, 2D models that span the laser polarization and propagation direction have been successfully used for intensities up to $10^{18}\,\mathrm{W/cm}$ [27]. Higher laser intensities require a full relativistic treatment, which implies the solution of the Dirac equation [28] or an expansion of it [29].

The electron motion in the laser propagation direction is induced by the laser magnetic field. This motion plays a key role in the research of this thesis. Hence, the TDSE is solved numerically on a two-dimensional grid in order to study high-order harmonic generation. This electron motion gives rise to the emission of harmonic radiation polarized in the laser propagation direction. Relatively little work has been dedicated to this radiation, with most attention being paid to the ordinary harmonic radiation which is polarized in the laser polarization direction.
In the first project, the impact of a static magnetic field on the harmonic radiation polarized in the laser propagation direction is investigated. It is found that an increase or a decrease in the harmonic signal is obtained, depending on the harmonic orders con-

sidered. These changes in the harmonic spectra are significant for relatively weak static magnetic fields of the order of 30T. Other attempts to influence the harmonic radiation polarized in the laser polarization direction require significantly stronger static magnetic fields (on the order of thousands of Tesla). The results of this project suggest that HHG in the laser propagation direction would be a useful tool to measure static magnetic fields.

A further consequence of the electron drift in the laser propagation direction is that the recollision on which HHG is based is hampered by the displacement of the returning electron in the laser propagation direction. As a result, harmonic emission is reduced. In view of the fact that not only HHG but also above-threshold ionization and nonsequential double ionization are recollision-related effects, a solution to this problem is desirable. Several solutions have been proposed which consist in employing pre-accelerated particles [30], tailoring the applied laser pulse [31], using crossed laser fields [32] or choosing particular systems such as positronium [33].

In the second project of this thesis a new solution is attempted. The properties of antisymmetric wave functions exposed to a strong laser pulse are employed in order to counteract the electron drift in the laser propagation direction. As a result, the combination of a drift due to antisymmetry and the drift induced by the laser magnetic field is shown to result in an enhanced recollision dynamics and an increased harmonic signal up to several orders of magnitude. This mechanism is studied for the first excited antisymmetric state of H_2^+ and atomic ions. In the case of H_2^+, the question of a maximum harmonic yield with respect to an optimal combination of both drifts is addressed. Furthermore, it is shown that for the first excited antisymmetric state of H_2^+ exposed to very high laser intensities there is no alignment of the molecule prior to the interaction with the strong laser pulse required, while for weaker intensities pre-alignment is necessary. But this is not a problem because the simulations show that the mechanism for enhancing HHG by means of the compensation of both drifts is efficient for a wide range of orientations of the molecule. Thus, no strict pre-alignment is required. In the case of antisymmetric orbitals of hydrogen-like ions the selection of the appropriate orbital can be accomplished by means of a suitable pre-pulse.

This thesis is structured as follows: In chapter (2) the basics which are relevant for the research presented in this thesis are discussed. Chapter (3) is dedicated to the discussion of the model which is employed to describe the interaction of an atom or molecule with a strong laser pulse. The numerical methods applied in this thesis are also elaborated upon in this chapter. Chapter (4) presents the results of the first project in which the impact of a static magnetic field on the harmonic radiation polarized in the laser propagation direction is investigated. It starts with a survey of studies which focus on the influence of static magnetic fields on high-order harmonic generation before the results obtained in the context of this thesis are presented. The mechanism for enhancing recollisions and HHG via a combination of the properties of antisymmetric orbitals and the electron drift in the laser propagation direction is proposed and investigated in chapter (5). Results for antisymmetric orbitals of H_2^+ and hydrogen-like ions are presented. Novel effects in

two-center interference structures in H_2^+-spectra are illustrated as an outlook for future work.

Note that, unless indicated otherwise, atomic units (a.u.) are used throughout this thesis.

Chapter 2

Fundamental processes in laser-matter interaction

2.1 Free electrons in the laser field

With the advent of high-power lasers it is nowadays possible to investigate interactions of extremely intense laser pulses with matter. These very high laser intensities permit to study the quantum dynamics of electrons ejected in a relativistic regime (see first ref. in [11]). After ionization of atoms or molecules the ejected electrons move in a quasi-free manner in the laser field. Whether the electron moves relativistically depends on the electron velocity in comparison with the speed of light. This depends again on the intensity of the applied laser field which is responsible for the acceleration of the electron. The electron drift in the laser propagation direction which is induced by the laser magnetic field is in the focus of this thesis. As we see in the following, this drift arises from the impact of the Lorentz force and it can be considered as a relativistic effect of first order in v/c, where v denotes the velocity of the electron and c the speed of light. The investigation of higher-order relativistic effects or full relativistic dynamics is not intended. For work on this topic, see first ref. in [11]. By appropriate choice of the laser parameters (intensity and frequency) we ensure that the regime is entered in which this first-order drift effect becomes crucial but higher relativistic effects are negligible.

In order to introduce this drift in the laser propagation direction and to illustrate the main features of a free electron in the laser field in general, it seems reasonable to discuss the electron dynamics of a classical free electron in the laser field prior to the treatment of the ionization process of atomic and molecular orbitals (see next section (2.2)).

The relativistic dynamics of a classical electron in the laser field is described by the Newton-Lorentz equation (in atomic units!):

$$\frac{d}{dt}\frac{\mathbf{v}(t)}{\sqrt{1-\left(\frac{\mathbf{v}(t)}{c}\right)^2}} = -\left(\mathbf{E}(\mathbf{r},t) + \frac{\mathbf{v}(t)}{c}\times\mathbf{B}(\mathbf{r},t)\right), \tag{2.1}$$

where $\mathbf{v}(t) = \frac{d}{dt}\mathbf{r} = \begin{pmatrix} \dot{x}(t) \\ \dot{y}(t) \\ \dot{z}(t) \end{pmatrix}$ is the velocity of the electron in dependence of the time t; Eq. (2.1) is valid in the lab system. The speed of light c takes a value of 137 a.u. Note that due to the choice of atomic units, the sign on the right-hand side in Eq. (2.1) reflects the electron charge. The entire term on the right-hand side of Eq. (2.1) represents the Lorentz force. The term $\mathbf{E}(\mathbf{r}, t)$ and $\mathbf{B}(\mathbf{r}, t)$ denotes the laser electric field or the laser magnetic field, respectively. Therefore, we have chosen linear polarization for the purpose of illustration:

$$\mathbf{E}(\mathbf{r}, t) = \mathbf{e_x} E_0 f(\eta) \sin \eta$$

and

$$\mathbf{B}(\mathbf{r}, t) = -\mathbf{e_z} E_0 f(\eta) \sin \eta$$

with $\eta = \omega(t - y/c)$. The term E_0 denotes the electric field amplitude of the laser field, ω its angular frequency. The phase of the laser field is represented by η. The propagation of the laser field takes place in the positive y-direction. The vectors $\mathbf{e}_x$ and $\mathbf{e}_z$ are unit vectors along the corresponding axis. An analytic treatment of the Newton-Lorentz equation (2.1) yields the following important facts [34]:

- The electron oscillates along the laser polarization direction with a quiver amplitude α:

  $$\alpha = \frac{E_0}{\omega^2}.$$

  In addition to this oscillation there is also a linear drift motion in this direction possible, depending on the initial conditions.

- The electron travels in the laser propagation direction a distance Δy per laser cycle:

  $$\Delta y = \frac{\pi}{2} \frac{E_0^2}{\omega^3 c}$$

As a result, the interaction of a classical electron with an intense linearly polarized laser field leads mainly to a two-dimensional motion consisting of oscillation and linear drift in the laser polarization direction and the drift in the laser propagation direction (if the trivial linear drift perpendicular to this plane due to the initial conditions is neglected). This two-dimensional motion results from the Lorentz force, as we show now. Neglecting the term $\left(\frac{v}{c}\right)^2$ in the square root of Eq. (2.1) yields:

$$\frac{d}{dt}\mathbf{v}(t) = -\left(\mathbf{E}(\mathbf{r}, t) + \frac{\mathbf{v}(t)}{c} \times \mathbf{B}(\mathbf{r}, t)\right). \tag{2.2}$$

Fig. (2.1) shows the numerical solution of this equation in the x-y–plane (the x-direction corresponds to the laser polarization direction and the y-direction to the laser propagation direction). The initial velocity in z-direction has been chosen as zero so that there is no trivial drift in this direction. In this figure ω =0.18 a.u. and E_0 =2 a.u.[1] Fig. (2.1)

[1]This corresponds to a laser intensity $I = 3.51 \cdot 10^{16} \frac{\mathrm{W}}{\mathrm{cm}^2} \cdot \left(E_0[\text{a.u.}]\right)^2 = 1.4 \cdot 10^{17} \frac{\mathrm{W}}{\mathrm{cm}^2}$.

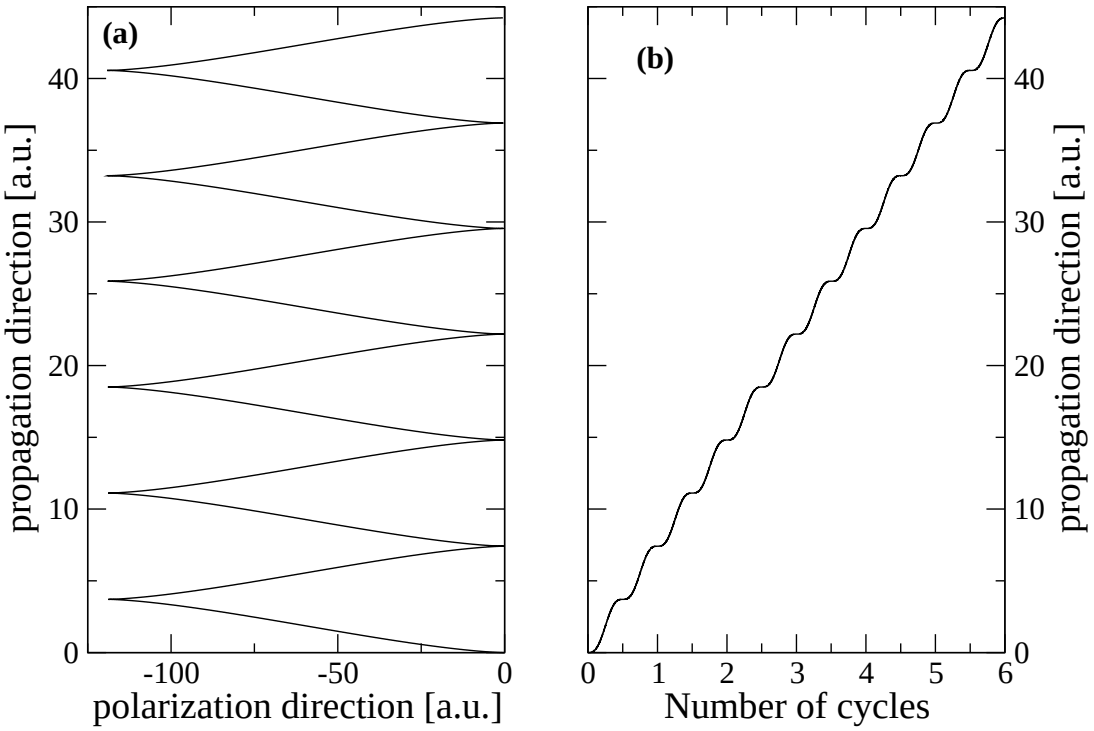

Figure 2.1: (a): Typical zig-zag motion of a classical electron subject to a cosine laser field. The electron has been initially at rest. The drift in the laser propagation direction which is induced by the magnetic component of the laser field becomes more important for stronger fields. If a sine laser field had been applied instead of a cosine one there would have been in addition to the oscillation in the laser polarization direction a linear drift motion in this direction. (b): Motion in the laser propagation direction versus the number of laser cycles. This part of the figure belongs to part (a). The points where the slope of the curve vanishes correspond to the turning points in (a). At these points the electron velocity is zero resulting in a vanishing drift in the propagation direction at these times according to the Lorentz force.

demonstrates also the occurrence of the oscillation in the laser polarization direction and the drift in the laser propagation direction owing to the magnetic component of the Lorentz force. (A numerical integration of the full relativistic equation (2.1) yields the same result in this parameter regime of Fig. (2.1)).

The drift in the laser propagation direction which is also present for ejected wave packets after laser-induced ionization of atoms or molecules plays an important role in this thesis [35]. The displacement of wave packets in the laser propagation direction has a direct impact on the recollision of wave packets with the mother ion and with this on high-order harmonic generation.

Neglecting the magnetic component of the Lorentz force in Eq. (2.2) leads merely to an oscillation in the laser polarization direction, plus a linear drift in this direction, depending on the initial conditions. This approximation can only be performed in a regime of laser

parameters in which the terms of the order of $\mathbf{v}/c$ are negligible.

In the simulations presented in this thesis, the magnetic component of the Lorentz force is nevertheless neglected in order to compare with a calculation for which this approximation has not been performed. This helps to assess the influence of the electron drift in the laser propagation direction on the results, e.g., on high harmonic spectra.

Concluding this section, we briefly explain how in a quantum-mechanical calculation, which consists of the solution of the corresponding time-dependent Schrödinger equation, the drift in the laser propagation direction can be neglected. This is a rather technical issue. Instead of neglecting the term $\mathbf{v}/c$ in Eq. (2.2), one obtains the same result by neglecting the laser magnetic field $\mathbf{B}(\mathbf{r},t)$. In the quantum-mechanical treatment the latter strategy is pursued, i.e., one applies the so-called **dipole approximation** for the laser field. The Hamiltonian which belongs to Eq. (2.2) possesses the following form:

$$H = \frac{1}{2}\left(\mathbf{p} + \frac{1}{c}\mathbf{A}(\mathbf{r},t)\right)^2, \tag{2.3}$$

where $\mathbf{p}$ is the canonical momentum and $\mathbf{A}(\mathbf{r},t)$ the vector potential from which the laser electric and magnetic field can be inferred, respectively.

The dipole approximation consists in the neglect of the spatial dependence of the vector potential, i.e., $\mathbf{A}(\mathbf{r},t) \approx \mathbf{A}(\mathbf{0},t) = \mathbf{A}(t)$. Thus, due to $\mathbf{B} = \nabla \times \mathbf{A}$, the laser magnetic field is neglected. (One should keep in mind that the dipole approximation for the laser field is only justified if the electron velocity is negligible to the speed of light corresponding to the neglect of $\mathbf{v}/c$ in Eq. (2.2). As a preparation of the following section, two customary gauges in the case of the dipole approximation are presented. In dipole approximation, the Hamiltonian (2.3) reads in velocity gauge:

$$H = \frac{1}{2}\mathbf{p}^2 + \frac{1}{c}\mathbf{A}(t)\cdot\mathbf{p} + \frac{1}{2c^2}\mathbf{A}^2(t). \tag{2.4}$$

Applying a gauge transformation[2] to the electro-magnetic potentials $\mathbf{A}(\mathbf{r},t)$ and $\phi(\mathbf{r},t)$ ($\phi \equiv 0$ in Eq. (2.4)) and to the wave function $|\psi(t)\rangle$ of the electron yields:

$$H = \frac{1}{2}\mathbf{p}^2 + \mathbf{E}(t)\cdot\mathbf{r}. \tag{2.5}$$

This is the Hamiltonian in length gauge. The gauge function $\chi(\mathbf{r},t)$ is $-\mathbf{A}(t)\cdot\mathbf{r}$.

[2]This transformation to the new quantities $\mathbf{A}'$, ϕ' and $|\psi'(t)\rangle$ is performed via:

$$\mathbf{A}' = \mathbf{A} + \nabla\chi(\mathbf{r},t), \quad \phi' = \phi - \frac{1}{c}\frac{\partial\chi}{\partial t}(\mathbf{r},t), \quad |\psi'(t)\rangle = e^{i\frac{1}{c}\chi(\mathbf{r},t)}|\psi(t)\rangle.$$

2.2 The ionization process

After having discussed the dynamics of a free classical electron in a laser field, the attention is directed to the ionization process which an atom or a molecule undergoes when it is subject to a strong laser pulse. Depending on the frequency and the intensity of the applied laser pulse, one distinguishes three different types of ionization processes: Multiphoton ionization, tunnelling ionization and over-the-barrier ionization (OTBI).

In the multiphoton regime, the ionization is characterized by the absorption of certain multiples of laser photons to create a continuum wave packet. As for the pathway of the initial bound electron to escape the atomic potential, intermediate bound states may be occupied prior to final ionization (see Fig. 2.2)(a). Thus, resonances among different bound states may play an important role in this regime. Furthermore, it is typical of the multiphoton regime that the center-of-mass trajectory of the entire wave function is found adjacent to the nucleus during the interaction with the laser pulse; the center-of-mass trajectory does not resemble the trajectory of a free classical electron in the laser field as this is often the case in the two other regimes. A further characteristics of the multiphoton regime is that the ionization rate of an n-photon absorption process is proportional to I^n, where I denotes the intensity of the applied laser field. It is also possible that an atom/molecule can absorb more laser photons than actually needed for escaping the core potential. In this case, the energy which is not required for the escape is transformed into kinetic energy of the continuum electrons formed. This process is called above-threshold ionization (ATI). In ATI-spectra, the kinetic energy of the various photo-electrons emitted during the ionization process are shown.
Increasing the laser intensity leads to the regime of tunnel ionization. In this regime, the following intuitive picture illustrated in Fig. 2.2(b) holds: In length gauge (see Eq. (2.5)), the electron senses the effective potential $V_{\text{eff}}(x,t) = V(x) + E(t) \cdot x$ (for simplicity, a 1d model corresponding to Fig. 2.2 is chosen) which is the sum of the original undisturbed core potential $V(x)$ and the time-dependent potential $E(t) \cdot x$ describing the interaction of the laser electric field $E(t)$ with the electron. The latter term tilts the original potential barrier $V(x)$ which the bound electron senses. As a result, the electron sees a tilted potential barrier through which it can tunnel into the continuum. This is shown in Fig. 2.2(b). This figure represents a snapshot of the effective potential $V_{\text{eff}}(x,t)$. It shows the situation in which the laser electric field possesses a notable value in order to be able to suppress the core potential $V(x)$. The situation which is shown in Fig. 2.2(b) and which illustrates a tunnelling event occurs for different times during the interaction with the laser field. In other words, there is continuous tunnelling through the current potential barrier, giving rise to the "birth" of continuum wave packets. The population of these continuum wave packets is ruled by the width and the height of the potential barrier through which the electron wave packet tunnels. The fact that there are continuum electron wave packets at different times during the ionization process leads to important ramifications for the recollision process that the tunnelled wave packet may undergo. After ejection, the tunnelled wave packets follow different trajectories in the laser field. They may be viewed as free particles in the laser field. Thus, the time of "birth" of a continuum wave packet determines which trajectory is followed. This is explained in

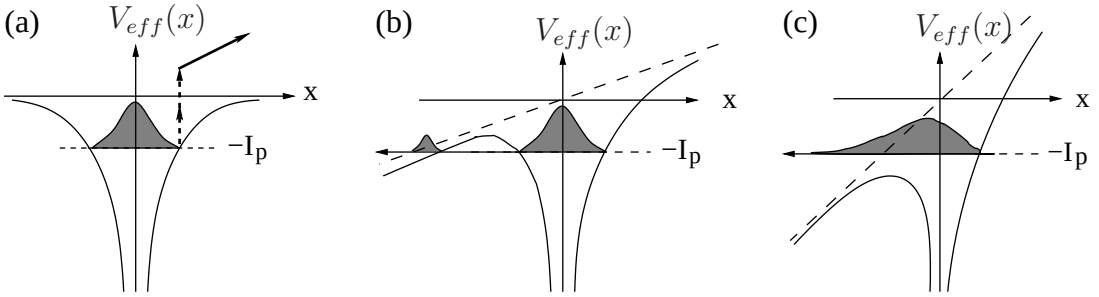

Figure 2.2: Schematic diagram of three different types of ionization mechanisms. Shown is the snapshot of the effective potential $V_{eff}(x)$:
(a): Multiphoton ionization occurs by means of the absorption of laser photons via the occupation of intermediate states.
(b): Tunneling regime: For a stronger laser field the laser electric field tilts the core potential forming a potential barrier through which the electro can tunnel into the continuum.
(c): Over-the-barrier regime: For even higher intensity the barrier of the effective potential is suppressed beneath the eigenenergy of the bound state. Thus, the major part of the population is transferred into the continuum instantaneously as soon as this situation is given.

detail in the section (2.3.2). In order to have a criterion at hand which helps to decide whether the electron dynamics takes place in the multiphoton regime or in the tunnelling regime, the so-called Keldysh parameter γ is useful:

$$\gamma = \sqrt{\frac{I_p}{2U_p}},$$

where I_p is the ionization potential and U_p denotes the ponderomotive energy. The ponderomotive energy corresponds to the average kinetic energy of a free, non-relativistic electron in the laser field. It can be expressed by means of the angular frequency ω and the electric field amplitude E_0 of the laser field as:

$$U_p = \frac{1}{4}\left(\frac{E_0}{\omega}\right)^2.$$

If $\gamma > 1$, the ionization takes place in the multiphoton regime, and if $\gamma < 1$, the tunnelling regime is reached.
The ionization rate in the tunnelling regime is dominated by the expression $\exp\left(-\frac{\text{const}}{E}\right)$, where E is the electric field amplitude of the laser field. The exact expression for the often used ADK-ionization rate is given in [36]. The idea to deduce this expression is to consider the laser electric field as quasi-static over a fraction of an optical cycle.
If the laser intensity increases further the laser electric field tilts the potential barrier in a manner that this potential barrier is pressed beneath the binding energy. This is illustrated in Fig. 2.2(c). The corresponding ionization process is called *over-the-barrier ionization* (OTBI). As a result of this barrier suppression, most of the population is found in the continuum, since no tunnelling is required anymore in order to escape the

core potential. If this over-the-barrier situation as depicted in Fig. 2.2(c) occurs early in the first laser cycle of the pulse, no wave packets with "birth"-times after this over-the-barrier ionization event are ejected. This means that not all trajectories which could be realized in the tunnelling regime are followed. This again has a significant impact on the recollision process and with this on high-order harmonic generation.

2.3 The recollision process and high-order harmonic generation (HHG)

When an atom or molecule is ionized by an intense laser pulse an ejected electron wave packet travels in a quasi-free manner in the laser field. As the laser field changes its sign the electron wave packet is accelerated back towards the parent ion. At the recollision of the returning electron with the core several phenomena might occur, which give rise to prominent effects in the field of laser-atom and laser-molecule interactions, respectively. One possibility which becomes important for multi-electron systems is that the recolliding electron interacts with a bound electron and, as a result of this recollision, transfers it into the continuum. This process is known as nonsequential double ionization.
Another process which also shows up in one-electron systems and which might occur upon recollision consists in the possibility that the returning electron is elastically scattered from the nucleus (nuclei). Thereby, the kinetic energy of the photoelectrons may be increased by means of the laser-assisted recollision. This effect is called high-order above threshold ionization (ATI). The alternative process for the elastic re-scattering is the generation of high-order harmonic radiation as a result of the recombination of the recollding electron wave packet into the initial state at the position of the nucleus (nuclei). Since high-order harmonic generation (HHG) is in the focus of this thesis some aspects of it are elucidated in detail in the following sections of this chapter.

2.3.1 Basic properties of HHG-spectra

During the recollision-recombination process for HHG electron wave packets are accelerated at the position of the nucleus (nuclei). As it is already known from classical electro-dynamics, moving charged particles give rise to electro-magnetic radiation [37]. The corresponding quantum-mechanical description is non-trivial. It is elaborated in [38]. The coherent part of the radiation which is emitted during the recollision process is given by the dipole acceleration $\mathbf{a}(t)$. For not too high electron velocities in comparison with the speed of light the emitted electric field is proportional to $\mathbf{a}(t)$ (see section (3.3)).

The dipole acceleration $\mathbf{a}(t)$ is calculated via Ehrenfest's theorem as a time-dependent expectation value:

$$\mathbf{a}(t) = \langle \psi(t) | \nabla V + \mathbf{E}(t) | \psi(t) \rangle \,, \tag{2.6}$$

where $|\psi(t)\rangle$ denotes the electronic wave function, V the core potential and $\mathbf{E}(t)$ the laser electric field.

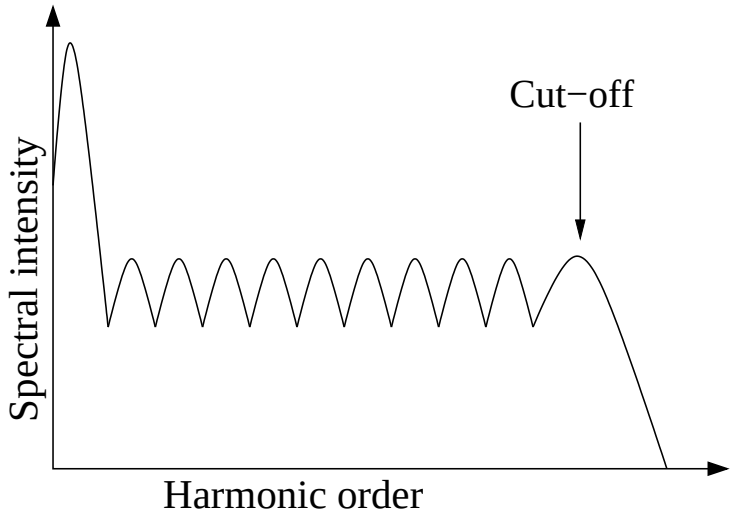

Figure 2.3: Schematic diagram of a typical harmonic spectrum.

The harmonic spectrum is obtained by means of Fourier transformation of the dipole acceleration:

$$\begin{aligned} S_{\hat{\mathbf{e}}}(\omega) &\sim |\hat{\mathbf{e}} \cdot \mathbf{a}(\omega)|^2 \\ &= \left| \int \langle \psi(t) | \hat{\mathbf{e}} \cdot [\nabla V + \mathbf{E}(t)] | \psi(t) \rangle e^{i\omega t} dt \right|^2 \end{aligned} \tag{2.7}$$

This is the spectrum of harmonic radiation polarized along the direction of the unit vector $\hat{\mathbf{e}}$. In this thesis $\hat{\mathbf{e}}$ is taken along the laser polarization direction and the laser propagation direction, respectively [3].

In the following we briefly discuss the basic properties of harmonic spectra which calculated and experimental spectra have in common. Fig. (2.3) illustrates a typical spectrum [4]. The spectral intensity peaks at the first harmonic order (the harmonic order is defined as the frequency of radiation divided by the laser frequency) and then considerably drops off until a plateau is reached in which the harmonic intensity remains constant over a wide range of harmonic orders. The plateau breaks off at a certain cut-off harmonic order.

[3] Although a full quantum-mechanical treatment reveals that calculating the harmonic spectrum emitted by a *single* atom/molecule from the dipole expectation value is actually incorrect, it is nevertheless reasonable when a comparison of the calculated spectra with those obtained in an experiment with dilute gases is intended For a large sample of atoms/molecules the resulting dipole acceleration is given to a good approximation by the number of atoms/molecules in the sample times the dipole expectation value of a *single* atom/molecule [38]

[4] Of course, in the case of experimental harmonic spectra effects which arise from the superposition of radiation emitted from each single atom/molecule in the sample may emerge in addition to the characteristics discussed here. It is vital for the experimental detection of the radiation that the emitted radiation from each atom/molecule is constructively superposed (phase-matching) so that the signal of the entire sample becomes sufficiently large. For this reason, the detection of the harmonic signal in a gas target is required in the laser propagation direction [39].

The harmonic peaks are only found at integer multiples of the laser frequency. This is not a quantum effect but the result of periodic harmonic emission over many laser cycles. There are selection rules which determine the harmonic order emitted. For these rules the symmetry of the combined system target plus laser field plays an essential role [40]. For example, for a spherical symmetric system as an atomic ground state subject to a linearly polarized laser pulse of long duration the generation of even harmonics polarized along the laser polarization is suppressed.

In general (regardless the fact that there are exceptions under special conditions), the cut-off frequency is given by:

$$\omega_{max} = I_P + 3.17\, U_P \ , \tag{2.8}$$

where I_P denotes the ionization potential and U_P the ponderomotive energy of the laser field. This formula can be explained with the help of the recollision model of high-order harmonic generation. This model consists of three steps. In the first one, electron wave packets tunnel into the continuum due to the interaction of an atomic or molecular orbital with an intense laser field. To be precise, *different* wave packets tunnel out at *different* times. Calling the formation of a tunnelled continuum wave packet dramatically a "birth" of an electron (wave packet), these different times of birth give rise to different trajectories of these wave packets in the laser field, because in the second step the freed electron wave packets move in a quasi-free manner in the laser field. However, the time of birth of a wave packet is decisive for the actual trajectory the wave packet follows during this quasi-free motion. In the third final step, a wave packet which re-collides with the population of the initial state at the position of the nucleus (nuclei) recombines into this initial state under harmonic emission. Which harmonics are emitted depends on the kinetic energy that the re-colliding wave packet possesses at the recollision event. This kinetic energy again depends on the time of birth. The maximum kinetic energy is given by $3.17\, U_p$. To be precise, this is the maximum kinetic energy of the wave packets which *re-collides* at all; there are also wave packets that never revisit the mother ion. It is again the time of birth which decides whether or not a recollision takes place. These facts are illustrated by the semi-classical model of HHG depicted in the following section.

The recombination of the re-colliding continuum wave packet into the initial state is incorporated in the dipole acceleration (2.6). Assuming that the wave function $|\psi(t)\rangle$ at the time of recollision t can be described as a superposition of the initial state $|\psi_{\text{init}}(t)\rangle = \alpha(t)|\psi_{\text{init}}\rangle$ and the re-colliding continuum wave packet

$$|\psi(t)\rangle = \alpha(t)|\psi_{\text{init}}\rangle + \beta(t)|\psi_c\rangle, \tag{2.9}$$

where the coefficients $\alpha(t)$ and $\beta(t)$ determine the occupation of these states, the decisive matrix element for the emission of the plateau harmonics is given by:

$$\alpha^*(t)\beta(t)\langle\psi_{\text{init}}|\nabla V|\psi_c\rangle. \tag{2.10}$$

This expression which is also incorporated in the expectation value of the dipole acceleration describes the transition from continuum states which form the continuum wave

packet to the initial state at the position of the nucleus (nuclei). This matrix element clearly shows that at the recollision event the overlap of the re-colliding wave packet with the initial wave function is vital for the strength of the harmonic signal. Furthermore, this overlap must be given at the vicinity of the nucleus (nuclei). This is the only position where the force ∇V renders a substantial contribution. The term in (2.6) containing the laser field contributes only to the low harmonic orders in the vicinity of the first harmonic order (= laser frequency). The overlap of the re-colliding wave packet and the initial state and with this the harmonic signal is reduced if the re-colliding wave packet spreads considerably during the quasi-free motion in the laser field. Wave packets with a larger travel time (= time between recollision and birth) undergo a larger spreading. The travel time depends on the time of birth.

Another impediment for HHG represents, in general, the electron drift induced by the laser magnetic field (see section 2.1). This drift leads to a displacement of the re-colliding wave packets in the laser propagation direction, which reduces the overlap and with this harmonic emission. It is shown in the context of this thesis for the first time that in contrast to this, the magnetic-field drift may also enhance the overlap and harmonic emission if antisymmetric initial states are applied (see chapter (5)).

The occurrence of the coefficient $\alpha^*(t)$ in (2.10) indicates that the initial state has to be occupied at the recollision event. Thus, if the intensity of the applied laser pulse is too high, the initial state may be depleted prior to the recollision event of certain harmonics. As a result, these harmonics cannot be emitted. A too rapid depletion of the initial state leads to the fact that there is no formation of a tunnelled wave packet after depletion. This may result in the circumstance that there are no wave packets ejected which contribute to the cut-off harmonics. The features of the trajectories of the ejected wave packets are discussed within the semi-classical model of HHG in the following section.

2.3.2 The semi-classical three-step model or Corkum model

As mentioned in the previous section, the time when an electron wave packet is ejected during the ionization process is crucial for the kinetic energy at the recollision-recombination event. Thus, this time of birth determines the harmonic order of the radiation emitted.

The reason for this fact is that, depending on the time of birth, the electron wave packets follow different specific trajectories after ionization during the quasi-free motion in the laser field. Thereby, the electron wave packets may gain different kinetic energies through the interaction with the laser field. This mechanism can be described within a simple semi-classical model which was first proposed by Corkum [24]. In this model, one assumes that an electron wave packet is ejected via laser-induced ionization at the time of birth t_0. After ionization, the electron wave packet is considered as a classical particle for which the classical equation of motion for the quasi-free motion in the laser field is solved. The classical electron is assumed to start at the origin (i.e. at the position of the nucleus) with zero initial velocity. These initial conditions yield a specific trajectory. This classical

trajectory is believed to describe the essential behavior of the quasi-free electron wave packet in the laser field. This procedure is justified by the assumption that after ionization the electron motion is dominated by the influence of the strong laser field and that the impact of the core potential becomes negligible for larger distances away from the core. This assumption represents the content of the so-called *strong-field approximation* (SFA), which has turned out to be a reliable approximation for the description of strong-field processes like high-order harmonic generation and high-order ATI [41]. Of course, the classical trajectories do not describe the spreading of the re-colliding wave packet which reduces the harmonic signal, but it both accounts for the existence of the 3.17-cut-off rule (2.8) and provides a simple picture of high-order harmonic generation which can be re-discovered in a full quantum-mechanical approach [42]. The actual recombination process which is clearly a quantum effect (see matrix element (2.6)) is treated in the semi-classical model in the way that the kinetic energy $E_{\mathrm{kin}}(t_1)$ at the time of recollision t_1 is calculated and the emission of a harmonic photon with frequency $I_p + E_{\mathrm{kin}}(t_1)$ is assumed, where I_p denotes the ionization potential of the atomic/molecular species considered. As a consequence, from a methodical point of view, the semi-classical model consists essentially of the computation of classical trajectories. This is exemplified in the following for a sinusoidal laser field of linear polarization which interacts with a classical electron. The essential physics thus occurs in the laser polarization direction, within the dipole approximation for the laser field. The corresponding Newtonian equation of motion reads:

$$\ddot{x}(t) = -E_0 \sin(\omega t), \tag{2.11}$$

where $x(t)$ describes the position of the electron in laser polarization direction in dependence of the time t. The laser parameters E_0 and ω denote the laser electric peak amplitude and the laser angular frequency, respectively. The initial conditions at the time of birth t_0 are:

$$\begin{aligned} x(t_0) &= 0, \\ \dot{x}(t_0) &= 0. \end{aligned}$$

The resulting solution of (2.11) is given by:

$$x(t) = \frac{E_0}{\omega^2}[\sin(\omega t) - \sin(\omega t_0) - \omega(t - t_0)\cos(\omega t_0)]. \tag{2.12}$$

One recognizes that there is, owing to the initial conditions, a linear drift motion in addition to the oscillation.

The recollision time t_1 is calculated by imposing $x(t_1) = 0$. Only the first recollision is taken into consideration, for in the quantum case the spreading of the wave packet re-colliding for the second time would be larger than it was at the first recollision, which justifies the expectation that a second recollision would only give a negligible contribution to HHG. Of course, the condition $x(t_1) = 0$ cannot be fulfilled for each t_0. This means that there are trajectories which never return to the core. Only the trajectories which return to the core are of interest for HHG. The recollision time t_1 is a function of the time of birth t_0, i.e., $t_1 = t_1(t_0)$ and, as a result, the kinetic energy at the recollision event is

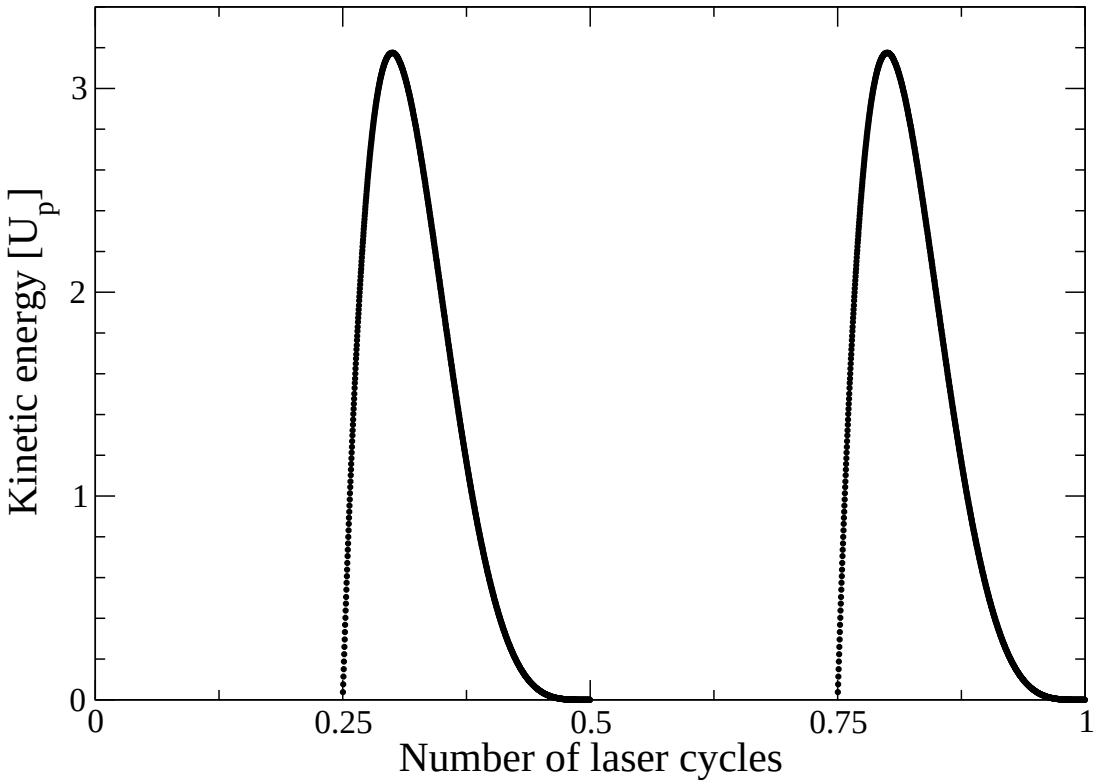

Figure 2.4: Kinetic energy in units of the ponderomotive potential U_p of recolliding electrons versus the time of birth t_0. To obtain this figure the trajectory (2.12) has been solved for zeros for various t_0 and the kinetic energy at the time of recollision has been evaluated. Note that only trajectories which exhibit recollisions have been taken into account. The maximum kinetic energy for recolliding electrons is 3.17 U_p. For this figure the parameters E_0=2 a.u. and ω= 0.18 a.u. have been employed.

a function of t_0, i.e., $E_{\mathrm{kin}} = E_{\mathrm{kin}}\big(t_1(t_0)\big)$ as well. Solving Eq. (2.12) numerically for zeros for various t_0 shows that the maximum kinetic energy is given by 3.17 U_p, which confirms the cut-off rule (2.8), see also Fig. (2.4). This is a general result. It is valid for the more general laser field given by $E_0 \sin(\omega t + \phi_0)$ with arbitrary ϕ_0.

In conclusion, we point out that an atom/molecule which is subjected to a laser field that leads to a depletion of the initial state before the trajectory yielding the 3.17 U_p is started does not obey the common 3.17-rule (2.8).

2.3.3 Quantum-mechanical description of HHG

In this section, a full quantum-mechanical approach based on the SFA, which can be viewed as the quantum-mechanical counterpart of the semi-classical three-step model discussed in the previous section, is briefly delineated [42]. In the context of HHG, this analytical method represents an alternative to the direct numerical integration of the time-dependent Schrödinger equation, which is used in this thesis and which is therefore

discussed in detail in chapter (3).

This theory is outlined for the case of an atom in its ground state $|0\rangle$, which is subject to an intense laser field. This illustration leans on [42]. There are extensions of this theory to the treatment of molecules in laser fields within the Born-Oppenheimer approximation [43]. The following criteria have to be met by choice of the laser parameters and the atomic species:

(a) During the evolution of the system the occupation of bound states different from the initial state can be neglected.

(b) The depletion of the initial state is negligible.

(c) The electron remains unaffected by the core potential in the continuum (SFA).

This approach (extended to the molecular version) cannot be followed in the framework of this thesis, since the first two conditions (a), (b) are not always fulfilled as the results of the direct numerical solution of the time-dependent Schrödinger equation shows (see chapter (5)). Given the above conditions (a)-(c), the solution of the time-dependent Schrödinger equation $|\psi(t)\rangle$ can be expressed by the following ansatz:

$$|\psi(t)\rangle = e^{iI_p t}\left(|0\rangle + \int d^3\mathbf{v}\; b(\mathbf{v},t)|\mathbf{v}\rangle\right), \tag{2.13}$$

where I_p denotes the ionization potential. The expression $b(\mathbf{v},t)$ represents the amplitude of the corresponding continuum state $|\mathbf{v}\rangle$. The ansatz (2.13) is inserted into the time-dependent Schrödinger equation, which leads to a differential equation for $b(\mathbf{v},t)$. This differential equation can be solved exactly resulting in a closed expression for $b(\mathbf{v},t)$. Further, a closed expression for the time-dependent dipole moment can be inferred from this. The modulus square of the Fourier transform of the dipole moment gives the harmonic spectrum. In conclusion, we would like to mention an advantage of this Lewenstein approach over the direct numerical integration of the time-dependent Schrödinger equation: This approach takes the full dimensionality of the system into account, i.e., one does not have to restrict oneself to two dimensions or one dimension as it is often the case for the direct numerical integration. Furthermore, the Lewenstein model has the potential to be extended to more complex systems like molecules for which a numerical integration is not feasible. In addition, non-dipole terms which arise from the spatial dependence of the vector potential (i.e., the laser magnetic field is taken into account) have been included in the Lewenstein formalism [44].

2.3.4 High-harmonic generation in molecules

Harmonic spectra of atoms and molecules have in principle the same characteristics in common. However, in the case of molecules, the additional degrees of freedom like the presence and the motion of several nuclei and the anisotropy of molecular orbitals are reflected in the harmonic spectra of molecules. In this section we would like to point

out the most important facts about the additional two-center interference structures in harmonic spectra of diatomic molecules, because they are also discussed in the context of harmonic spectra of H_2^+ in chapter (5). The following presentation is based on [45].

In harmonic spectra of diatomic molecules, characteristic minima and maxima due to the presence of two nuclei can be found. The occurrence of these structures is attributed to the interference of the re-colliding electron wave packet with the initial molecular orbital at the positions of the two nuclei. The positions of the extrema in the spectrum depend both on the orientation of the molecule to the polarization direction of the applied laser field and on the separation of the nuclei; however, note that within this context the nuclei are assumed to be clamped at certain positions during the interaction with the laser pulse. One can infer simple formulas which predict the positions of the extrema in dependence on the nuclear separation R and the orientation angle θ between the molecular axis and the polarization direction of the laser pulse: The condition which holds for the interference minima is given by:

$$R\cos\theta = (2m+1)\lambda/2, \quad m = 0, 1, 2, \ldots \tag{2.14}$$

and for the maxima the condition

$$R\cos\theta = m\lambda, \quad m = 0, 1, 2, \ldots \tag{2.15}$$

has to be fulfilled. The de-Broglie wavelength of the re-colliding electron is denoted by λ. These conditions are valid for symmetric initial states, whereas the conditions have to be interchanged for antisymmetric initial states.

We remark that within this simple picture the positions of the extrema do only depend on the inter-nuclear separation and the orientation of the molecule. The deduction of these formulas precludes details of the ionization process, e.g. the shape of the tunnelled electron wave packet. This leads to the circumstance that the formulas above are completely independent of the laser intensity.

In the case that the molecular axis is perpendicular to the laser polarization direction ($\theta = 90°$), no two-center-interference structure occurs, since there is no phase difference between the re-colliding incident wave and the initial orbital sited at the two nuclei.

In conclusion, we would like to mention that the impact of the nuclear motion on the harmonic spectra has recently been investigated [43]. In particular, nuclear motion has been taken into account within an adapted Lewenstein model. The dissociation of the nuclei suggests an overall decrease in harmonic intensity. In the numerical approach of this thesis, which consists in the direct integration of the time-dependent Schrödinger equation in two dimensions, the nuclear motion is not taken into consideration, since the nuclear motion would require an extra dimension. This would result in unacceptable computational requirements if one was not willing to perform the dipole approximation. Moreover, the spatial dependence of the vector potential, if the dipole approximation was not carried out, would lead to complications with respect to the introduction of relative coordinates and center-of-mass coordinates, which would help to reduce the computational efforts.

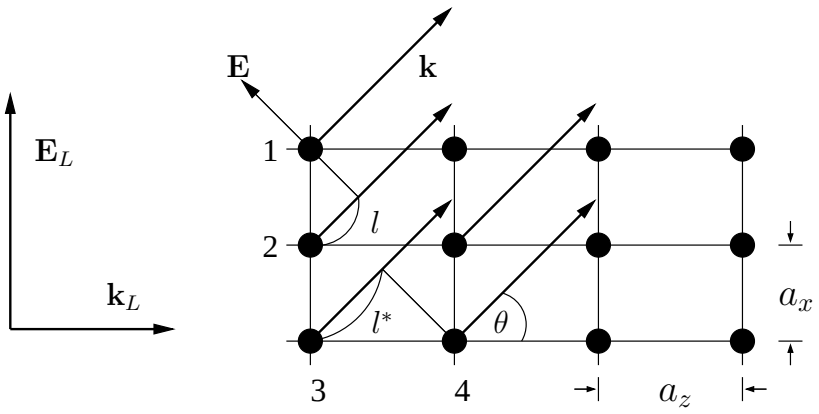

Figure 2.5: Phase-matching of HHG from a thin solid crystal layer. "Transverse" phase-matching between ions 1 and 2 and "longitudinal" phase-matching between ions 3 and 4 lead to the conditions (2.17) and (2.18), respectively.

2.3.5 High-harmonic generation from crystals

In this thesis, harmonic spectra of a single atom or molecule are computed. In terms of a realization of a HHG-experiment, however, a strong harmonic signal is desirable. This can be achieved by means of a gas target for which the harmonic radiation of the single species adds up coherently if the harmonic radiation is detected in the laser propagation direction [39]. However, if one focusses on the harmonic radiation which is polarized in the laser propagation direction, the detection in this direction is precluded, since the single-atom/molecule harmonic radiation of this polarization is not emitted in the laser propagation direction. The harmonic radiation polarized in the laser propagation direction is of interest in chapter (4).

Therefore, we briefly present another method to obtain a phase-matched harmonic signal which allows for a detection direction different from the propagation direction. This method is based on the usage of crystals. We follow the representation given in [46], only depicting the essential idea.

The system of interest is a thin solid crystal layer subject to a strong laser beam. The dimensions of the layer are to be substantially smaller than the radius of the laser beam. In order to achieve constructive interference of the harmonic waves of all ions, conditions similar to the Bragg condition in solid state physics have to be imposed. The difference to the Bragg condition is that the harmonic waves are generated within the crystal via the mechanism for the harmonic radiation of a single atom/molecule. For harmonic radiation from two ions in the crystal with displacement vector $\boldsymbol{\ell}$, the following condition ensuring constructive interference of the emitted harmonic waves must hold:

$$|\omega t - \mathbf{k} \cdot \boldsymbol{\ell}| = 2\pi s, \quad s = 1, 2, \ldots, \tag{2.16}$$

where ω and $\mathbf{k}$ are the frequency and the wave-vector of the harmonic radiation, respectively, with $k = |\mathbf{k}| = n\omega/c$, n being the refraction index of the harmonic radiation, and

$t = \mathbf{k}_L \cdot \boldsymbol{\ell}/\omega_L$ is the time the laser pulse takes to propagate the distance $\ell = |\boldsymbol{\ell}|$ between the ions, where $\mathbf{k}_L$ denotes the laser wave-vector and ω_L the laser frequency. Fig.(2.5) illustrates the situation for a periodic crystal structure subject to the laser field $\mathbf{E}_L$ which is polarized in x-direction and which propagates in z-direction. The terms a_x and a_z denote the lattice period in the corresponding directions, θ is the angle between the propagation direction of the laser pulse and the harmonic wave-vector $\mathbf{k}$. Phase-matching between ions 1 and 2 requires according to Eq. (2.16): $\omega t - k\ell = 2\pi s_1$ with $t_1 = 0$, $\ell = a_x \sin\theta$ and integer s_1. This results in the condition:

$$k a_x \sin\theta = 2\pi s_1. \tag{2.17}$$

Phase-matching between ions 3 and 4 imposes: $\omega t - k\ell^*$ with $\ell^* = a_z \cos\theta$, time delay $t = a_z n_L/c$ and integer s_2. This leads to the condition:

$$a_z \omega (n_L - n\cos\theta)/c = 2\pi s_2. \tag{2.18}$$

We refer to these conditions in chapter (4).

Chapter 3

Model system and numerical approach

3.1 Theoretical model of the laser-atom/molecule interaction

The electron dynamics after laser-induced ionization of atomic and molecular systems and with this high-order harmonic generation are in the focus of this thesis. In particular, we study these processes for one-electron systems of hydrogen-like ions and H_2^+. Since the quantum nature of these systems exposed to a linearly polarized short and strong laser pulse plays an important role for these processes a quantum-mechanical treatment is required. We focus on a regime of laser intensities and atomic/molecular systems with moderate binding energies for which the Schrödinger equation renders an adequate description. However, the choice of the laser parameters employed requires to take the laser magnetic field into account. Spin effects and higher-order relativistic effects are negligible in the regime of interest in this thesis. This implies that the solution of the Dirac equation [28] or the Schrödinger equation taking higher relativistic orders via a Foldy-Wouthuysen expansion of the Hamiltonian into account is not necessary [29]. As we have already shown for a classical electron in a laser field in section (2.1), the laser magnetic field gives rise to a drift motion of the electron in the laser propagation direction. Taking the laser magnetic field into consideration also for a quantum-mechanical description means that there is a drift of the electron wave packets in the laser propagation direction.

Our approach, which is discussed in this section, describes the quantum dynamics of a one-electron system subject to a strong laser pulse by means of the time-dependent Schrödinger equation within a two-dimensional model system. Hereby, we restrict ourselves to the plane spanned by the laser polarization direction and the laser propagation direction. The crucial physics occurs in this plane since the electron dynamics is mainly characterized by the laser electric field in the laser polarization direction and the drift in the laser propagation direction induced by the laser magnetic field. The reduction of

the model system to two dimensions has become an established method in the field of laser-matter interactions [11, 29]. This reduction to two dimensions permits a numerical treatment on a grid. For the parameter regime under consideration in this thesis a three-dimensional grid calculation would be too time-consuming and one would face a serious problem with the use of computer memory. Hence, it is reasonable to restrict oneself to the two crucial dimensions in order to perform the simulation under acceptable conditions[1].

Evidently, wave packet spreading in the direction perpendicular to the plane spanned by the laser polarization direction and the laser propagation direction is not described by our model. But this wave packet spreading leads merely to a less efficient recollision dynamics and with this to an overall decrease in the harmonic signal. The effects discussed in this thesis (see chapter (4) and (5)) are in principle not affected by this circumstance. A further consequence of this 2D description is the fact that it is more appropriate to model the interaction of the electron with the nucleus (nuclei) with the help of a soft-core potential instead of a Coulomb potential. The numerical solution of the time-dependent Schrödinger for this 2D system is depicted in section (3.2) and section (3.4) is dedicated to computation of the corresponding eigenfunctions.

The Schrödinger equation for the wave function $\Psi(\mathbf{r}, t)$ of the electron under the influence of both a potential of an ionic core (two protons for H_2^+) and an electro-magnetic field reads:

$$i\frac{\partial}{\partial t}\Psi(\mathbf{r}, t) = H\Psi(\mathbf{r}, t) \tag{3.1}$$

The Hamilton operator is given by:

$$H = \frac{1}{2}(\mathbf{p} + \frac{1}{c}\mathbf{A}(\mathbf{r}, t))^2 - \Phi(\mathbf{r}, t) + V_{ion}(\mathbf{r}) \tag{3.2}$$

Here c denotes the speed of light which is in atomic units 137 a.u. The position of the electron is described by $\mathbf{r} = (x, y)$ in a coordinate-system whose origin is at rest. In the case of an atomic ion this origin is identical with the nucleus while for H_2^+ this origin is centered in the middle of an inter-nuclear line connecting the two nuclei. Due to the large mass of the nucleus (nuclei) its slow motion is neglected in comparison with the fast electron motion. The laser field is included into the Hamiltonian via the electro-magnetic potential $\mathbf{A}$. Owing to the high intensity of the applied laser fields there is a high photon density which permits to treat the electro-magnetic field classically [47]. From the vector potential $\mathbf{A}$ the real fields can be inferred by:

$$\mathbf{E}(\mathbf{r}, t) = -\frac{1}{c}\frac{\partial \mathbf{A}(\mathbf{r}, t)}{\partial t} \tag{3.3}$$

and

$$\mathbf{B}(\mathbf{r}, t) = \nabla \times \mathbf{A}(\mathbf{r}, t)\,, \tag{3.4}$$

[1] Very recently, the possibility to solve the time-dependent Schrödinger equation in three dimensions taking the laser magnetic field into account has been pointed out. This approach is based on the expansion of the solution into a specific set of basis functions [25].

where $\mathbf{E}(\mathbf{r},t)$ is the electric field and $\mathbf{B}(\mathbf{r},t)$ is the magnetic one. Working the Hamiltonian (3.2) out and applying Coulomb gauge the Hamiltonian has the following form:

$$H = \frac{1}{2}\mathbf{p}^2 + \frac{1}{c}\mathbf{A}(\mathbf{r},t) \bullet \mathbf{p} + \frac{1}{2c^2}\mathbf{A}^2(\mathbf{r},t) - \Phi(\mathbf{r},t) + V_{ion}(\mathbf{r}) \tag{3.5}$$

3.1.1 The laser pulse

In the following, the laser pulse applied in the simulations of this thesis (see chapter (4) and (5)) is presented. This laser pulse is linearly polarized in the x-direction and propagates in the positive y-direction. In the latter direction the laser pulse is spatially and temporally confined. The pulse possesses a trapezoidal shape. This means that the amplitude of both the laser electric field and magnetic field increases linearly with the phase $\eta = \omega(t - y/c)$ over a few laser cycles. After this turn-on phase the amplitude of the laser field remains constant over a few laser cycles prior to a final linear decrease of the pulse to zero over a few laser cycles. Thus, the laser electric field owns the following form:

$$\mathbf{E}(\mathbf{r},t) = \mathbf{e_x} E_0 f(\eta) \sin\eta \tag{3.6}$$

and the laser magnetic field looks like:

$$\mathbf{B}(\mathbf{r},t) = -\mathbf{e_z} E_0 f(\eta) \sin\eta \tag{3.7}$$

The vectors $\mathbf{e_x}$ and $\mathbf{e_z}$ are unity vectors in the x-direction and the z-direction, respectively. Note that the laser magnetic field points out the x-y-plane. The electric peak amplitude is denoted by E_0. The term $f(\eta)$ characterizes the trapezoidal pulse shape:

$$f(\eta) = \begin{cases} 0 & : \quad \eta < 0 \\ \frac{\eta}{2\pi N_{on}} & : \quad 0 \leq \eta \leq 2\pi N_{on} \\ 1 & : \quad 2\pi N_{on} < \eta \leq 2\pi(N_{DUR} - N_{off}) \\ \frac{2\pi N_{DUR} - \eta}{2\pi N_{off}} & : \quad 2\pi(N_{DUR} - N_{off}) < \eta \leq 2\pi N_{DUR} \end{cases}$$

Here, N_{on} and N_{off} denote the number of laser cycles assigned to the turn-on phase and the turn-off phase of the laser pulse, respectively. The whole duration of the laser pulse is given by N_{DUR}. In order to obtain the fields (3.6) and (3.7) the vector potential $\mathbf{A}(\mathbf{r},t)$ fulfilling the Coulomb gauge is constructed as follows:

$$\mathbf{A}(\mathbf{r},t) = \mathbf{e_x} \begin{cases} 0 & : \quad \eta < 0 \\ \frac{E_0 c}{2\pi N_{on}\omega}(\eta\cos\eta - \sin\eta) & : \quad 0 \leq \eta \leq 2\pi N_{on} \\ \frac{E_0 c}{\omega}(\cos\eta - (\sin 2\pi N_{on})/2\pi N_{on}) & : \quad 2\pi N_{on} < \eta \leq 2\pi(N_{DUR} - N_{off}) \\ \frac{E_0 c}{2\pi N_{off}\omega}((2\pi N_{DUR} - \eta)\cos\eta + \sin\eta) & : \quad 2\pi(N_{DUR} - N_{off}) < \eta \leq 2\pi N_{DUR} \end{cases} \tag{3.8}$$

This vector potential is differentiable and its derivatives are continuous. Moreover, it depends exclusively on the spatial coordinate y and not on x. This circumstance is to play an important role for the numerical solution of the time-dependent Schrödinger equation by means of the split-operator method (see section (3.2)). The spatial dependence of

$\mathbf{A} = (A_x(y,t), 0, 0)$ on y is responsible for the existence of the laser magnetic field (3.7). Performing the dipole approximation means the neglect of this spatial dependence, i.e. y is set to zero. Taking into account that only the x-component $A_x(y,t)$ in the vector potential is non-vanishing results in the Hamiltonian employed for the simulations:

$$H(x,y,t) = \frac{1}{2}\mathbf{p}^2 + \frac{1}{c}A_x(y,t)p_x + \frac{1}{2c^2}A_x(y,t)^2 + V_{ion}(x,y) \tag{3.9}$$

3.1.2 The soft-core potential

The interaction of the electron with the nucleus (or nuclei) is naturally given by a Coulomb potential. However, in simulations in which the dimensions of the model system are reduced to one or two dimensions, the usage of a so-called soft-core potential is recommended [48]. The soft-core potential $V_{ion}(x,y)$ in the Hamiltonian (3.9) in the case of atomic ions possesses the following form:

$$V_{ion}(x,y) = -\frac{k}{\sqrt{s + x^2 + y^2}} \tag{3.10}$$

For large distances from the origin $(x,y) = (0,0)$ this potential possesses the same asymptotic behavior as the corresponding 2D Coulomb potential ($s = 0$). In contrast to the Coulomb potential the singularity at the origin is removed in the soft-core potential. The application of a soft-core potential for 1D or 2D simulations is justified by the circumstance that a corresponding 1D or 2D Coulomb potential would over-emphasize the influence of the nucleus on the electron in a 1D or 2D model system, respectively. The attraction of the nucleus would be too pronounced.
The parameters k and s in (3.10) are employed to match some eigenvalues of the field-free Hamiltonian (see (3.9) with $A_x(y,t)$ set to zero) with some eigenvalues of the corresponding real 3D system. This is accomplished by the methods outlined in section (3.4).

In the case of H_2^+ with clamped nuclei the soft-core potential $V_{ion}(x,y)$ is a superposition of two soft-core potentials (3.10):

$$V_{ion}(x,y) = -\sum_{k=1,2} \frac{1}{\sqrt{(x-x_k)^2 + (y-y_k)^2 + \epsilon}}\,, \tag{3.11}$$

where (x_1, y_1) and (x_2, y_2) are the positions of the nuclei. The positions are given by $x_{1,2} = \pm R/2 \cos\Theta$ and $y_{1,2} = \pm R/2 \sin\Theta$. The simulations are carried out for different fixed angles Θ between the molecular axis and the laser electric field. The nuclear separation R is set at 2 a.u.

3.2 The split-operator method

In this section we introduce the split-operator technique which has been employed in this work to solve the time-dependent Schrödinger equation with Hamiltonian (3.9) for

a one-electron system, i.e. a hydrogen-like atomic ion [2] and H_2^+ [3], respectively. The corresponding system is defined by the choice of the soft-core potential Eq. (3.10) and Eq. (3.11), respectively. In the framework of the theoretical investigation of laser-matter interactions the split-operator method has been successfully applied and can be viewed as a standard technique [49]. In the following description we refer to the 2D model system delineated in the previous section (3.1). Although the quantities of positions x, y in coordinate space or positions p_x, p_y in momentum space are denoted as in the previous section (3.1) one should be aware of the fact that for the implementation of the split-operator technique these quantities are discrete samples. The same is true for the electron wave function. At the very beginning of a computer run the grids in coordinate and momentum space of desired size are initialized. Then the initial wave function $\Psi(x, y, t = 0)$ is read in and propagated on the grids at discrete time steps. Before this, the initial wave function which is chosen as an eigenfunction of the field-free Hamiltonian has been obtained by the methods discussed in section (3.4).
The time evolution of the initial state $\Psi(x, y, t = 0)$ is governed by the time-dependent Schrödinger equation. Its formal solution can be expressed with the help of the short-time propagator:

$$U(x, y, t) = e^{-iH(x,y,t)\Delta t} , \tag{3.12}$$

since the wave function $\Psi(x, y, t+\Delta t)$ propagated by the small time increment Δt results from the application of (3.12) to $\Psi(x, y, t)$:

$$\Psi(x, y, t + \Delta t) \approx U(x, y, t)\Psi(x, y, t) \tag{3.13}$$

This implies that starting from $\Psi(x, y, t = 0)$ successive application of short-time propagators (3.12) allows of the computation of the solution of the time-dependent Schrödinger equation $\Psi(x, y, T)$ after a propagation period T. This circumstance is the starting point of the split-operator algorithm.
For further discussion the Hamiltonian $H(x, y, t)$ (3.9), as it is used in the simulations, is inserted into Eq. (3.12) and the advantageous splitting of this short-time propagator is demonstrated in this case:

$$U(x, y, t) = e^{-i\mathbf{p}^2\Delta t/4}\, e^{-iA_x(y,t)p_x\Delta t/c}\, e^{-i(A_x(y,t)^2/2c^2+V(x,y))\Delta t}\, e^{-i\mathbf{p}^2\Delta t/4} \tag{3.14}$$

One can show that this manner of splitting the exponential operators of the kinetic energy results in an error of the order of $(\Delta t)^3$. This arises from the non-commutativity of the split terms and can be explained by the Baker-Hausdorff-formula; for details see [50]. Thus, the whole propagation over the period T, which is divided into N small short-time intervals $\Delta t = T/N$, is accomplished by the following iterative scheme:

$$\Psi(x, y, T) \approx \exp(+i\mathbf{p}^2\Delta t/4)U(x, y, t_N)U(x, y, t_{N-1}) \ldots U(x, y, t_1) \exp(-i\mathbf{p}^2\Delta t/4)\Psi(x, y, 0) \tag{3.15}$$

with

$$\begin{aligned} U(x, y, t_i) = \exp(-i\mathbf{p}^2\Delta t/2) &\times \exp(-iA_x(y, t_i)p_x\Delta t) \\ &\times \exp(-i[A_x(y, t_i)^2/2c^2 + V(x, y)]\Delta t) \end{aligned} \tag{3.16}$$

[2] For results see chapter (4) for the ground state and chapter (5) for the first excited antisymmetric state.

[3] For results see chapter (5).

(with $i = 1 \ldots N$). Thus, the whole propagation consists essentially of the application of the operators $U(x, y, t_i)$ at times t_i. Note that in the derivation of (3.16) the term $\exp(-i\mathbf{p}^2\Delta t/2)$ arises from the successive application of short-time propagators (3.14) at different times t_{i-1} and t_i. In order to accomplish the scheme (3.15) with $U(x, y, t_i)$ (3.16) we remark that the application of the term $\exp(-i[A_x(y, t_i)^2/2c^2 + V(x, y)]\Delta t)$, which is solely dependent on the spatial coordinates and the time, results in a simple multiplication of a complex number with the wave function given in coordinate space. The exponential term $\exp(-iA_x(y, t_i)p_x\Delta t)$ mingles the spatial coordinate y with the momentum operator p_x which becomes the differential operator $-i\frac{\partial}{\partial x}$ in coordinate representation. Thus, applying the exponential operator $\exp(-iA_x(y, t_i)p_x\Delta t)$ numerically to an intermediate wave function in coordinate representation is problematic. This obstacle is overcome by means of the Fast Fourier Transform (FFT) of the coordinate-space wave function, i. e. a one-dimensional FFT with respect to x is performed on the intermediate wave function $\Psi(x, y, t)$:

$$\psi(x, y, t) \xrightarrow{\text{1d-FFT}} \tilde{\psi}(p_x, y, t) \tag{3.17}$$

The wave function $\tilde{\psi}(p_x, y, t)$ being in mixed representation is ready for the application of $\exp(-iA_x(y, t_i)p_x\Delta t)$; it merely represents the multiplication of complex numbers again. As for this step, it is vital for the success of this method that the vector potential $A_x(y, t)$ solely depends on the spatial coordinate y. If it also depended on x the performance of the 1d-FFT with respect to x would again lead to numerical differentiation with respect to x, thwarting the plan to circumvent numerical differentiation (in exponential operators !) with the help of Fourier transformation. In the next step a one-dimensional FFT with regard to y is performed on $\tilde{\psi}(p_x, p_y, t)$ which renders the wave function completely in momentum representation $\tilde{\psi}(p_x, p_y, t)$. This permits the convenient application of $\exp(-i\mathbf{p}^2\Delta t/2)$ avoiding explicit numerical differentiations [4] In order to switch back to coordinate-space representation a two-dimensional inverse FFT is applied to $\tilde{\Psi}(p_x, p_y, t)$. In practice, the FFT has been performed by the Fast Fourier transformation routines FFTW (www.fftw.org). The FFTW-routines also allow for a threaded FFT.

Finally, a few aspects which concern the choice of laser parameters and the properties of the grid and which are relevant in order to obtain converged results are mentioned:

- It is crucial for an adequate description of the electron dynamics in the laser field to choose sufficiently large grids in coordinate-space. The grid is large enough if a further increase of the grid size does not lead to changes in the computed results, i.e., in the computed observable quantities of interest, like, e.g., the center-of-mass trajectory or the harmonic spectrum. Of course, the grid size needed depends on

[4] We remark that there is also the possibility to make use of the Crank-Nicolson method [36] which is based on a finite difference scheme. However, the FFT method used in this work allows for more accurate results with respect to the application of the differentiation operators because all grid points, i.e. all available information, are taken into account in the case of FFT, while finite differences only employ the information provided by neighboring grid points. On the other hand, the FFT method is in general more time-consuming than a finite difference scheme which consists of the solution of linear equations in the end.

the applied laser intensity and laser frequency and on the binding energies of the considered atomic or molecular orbitals. To obtain a preliminary crude assessment of the necessary length L_x of the coordinate-space grid in laser polarization direction, the dynamics of a classical free electron in the laser field may be helpful:

$$L_x > \frac{E_0}{\omega^2}, \tag{3.18}$$

where E_0 is the electric peak amplitude of the laser field and ω its angular frequency. The quantity E_0/ω^2 is the classical quiver amplitude of a free electron in the laser field, see section (2.1).

In analogy to the estimate above, one can assess the necessary grid length in laser propagation direction L_y with the help of the distance travelled in the laser propagation direction by a classical free electron per optical cycle (see section (2.1)):

$$L_y > N_{\mathrm{DUR}} \frac{\pi}{2} \frac{E_0^2}{\omega^3 c} \tag{3.19}$$

(N_{DUR} denotes the whole number of laser cycles.)
However, even very large grids cannot fully prevent the electron wave packets ejected by the impact of a strong laser pulse from reaching the grid boundaries. In the wake of reflections of these wave packets at the grid boundaries, outgoing wave packets could interfere with reflected ones. This could result in unphysical effects in the quantities of interest. In order to avoid the reflection of the wave packets at the grid boundaries, the propagated wave function is multiplied at each time step with a $\cos^{1/8}$-mask function [51]:

$$D(x) = \begin{cases} 1 & \text{if} \quad x \leq r_0 \\ \cos^{1/8}\left(\frac{\pi}{2}\frac{x-r_o}{L_d}\right) & \text{if} \quad r_0 < x < r_0 + L_d, \end{cases} \tag{3.20}$$

where r_0 denotes the length of the un-damped part of the grid and L_d describes the length of the part of the grid in which the propagated wave function is damped. This function represents the mask function for damping in the laser polarization direction. In the laser propagation direction an analogous function is used.

The application of absorbing boundaries leads to the fact that the norm of the wave function cannot remain unity during the propagation. A severe loss of the norm indicates too small grids.

- As for the grid in momentum-space, all momentum components of the wave function have to be presentable. This means that the maximum momentum which the momentum wave function possesses has to be smaller than the maximum momentum p_{max} being presentable on the momentum grid according to Nyquist's sampling theorem [52]. This has to hold both in the laser polarization direction and in the laser propagation direction. For example, in laser polarization direction:

$$p_{\mathrm{max}} = \frac{\pi}{\Delta x}, \tag{3.21}$$

where Δx is the grid spacing, i.e., the distance of two neighbored grid points. Thus, sufficiently small grid spacing Δx in the laser polarization direction ensures that the above mentioned criterion is met. For the laser propagation direction, there are analogous considerations. A rough estimate of the maximum momentum can be accomplished by the quiver momentum amplitude of a classical free electron in the laser field given by E_0/ω.

- The choice of the temporal spacing Δt is crucial for the convergence of the split-operator algorithm. To ensure convergence, several computer runs with different Δt are helpful. If there are no differences observable in the results for decreasing Δt, the temporal spacing Δt is sufficiently small. Moreover, for the computation of the harmonic spectrum as the modulus square of the Fourier transform of the dipole acceleration one should choose a sufficiently small Δt, so that a densely sampled dipole acceleration array is provided. This is again required by the sampling theorem which predicts a maximum presentable harmonic energy of

$$E_{\max} = \frac{\pi}{\Delta t}. \tag{3.22}$$

  This $E_{\max}$ should be large enough in order to be able to represent the cut-off energy $I_p + 3.17\, U_p$ of the harmonic spectrum.

Finally, it should be mentioned that the need for large grids and small grid spacings results in both large memory requirements and long computation durations. Of course, small Δt also renders long computer runs. As a result, in practice one has to figure out appropriate parameters for each physical system under consideration ensuring the accuracy of the computations on the one hand and limiting the durations of computer runs on the other hand.

3.3 Computation of observable quantities

During the propagation by the split-operator algorithm which yields the wave function $\psi(x, y, t)$ for each discrete time t it is possible to infer observable quantities which characterize the electron dynamics in the presence of an atomic or molecular core potential under the influence of a laser pulse. Effects in the electron dynamics are closely related to specific effects occurring in these observable quantities.

The fact that the wave function $\psi(x, y, t)$ is computed at each time step permits immediately the computation of the probability density $\rho(x, y, t) = |\psi(x, y, t)|^2$ of the electron. This renders the direct illustration of the wave packet dynamics possible and with this helps to gain insight into the ionization behavior of the investigated system.

It becomes apparent that there is plenty of ionization for weakly bound systems which are exposed to a strong laser pulse, i.e., a significant population of the continuum takes place (see H_2^+ in the laser field in Fig. 5.13). In this case the wave packet dynamics resembles the dynamics of a free wave packet in the laser field. Thus, a direct illustration of the density $\rho(x, y, t)$ is possible. In contrast to this, if an atomic system with high binding energy is used (see atomic ions in the laser field in Fig. 5.22) only a minor fraction of the population is transferred into the continuum, whereas the major part of the population remains at the position of the nucleus. In order to illustrate the small tunnelled wave packets, it is recommendable to depict the quantity $\log \rho(x, y, t)$ in this case.

By means of two-dimensional spatial integration of the density $\rho(x, y, t)$ the norm of the wave function can be determined at every time. In terms of absorbing boundaries, one is enabled to assess crudely the ionization behavior of the system during the propagation by keeping track of the norm.

During the propagation of the wave function $\psi(x, y, t)$ it is possible to study the occupation of bound eigenstates $\psi_{\text{bound}}(x, y)$, which have been computed in advance, with the spectral method for example. This can be accomplished by projecting the propagated wave function $\psi(x, y, t)$ onto the bound states $\psi_{\text{bound}}(x, y)$:

$$\left|\langle\psi_{\text{bound}}(x, y)|\psi(x, y, t)\rangle\right|^2 = \int_{y_{\min}}^{y_{\max}} \int_{x_{\min}}^{x_{\max}} \psi^*_{\text{bound}}(x, y)\psi(x, y, t)\, dx\, dy.$$

Of course, integration means here numerical integration, i.e., using sums. The boundaries of the integrals are identical with the boundaries of the grid.

For the purpose of comparison with classical dynamics, the computation of center-of-mass trajectories of the electronic wave function $\psi(x, y, t)$ is obvious. The position expectation values $\langle x\rangle(t)$ and $\langle y\rangle(t)$ in laser polarization direction and laser propagation direction are given as follows:

$$\langle x\rangle = \int_{y_{min}}^{y_{max}} \int_{x_{min}}^{x_{max}} x \mid \psi(x, y, t) \mid^2 \, dxdy \tag{3.23}$$

and

$$\langle y\rangle = \int_{y_{min}}^{y_{max}} \int_{x_{min}}^{x_{max}} y \mid \psi(x, y, t) \mid^2 \, dxdy \,, \tag{3.24}$$

respectively. Strong ionization can also be read off the behavior of the center-of-mass trajectories $\langle x\rangle(t)$ and $\langle y\rangle(t)$, respectively, if the grids have been chosen too small in a computer test run. In this case, outgoing wave packets are absorbed after a certain time, which results in an unphysical displacement of the center-of-mass. Thus, the center-of-mass trajectories may help to find appropriate grid sizes.

Moreover, the radiation that is emitted during the interaction of an atomic or molecular orbital with a strong laser pulse can be computed. The quantity which is directly amenable to the simulation and which characterizes the emission of radiation is either the electric dipole moment or the dipole acceleration. The electric dipole moment is—apart from a factor which represents the charge—identical with the center-of-mass trajectories $\langle x\rangle(t)$ or $\langle y\rangle(t)$, respectively.

It has been shown that the computation of harmonic spectra using the dipole acceleration is more advantageous[5]. This is due to the circumstance that harmonic spectra computed by means of the dipole moment may be disturbed by a stronger background noise [53]. The dipole acceleration in the laser polarization direction $a_x(t)$ and the one in the laser propagation direction $a_y(t)$ are proportional to the corresponding emitted electric fields if the velocity of the electron is small in comparison with the speed of light. The general expressions for the fields in the classical case are found in [36], Eq. (10.7) therein. The proportionality of dipole acceleration and electric field mentioned above is valid if the electron velocity v fulfils $(v/c) \ll 1$. (To be precise, in this approximation, the electric field is proportional to $\mathbf{n} \times \mathbf{n} \times \mathbf{a}$, where $\mathbf{n}$ is a unit vector in the observation direction and $\mathbf{a}$ is the dipole acceleration vector.)

On the other hand, the dipole accelerations $a_x(t)$ and $a_y(t)$ can be obtained by the direct numerical differentiation of the center-of-mass trajectories $\langle x\rangle(t)$ and $\langle y\rangle(t)$, respectively:

$$a_x(t) = \frac{d^2}{dt^2}\langle x\rangle(t)$$

and

$$a_y(t) = \frac{d^2}{dt^2}\langle y\rangle(t).$$

Depending on the specific system and the laser parameters, numerical differentiation might be problematic, i.e. it might lead to increased noise in the harmonic spectrum. On the other hand, the application of Ehrenfest's theorem yields formulas which can be evaluated during the computer run:

$$a_x(t) = \int_{y_{\min}}^{y_{\max}} \int_{x_{\min}}^{x_{\max}} \psi^*(x,y,t)\left(-\frac{\partial}{\partial x}V_{\text{ion}}(x,y)\right)\psi(x,y,t)\,dx\,dy \tag{3.25}$$

[5]Under the condition that the center-of-mass trajectory $\langle x\rangle(t=0) = 0$ at the beginning of the propagation (this is always the case) and provided that at the end of the propagation $\langle x\rangle(t=T) = 0$ (this requirement is questionable and depends on the specific case) two-fold partial integration yields the following relation of spectra based on the dipole acceleration and the ones computed via the dipole moment:

$$\left|\int_0^T \frac{d^2}{dt^2}\langle x\rangle(t)e^{i\omega t}dt\right|^2 \sim \omega^4\left|\int_0^T \langle x\rangle(t)e^{i\omega t}dt\right|^2$$

and

$$a_y(t) = \int_{y_{\min}}^{y_{\max}} \int_{x_{\min}}^{x_{\max}} \psi^*(x,y,t)\left(-\frac{\partial}{\partial y} V_{\text{ion}}(x,y)\right)\psi(x,y,t)\, dx\, dy. \tag{3.26}$$

Hereby, the expectation value of the laser electric field is neglected, since it only contributes to the fundamental and low harmonic orders.

The advantage of employing the spatial derivative of the core potential consists in the fact that only the wave packet dynamics in the vicinity of the core potential plays a role, for remote from the nucleus $-\frac{\partial V_{\text{ion}}}{\partial x}$ and $-\frac{\partial V_{\text{ion}}}{\partial y}$ are negligible and thus do not contribute substantially to the integrals (3.25) and (3.26), respectively.

Employing the center-of-mass trajectory, parts of the wave function may become important which are adjacent to the grid boundaries and are thus damped. This might give rise to spurious effects in the dipole acceleration and the harmonic spectrum. Which method for the computation of the dipole acceleration is applied is indicated in each chapter presenting the results (see chapter (4) and chapter (5)). The harmonic spectrum is computed as the modulus square of the windowed Fourier transform of the dipole acceleration

$$\left| \int a_x(t) w(t) e^{i\omega t} dt \right|^2$$

and

$$\left| \int a_y(t) w(t) e^{i\omega t} dt \right|^2.$$

Since the dipole acceleration is only available on a finite time interval, it is good practice to multiply the dipole acceleration with the window function $w(t)$ (Hanning window (3.34)) prior to the Fourier transformation. By this measure, unphysical features in the spectrum which are due to the finiteness of the dipole acceleration array are suppressed.

3.4 Computation of eigenstates

In this section we introduce the two numerical methods which have been employed to compute the initial states for the propagation procedure presented in the previous section. These initial states are eigenfunctions of the corresponding field-free Hamiltonian. The two methods permit the determination of eigenvalues and eigenfunctions of the time-independent Schrödinger equation.
In practice, we have taken the following proceeding: By a first preliminary choice of the soft-core parameter a certain soft-core potential has been taken into consideration. The initial testing wave function has been propagated (laser field switched off) and the autocorrelation function of this initial wave function with the propagated wave function has been computed. One obtains the energy eigenvalue spectrum of this specific potential by means of the windowed Fourier transform of the autocorrelation function. By varying the soft-core parameter and subsequent propagation one can opt for a desired position of the ground state energy or the position of an energy eigenvalue belonging to an excited state of the potential. Thus, the energy eigenvalues of the desired initial states are adapted to the corresponding eigenvalues of the real system. After having decided for certain soft-core parameters, the corresponding eigenfunctions can be computed. For this purpose, *propagation in imaginary time* and the *spectral method* are especially suitable in the context of an existing code for wave packet propagation. Both methods can be implemented in addition to the code of the propagation method without difficulty.

3.4.1 The spectral method

The following presentation of the spectral method is based on [54]. We look for eigenvalues E_n and eigenfunctions $u_{nj}(x, y)$ of the time-independent Schrödinger equation:

$$-\frac{1}{2}\left(\frac{\partial^2}{\partial x^2}+\frac{\partial^2}{\partial y^2}\right)u_{nj}+Vu_{nj}=E_n u_{nj}, \tag{3.27}$$

where $V(x, y)$ represents a specific potential. In our case it is either a soft-core potential (3.10), or a double-well soft-core potential (3.11).

The index j is used to distinguish states within a degenerate set. The spectral method consists of two steps. In the first one, an initial testing wave function $\psi(x, y, 0)$ is propagated according to the time-dependent Schrödinger equation

$$i\frac{\partial\psi}{\partial t}=-\frac{1}{2}\left(\frac{\partial^2}{\partial x^2}+\frac{\partial^2}{\partial y^2}\right)\psi+V(x,y)\psi. \tag{3.28}$$

This is accomplished by the method described in section (3.2) with the laser field switched off.

For each time step during the propagation, the autocorrelation $P(t)$ is computed corre-

sponding to

$$P(t) = \langle \psi(x,y,0) | \psi(x,y,t) \rangle \tag{3.29}$$

$$= \iint \psi^*(x,y,0)\psi(x,y,t)\, dx\, dy. \tag{3.30}$$

If the initial wave function $\psi(x,y,0)$ represents the following superposition of eigenfunctions u_{nj} with coefficients A_{nj}: $\psi(x,y,0) = \sum_{n,j} A_{nj} u_{nj}(x,y)$, the wave function $\psi(x,y,t)$, propagated according to Eq.(3.28) possesses the following form:

$$\psi(x,y,t) = \sum_{n,j} A_{nj} u_{nj} \exp(-iE_n t). \tag{3.31}$$

Using this expression in Eq.(3.30), the autocorrelation $P(t)$ results in

$$P(t) = \sum_{n,j} |A_{nj}|^2 \exp(-iE_n t). \tag{3.32}$$

The Fourier transform of Eq.(3.32) reveals the eigenenergy spectrum belonging to the potential $V(x,y)$:

$$P(E) = \sum_{n,j} |A_{nj}|^2 \delta(E - E_n). \tag{3.33}$$

However, the δ-peak structure of this spectrum is due to an infinite record of the autocorrelation $P(t)$. In practice, the autocorrelation is only available over a limited propagation period T. This implies that the clear ideal δ-peak structure is not given in practice but the appearance of additional side lobes to the peaks at the energy eigenvalues is given by the finite propagation period T.

In order to suppress the disturbing side lobes in the energy spectrum it is advisable to multiply the right-hand side of Eq. (3.32) by the normalized window function $w(t)/T$, where

$$w(t) = \begin{cases} 1 - \cos(2\pi t/T), & \text{if} \quad 0 \le t \le T, \\ 0, & \text{if} \quad t > T \end{cases}. \tag{3.34}$$

This results in

$$P(E) = \sum_n W_n L(E - E_n)\ . \tag{3.35}$$

The weights $W_n = \sum_j |A_{nj}|^2$ are determined by the choice of the initial testing wave function $\Psi(x,y,0)$. The lineshape function $L(E-E_n)$ for each individual resonance at E_n is given by

$$\begin{aligned} L(E-E_n) &= \frac{1}{T}\int_0^T \exp[i(E-E_n)t]\, w(t)\, dt \\ &= \frac{\exp[i(E-E_n)T]-1}{i(E-E_n)T} - \frac{1}{2}\left[\frac{\exp\{i[(E-E_n)T+2\pi]\}-1}{i[(E-E_n)T+2\pi]}\right. \\ &\quad \left. + \frac{\exp\{i[(E-E_n)T-2\pi]\}-1}{i[(E-E_n)T-2\pi]}\right] \end{aligned} \tag{3.36}$$

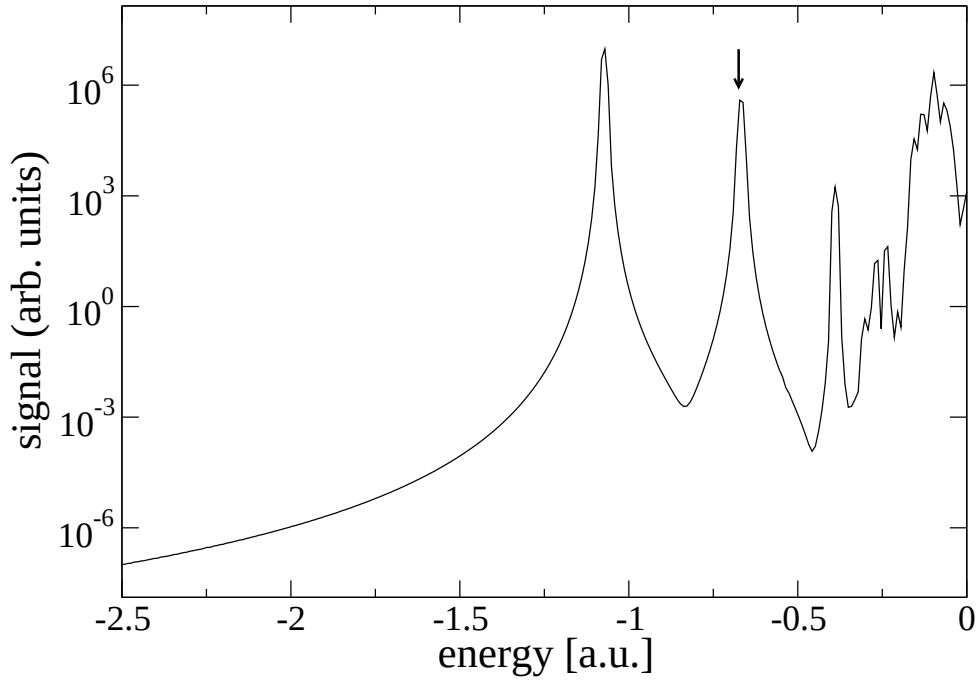

Figure 3.1: Energy spectrum of H_2^+ modelled by the soft-core potential (3.11) with ϵ =0.58. The arrow indicates the eigenenergy of -0.67 a.u. of the first (purely electronically) excited antisymmetric state.

The application of the window function $w(t)$ before Fourier transforming the autocorrelation function $P(t)$ helps to reduce the amplitudes of the side lobes and with this permits an accurate determination of the positions of the energy eigenvalues E_n in the spectrum (3.35). Note that the choice of the initial testing wave function $\psi(x, y, 0)$ is relevant for the occurrence of the energy eigenvalues E_n in the spectrum since the coefficients A_{nj} in $\psi(x, y, 0)$ also appear in Eq. (3.35). If some of them vanish, so does the eigenvalue within the spectrum. Thus, it is recommendable to perform a computer run with a quite arbitrary initial testing wave function which contains as many eigenfunctions u_{nj} as possible in order to be able to observe all energy eigenvalues E_n belonging to the potential $V(x, y)$. If one chose, e.g., an antisymmetric $\Psi(x, y, 0)$ only energy eigenvalues E_n belonging to antisymmetric eigenfunctions u_{nj} would be visible in the energy spectrum.

Figure (3.1) shows, for example, the energy spectrum of the double-well soft-core potential applied in chapter (5). The parameters of this soft-core potential have been determined so that the first excited state possesses an eigenenergy of -0.67 a.u. (indicated by the arrow in the figure).

In the second step of the spectral method one focuses on the computation of eigenfunctions for which one has obtained the energy eigenvalues E_n in the first step. Multiplying both

sides of Eq. (3.31) by $T^{-1}w(t)\exp(iEt)$ and subsequent integration from 0 to T yields:

$$\begin{aligned}\psi(x,y,E) &= \frac{1}{T}\int_0^T \psi(x,y,t)w(t)\exp(iEt)\,dt \\ &= \sum_{n,j} A_{nj}u_{nj}(x,y)L(E-E_n)\end{aligned} \tag{3.37}$$

For a specific eigenvalue $E_{n'}$ one obtains:

$$\psi(x,y,E_{n'}) = \sum_j A_{n'j}u_{n'j}(x,y)L(0) + {\sum_{n,j}}' A_{nj}u_{nj}(x,y)L(E_{n'}-E_n)\ . \tag{3.38}$$

For negligible overlap between resonant terms in Eq.(3.37), the second sum in Eq.(3.38) can be neglected, which yields:

$$\psi(x,y,E_n) = \sum_j A_{nj}u_{nj}(x,y)L(0) \tag{3.39}$$

For large propagation periods T the lineshape function $L(E-E_n)$ becomes pointed. This justifies Eq.(3.39) in the limit of sufficiently large T and accounts for the need of long propagation in order to obtain accurate eigenfunctions. Thus, the numerical computation of a particular eigenfunction u_n is reduced to one numerical integration (performed in the second computer run with known E_n):

$$u_n(x,y) = \text{const} \times \int_0^T \psi(x,y,t)\,w(t)\,\exp(iE_nt)\,dt = \text{const} \times \psi(x,y,E_n) \tag{3.40}$$

At the end of the integration procedure, normalization gives the desired eigenfunction. With respect to the computation of eigenfunctions the choice of the initial testing wave function can be decisive as Eq.(3.39) implies. At most one member of the degenerate set of states should be contained in $\psi(x,y,0)$ in order to achieve the desired u_{nj} and not a superposition of degenerate states. Furthermore, if a certain type of symmetry for the desired eigenfunction is given one should take this symmetry also into consideration for $\psi(x,y,0)$. In practice, an advantage of the spectral method consists in the fact that the stability of the computed eigenfunctions can be amended in successive computer runs. As a test of stability of the numerical eigenfunction, the autocorrelation is required to be unity for a large propagation period if this numerical eigenfunction serves as an initial wave function.

3.4.2 Propagation in imaginary time

Propagation in imaginary time represents in first place a method to obtain numerically the ground state energy and wave function of the time-independent Schrödinger equation. As terminology suggests, the basic step of this method consists in the substitution of the variable time t by imaginary time τ: $t \to -i\tau$. Therefore, it makes the circumstance plausible that this method can be implemented along with the implementation of the

split-operator propagation technique, since only minor changes to the latter are required. Similar to the spectral method, this technique also yields energy eigenvalues and eigenfunctions after propagation of an initial testing wave function. Further reading on the propagation in imaginary time is given in [55]. Let us assume that the time-independent Schrödinger equation possesses eigenvalues E_n and eigenfunctions ψ_n:

$$H\psi_n = E_n\psi_n, \qquad n = 0, 1, 2, \ldots \tag{3.41}$$

The substitution $t \to -i\tau$ in the time-dependent Schrödinger equation $i\frac{\partial}{\partial t}\psi = H\psi$ with the time-independent Hamiltonian H results in:

$$\frac{\partial}{\partial \tau}\tilde{\psi} = -H\tilde{\psi} \tag{3.42}$$

with $\tilde{\psi}(x, y, \tau) := \psi(x, y, -it)$. Assuming that the initial testing wave function $\psi(x, y, t = 0)$ possesses the following expansion into eigenfunctions ψ_n

$$\psi(x, y, t = 0) = \sum_n a_n\psi_n(x, y) \tag{3.43}$$

yields for the propagated solution of the time-dependent Schrödinger equation

$$\psi(x, y, t) = \exp(-iHt)\psi(x, y, t = 0) = \sum_n a_n \exp(-iE_nt)\psi_n(x, y). \tag{3.44}$$

The substitution $t \to -i\tau$ in the equation above leads to

$$\tilde{\psi}(x, y, \tau) = \exp(-H\tau)\psi(x, y, t = 0) = \sum_n a_n \exp(-E_n\tau)\psi_n(x, y). \tag{3.45}$$

Inserting this $\tilde{\psi}$ into Eq.(3.44) confirms that $\tilde{\psi}(x, y, \tau)$ is a solution of Eq.(3.42). Furthermore, we have

$$\tilde{\psi}(x, y, \tau = 0) = \psi(x, y, 0). \tag{3.46}$$

In the following it is shown how the wave function $\tilde{\psi}(x, y, \tau)$ propagated in imaginary time serves to compute the ground state energy E_0 and the ground state wave function ψ_0. With Eq.(3.45) one obtains:

$$\langle\tilde{\psi}|H|\tilde{\psi}\rangle = \sum_n \sum_{n'} a_n a_{n'} \exp[-(E_n + E_{n'})\tau]E_n\langle\psi_{n'}|\psi_n\rangle, \tag{3.47}$$

$$\langle\tilde{\psi}|\tilde{\psi}\rangle = \sum_n \sum_{n'} a_n a_{n'} \exp[-(E_n + E_{n'})\tau]\langle\psi_{n'}|\psi_n\rangle. \tag{3.48}$$

Taking only the dominant $(n = 0, n' = 0)$-terms for large τ into account yields the ground state energy:

$$E_0 = \lim_{\tau\to\infty} \frac{\langle\tilde{\psi}|H|\tilde{\psi}\rangle}{\langle\tilde{\psi}|\tilde{\psi}\rangle}. \tag{3.49}$$

Knowing the ground state energy, we consider $(a_0 \neq 0)$:

$$\exp(E_0\tau)\tilde{\psi}(x, y, \tau) = a_0\psi_0(x, y) + \sum_{n>0} a_n \exp[-(E_n - E_0)\tau]\psi_n(x, y). \tag{3.50}$$

This gives the ground state wave function:

$$\psi_0(x,y) \propto \lim_{\tau\to\infty} \exp(E_0\tau)\tilde{\psi}(x,y,\tau). \tag{3.51}$$

Hence, considering Eq.(3.45) and Eq.(3.46), the implementation of the procedure becomes evident: An initial testing wave function is read in like for the propagation in real time. However, this wave function is propagated by means of the operator $\exp(-H\tau)$, i.e., in contrast to the short-time propagator in real time the complex exponential terms are replaced by real ones. This allows of a convenient implementation of the method if the code for the standard wave packet propagation already exists. Similar to the spectral method attention should be paid to the choice of the initial testing wave function in which the ground state must be contained, i.e. $a_0 \neq 0$.

After propagation, Eq.(3.47) yields the ground state energy. If this has been determined, Eq.(3.51) gives the ground state wave function. After having computed the ground state wave function, it is thinkable to procure the first excited state. For this purpose the ground state wave function should be projected onto the initial testing wave function, this gives a_0, and subsequently $a_0\psi_0(x,y)$ should be subtracted from the initial wave function. This prepared wave function would then yield the eigenvalue and the eigenfunction of the first excited state (if $a_1 \neq 0$). This specific procedure has not been performed in this thesis.

3.4.3 The methods in practice

In this work, propagation in imaginary time and subsequently the spectral method have been employed to generate the ground state of an atomic system, see chapter (4). For the computation of excited atomic and molecular orbitals, the spectral method has been applied exclusively, see chapter (5). On the other hand, the spectral method has the advantage of providing more stable eigenstates by successive application. (It has to be ensured that the numerical eigenstates remain stable over the period of laser interaction.) On the other hand, the spectral method permits the direct computation of excited eigenfunctions, i.e., there is no need for the computation of energetically lower eigenfunctions in advance.

Propagation in imaginary time has turned out to be suitable for a relatively quick computation of a crude version of the ground state wave function. The spectral method is more time-consuming since particularly long propagation is needed in order to achieve accurate results.

3.5 Monte Carlo simulations

In this section the classical Monte Carlo method which is based on the solution of the classical equations of motion and stochastics is presented. This method is by far less demanding in view of implementation and computer hardware requirements than the direct numerical integration of the time-dependent Schrödinger equation. However, since this approach is based on classical mechanics, it only serves to mimic the spreading of (quasi-)free quantum mechanical wave packets driven by a laser field. The modelling of interference effects which are essential for high-order harmonic generation (interference of re-colliding wave packets with the initial state) is beyond the skills of this method. Therefore, almost all results in this thesis have been obtained by the numerical integration of the Schrödinger equation. Monte Carlo simulations have only been employed to mimic the wave packet spreading of a wave packet with a nodal line in order to demonstrate the displacement of these wave packets in the laser propagation direction due to the influence of the laser magnetic field (see section (5)). Thus, the Monte Carlo method is explained in the manner it is used in this thesis. For a detailed study of this method see [56].

The Monte Carlo method is based on the uncertainty with respect to position and momentum of a quantum mechanical wave packet. In our case, this initial wave packet $\psi(x, y, t = 0)$ is an eigenfunction of the field-free Hamiltonian. With the help of Fourier transformations (FFTW), its counterpart in momentum space $\tilde{\psi}(p_x, p_y, t = 0)$ is obtained. These wave functions yield the position and momentum distribution according to the densities $\rho(x, y) = |\psi(x, y, t = 0)|^2$ and $\tilde{\rho}(p_x, p_y) = |\tilde{\psi}(p_x, p_y, t = 0)|^2$, respectively. According to these distributions, the initial conditions for numerous classical trajectories are determined. Then, for each initial condition the corresponding classical equations of motion are solved. Making a snapshot after time t, the variety of classical trajectories $\big(x(t), y(t)\big)$ gives a distribution of points in the x-y–plane. This distribution is expected to reflect the corresponding distribution belonging to the propagated wave function $\psi(x, y, t)$. Thus, the objective of the Monte Carlo method is to mimic wave packet spreading.

The initial conditions for $x(t = 0)$, $p_x(t = 0)$, $y(t = 0)$, and $p_y(t = 0)$ are drawn in accordance with the distributions $\rho(x, y)$ and $\tilde{\rho}(p_x, p_y)$. This is performed by means of the rejection method [52]. In this procedure, the maximum of each distribution is determined. Then, equally distributed random variables between zero and each maximum are drawn (srand-function in C). Subsequently, a value ρ_0 or $\tilde{\rho}_0$ of the $\rho(x, y)$-array or the $\tilde{\rho}(p_x, p_y)$-array is picket out according to the equal distributions, respectively. This corresponds to randomly drawing triples $\big(x, y, \rho(x, y)\big)$ on the position grid or $\big(p_x, p_y, \tilde{\rho}(p_x, p_y)\big)$ on the momentum grid, respectively. If $\rho_0 \leq \rho(x, y)$ or $\tilde{\rho}_0 \leq \tilde{\rho}(p_x, p_y)$, the corresponding triples are accepted. This means that the first two coordinates of the triple have been drawn as initial values according to the distribution $\rho(x, y)$ or $\tilde{\rho}(p_x, p_y)$, respectively.

For smaller values of the probability densities $\rho(x, y)$ or $\tilde{\rho}(p_x, p_y)$, the rejection of the corresponding triple is more likely, which explains the functioning of the rejection method.

After having drawn a large number of initial conditions, the solution of the classical equations of motion for each initial condition is accomplished. For this purpose, the canonical equations with the Hamilton function H are solved by the classical Runge-Kutta method of fourth order [57],

$$\dot{x}(t) = \frac{\partial H}{\partial p_x} = p_x(t) + \frac{1}{c} A_x\big(y(t), t\big), \tag{3.52}$$

$$\dot{y}(t) = \frac{\partial H}{\partial p_y} = p_y(t), \tag{3.53}$$

$$\dot{p}_x(t) = -\frac{\partial H}{\partial x} = -\frac{\partial V_{\text{ion}}}{\partial x}\big(x(t), y(t)\big), \tag{3.54}$$

$$\dot{p}_y(t) = -\frac{\partial H}{\partial y} = -\frac{1}{c}\frac{\partial A_x}{\partial y}\big(y(t), t\big)\left(p_x + \frac{1}{c} A_x\big(y(t), t\big)\right) - \frac{\partial V_{\text{ion}}}{\partial y}\big(x(t), y(t)\big). \tag{3.55}$$

The Hamilton function H results from interpreting the Hamilton operator (3.9) as a classical Hamilton function. The vector potential is given by (3.8). The numerical solution of this system of ordinary coupled differential equations gives a large number of trajectories $\big(x(t), y(t)\big)$ reflecting the wave packet spreading of the propagated wave function (see chapter 5).

Chapter 4

Results I: HHG in the presence of a static magnetic field

4.1 Overview and motivation

As we have learnt in chapter (2), a HHG-spectrum possesses the following typical form: After a considerable decrease in intensity there is a frequency region of multiples of the irradiated laser frequency forming an intensity plateau which breaks off at a certain cut-off frequency. Meanwhile there have been numerous investigations which pursue the aim to find a way to enhance the signal of the harmonic peaks or to shift the cut-off frequency towards higher frequencies: As for the increase of the cut-off frequency a laser-driven atomic system within a parabolic potential has been investigated by [58]. The authors showed that the cut-off frequency can be enhanced by this configuration. Furthermore, various schemes which can be used to modify the HHG-process have been studied theoretically in [59]. These schemes consist of both subjecting a molecular system to a combination of two laser fields, whereas the frequency of the second field is a multiple of the first one, and the addition of electric and magnetic fields to the driving laser field.
Adding a static magnetic field to the laser field can be quite beneficial. Thus, we intend to give a survey of theoretical investigations done so far focusing on a system which consists of an electron, atom or molecule that is subjected to a combination of laser and static magnetic field: Connerade and Keitel showed in 1996 that the laser-induced relativistic dynamics of an electron in an atomic potential can be modified by adding a static magnetic field directed parallel to the laser propagation direction so that even harmonics occur in the HHG-spectrum. This investigation is based on classical Monte Carlo simulations [60]. Salamin and Faisal investigated a classical free electron brought to relativistic dynamics by an elliptically polarized laser field [61]. An additional static magnetic field which is parallel to the laser propagation direction induces supplementary wiggles in the helix motion of the electron. Depending on the observation direction either one further harmonic peak besides the Thomson peak shows up or infinitely many peaks of indistinct structure come up due to the presence of the static magnetic field.

Whereas in the two previously mentioned papers an intense laser field caused relativistic

dynamics, work of Wagner et al. [62] pointed out that moderately intense laser fields are able to induce a relativistic electron motion by means of an additional static magnetic field. The authors discovered relativistic resonance effects possessing salient characteristics as the formation of ring-like charge distributions of relatively large extension. As a further signature of these relativistic resonances the enhancement of the harmonic signal was reported. In a non-relativistic context Zuo et al. [59] have found by numerical integration of the time-dependent Schrödinger equation that the signal strength in the HHG-spectrum can be increased if a static magnetic field directed parallel to the laser polarization direction is added to a two-color laser field interacting with the H_2^+ molecular ion. However, the applied magnetic field has a tremendous value of $0.47 \cdot 10^9$G. The authors attribute this effect to the suppression of wave packet spreading. This leads to more efficient recollisions. The same mechanism has been seen at work by Milošević et al. [63]: Also non-relativistically, the same configuration of laser and static magnetic field is responsible for the enhancement of the HHG signal emitted by a H^- ion and an argon atom that are subjected to these fields. By applying the strong field approximation the authors discovered that the increase in harmonic strength is particularly efficient if the following conditions are fulfilled: the static magnetic field should induce an electron motion so that a multiple of the classical cyclotron period is equal to the return time of the ionized electron. Thus, adding a static magnetic field of appropriate strength can result in an enhancement of the harmonic intensity by orders of magnitudes. In this work the authors also point out that the cut-off frequency can be slightly shifted towards higher frequencies. Another work [64] also concerning the generation of HHG-radiation in a non-relativistic regime considers the H-atom subjected to a linearly polarized laser field and an additional static magnetic field which is directed perpendicular to both the laser electric field component and the laser propagation direction. This investigation involves the solution of the time-dependent Schrödinger equation in three dimensions. The authors discovered that a super strong static magnetic field in the order of 10 kT induces very efficiently an additional wiggly electron motion. This gives rise to the formation of a second plateau in the HHG-spectrum with a considerably increased cut-off frequency.

The papers surveyed above which study high harmonic generation for an atomic or molecular system have in common that the physical system (atom/molecule plus laser and static magnetic field) has to meet resonance criteria in order to be able to observe a distinct effect in the spectrum [59], [62], [63], [64]. These resonance criteria require that the cyclotron frequency must be of the order of the applied laser frequency. This implies that super strong static magnetic fields have to be used in order to meet these criteria and to perceive significant effects in the spectrum. In contrast to these papers, we follow a different approach in this chapter: We do not seek to reach resonances in our system. Instead, we found that relatively weak magnetic fields (30 T) cause observable effects in the spectrum that arises from the electron drift in the laser propagation direction. For these effects no resonance conditions as mentioned above have to be fulfilled [1]. To the best of our knowledge the impact of a static magnetic field on this radiation spectrum has not

[1] If we attempted to reach a cyclotron frequency $\omega_c = B_{stat}/c$ in the order of the applied laser frequency ω_L =0.058 a.u. (which corresponds to a laser wavelength of 780 nm) a static magnetic field B_{stat} of 14 kT would be required.

been studied before within a full quantum mechanical treatment beyond the dipole approximation. Employing the dipole approximation Tong and Chu [64] found that a super strong static magnetic field of the order of 10 kT causes the emission of harmonics polarized in laser propagation direction, but in this case the generation of these harmonics is due to this strong static magnetic field (resonance effect). In their study they could safely neglect the laser magnetic field. Without static magnetic field, high harmonic radiation polarized in laser propagation direction was discussed in [65]. Since we found that this radiation is more sensitive to the influence of a static magnetic field than the ordinary HHG radiation which is polarized along the laser polarization direction we are able to observe distinct effects in this radiation spectrum by employing weak static magnetic fields [66]. No resonance criteria have to be met. Thus, on one the hand our approach is interesting with regard to HHG experiments in combined laser and static magnetic fields since the effects in the spectrum are distinct and occur at experimentally accessible magnetic field strengths. Consequently, we attempted to employ parameters in our simulation that are in the scope of experimental realization. On the other hand our approach may also spark some interest from a theoretical point of view as the impact of the static magnetic field on the radiation which is polarized in laser propagation direction can only be studied if the laser magnetic field component is taken into account in our simulation. In contrast to this, the dipole approximation can be carried out if the impact of a static magnetic field on the ordinary HHG spectrum is studied and the velocity of the ionized electron is small in comparison with the speed of light [59], [63].

We solve the time-dependent Schrödinger equation numerically for a He^+ model ion which is subjected to a linearly polarized laser pulse and a static magnetic field. The model ion should in first place represent an atomic one-electron system; the method and results presented in this work can in principle be applied to other atomic species. However, the radiation which is in the focus of this chapter cannot be detected in gas targets in forward direction since the single atom radiation does not propagate in this direction; other directions are problematic because of missing phase-matching. As a way out, we propose to detect this radiation in certain angles θ to the laser propagation direction in crystals or crystal-like structures in order to realize the concept of this chapter experimentally. According to section (2.3.5) and [46], the harmonic waves which satisfy a Bragg condition add up constructively and are therefore observable in a certain angle θ to the laser propagation direction; the considerations leading to this result in [46] remain valid for the kind of harmonic radiation we focus on (second scheme in [46]; in our case forward detection $\theta = 0°$ is precluded). The harmonic radiation of frequency ω ($\omega = N\omega_L$, with the harmonic order N and the laser frequency ω_L) which fulfills the Bragg condition and is observable under the angle θ satisfies the following equations according to [46] (see also section (2.3.5)):

$$n\,\omega\,a_x \sin\theta/c = 2\pi s_1 \tag{4.1}$$

$$a_z\,\omega\,(n_L - n\cos\theta)/c = 2\pi s_2\ , \tag{4.2}$$

where s_1 and s_2 are integers, $\lambda_L = 780\,\mathrm{nm}$ is the laser wavelength, a_x and a_z is the lattice period in laser polarization and propagation direction, respectively; n is the re-

fractive index of the harmonic wave and n_L the one of the laser wave. If $n_L << n$, i.e. if $n_L = n\cos\theta$ is possible in a crystal, the harmonic order N is observable under the angle $\theta = \arctan(s_1\lambda_L/(a_x n_L N))$. In the case that $n \approx n_L \approx 1$ (for simplicity $a = a_x = a_z$) the equations (4.1) and (4.2) yield (for $s_1 = s_2 = 1$) that the harmonic order N can be detected for $\theta = 90°$ if $N = \lambda_L/a$. This means that a periodic structure with nanometer spacing a is required. It is possible to implant various species of atoms into solids (doping) in a controlled way to build a crystal-like structure with nanometer spacings a [67]. As a result, the single atom signal can be efficiently enhanced by the number of lattice centers.

In our simulations presented in the next section the laser peak intensity reaches a value of $5 \cdot 10^{14}\,\frac{W}{cm^2}$. This can still be accomplished by relative compact laser systems. The static magnetic field does not exceed 30 T in our considerations. (Quasi)static magnetic fields of such magnitude are realizable in a laboratory without exorbitant circumstances. Generally, both static magnetic fields and pulsed magnetic fields whose duration ranges from μs to a few seconds should be taken into account. Pulsed fields of such long duration can be considered as static with regard to the fs durations of the laser-matter interaction. Superconducting magnets are able to produce static magnetic fields up to 15 T without problems. Those magnets should be able to be integrated into a setup used for HHG-experiments. Using Bitter plates static magnetic fields up to 33 T can be produced nowadays. The record field strength of 45 T for a static magnetic field has been generated by a combination of Bitter technology and superconducting coils. If Bitter technology is suitable for integration into HHG-experiments is not clear to us. However, pulsed magnetic fields reaching a value of 50 T can be produced in a laboratory without problems and might be compatible with common laser systems. For a survey of the magnet technology see [68] and references therein.

In the next section, the atomic quantum dynamics of a one-particle system in a weakly relativistic regime is studied. This concerns a parameter regime, in which the electron drift in the propagation direction becomes discernible. An interplay between this drift and the attraction of the nucleus results in a wiggly motion of the electron in the laser propagation direction. This motion gives rise to the radiation of high harmonics emitted into directions perpendicular to the laser propagation direction. In our simulations we can show that the signal strength of the harmonics can be substantially affected with the help of a static magnetic field which reaches a value of 30 T and is directed perpendicular to the plane spanned by the laser polarization and the laser propagation direction. Our considerations suggest a method that might be used to measure static magnetic fields.

4.2 Results: Impact of a static magnetic field on HHG-spectra

We solve the time-dependent Schrödinger equation numerically on a two-dimensional grid beyond the dipole approximation for a He^+ model ion subjected to a strong laser pulse and a static magnetic field. For a two-dimensional model atom in a laser field inducing weakly relativistic dynamics see [27,29]. The model system employed has been presented in detail in chapter (3). The laser pulse is linearly polarized along the x-axis and propagates in y-direction. The electron is initially bound to the ground state and localized at the origin (nucleus) of the x-y-plane. The Hamiltonian which rules the electron dynamics has been given by Eq. (3.9):

$$H(x,y,t) = \frac{1}{2}\mathbf{p}^2 + \frac{1}{c}A_x(y,t)p_x + \frac{1}{2c^2}A_x(y,t)^2 + V_{ion}(x,y) \tag{4.3}$$

Here t denotes the time and c the speed of light. The operator $\mathbf{p} = (p_x, p_y, 0)$ represents the canonical momentum. However, in contrast to the Hamiltonian (3.9), the non-vanishing component $A_x(y,t)$ of the vector potential $\mathbf{A} = (A_x(y,t), 0, 0)$ describes both the laser pulse of trapezoidal shape **and** the static magnetic field directed perpendicular to the x-y-plane. The part of $A_x(y,t)$ which models the static magnetic field has the simple form: $-B_{stat} \cdot y$, whereas B_{stat} denotes the static magnetic field component. The part of the vector potential which describes the laser pulse is given by Eq. (3.8). Thus, taking the curl of the entire vector potential $\mathbf{A}$ results in the sum the laser magnetic field (3.7) and the static magnetic field $\mathbf{B}_{stat} = B_{stat}\mathbf{e_z}$. Note, since we do not carry out the dipole approximation even the part of the vector potential that describes the laser pulse depends on the spatial coordinate y. Consequently, the laser magnetic field component does not vanish and causes a drift motion of the electron in the propagation direction [29]. Due to the arrangement of the fields the laser magnetic field and the static magnetic field compete with each other as both fields are directed perpendicular to the x-y-plane. We would like to emphasize that our simulations study a regime in which the drift motion becomes discernible but higher order relativistic effects can be safely neglected. $V_{ion}(x,y)$ describes the attraction of the nucleus and is modeled by a soft-core potential (see subsection (3.1.2):

$$V_{ion}(x,y) = -\frac{3.28}{\sqrt{1+x^2+y^2}} \tag{4.4}$$

The soft-core parameters in Eq.(4.4) have been chosen so that the electronic ground state wave function possesses an eigenenergy of -2 a.u. which corresponds to the real value. The ground state wave function has been obtained by propagation in imaginary time (3.4.2) and the spectral method (3.4.1). We employ the split-operator algorithm to solve the time-dependent Schrödinger equation with Hamiltonian (4.3), please see section (3.2).

Once the wave function is obtained the expectation value of position and the dipole acceleration can be computed. The center of mass motion of the electronic wave packet allows for association with classical dynamics. The dipole acceleration $\frac{d^2}{dt^2}\langle y\rangle(t)$ can be

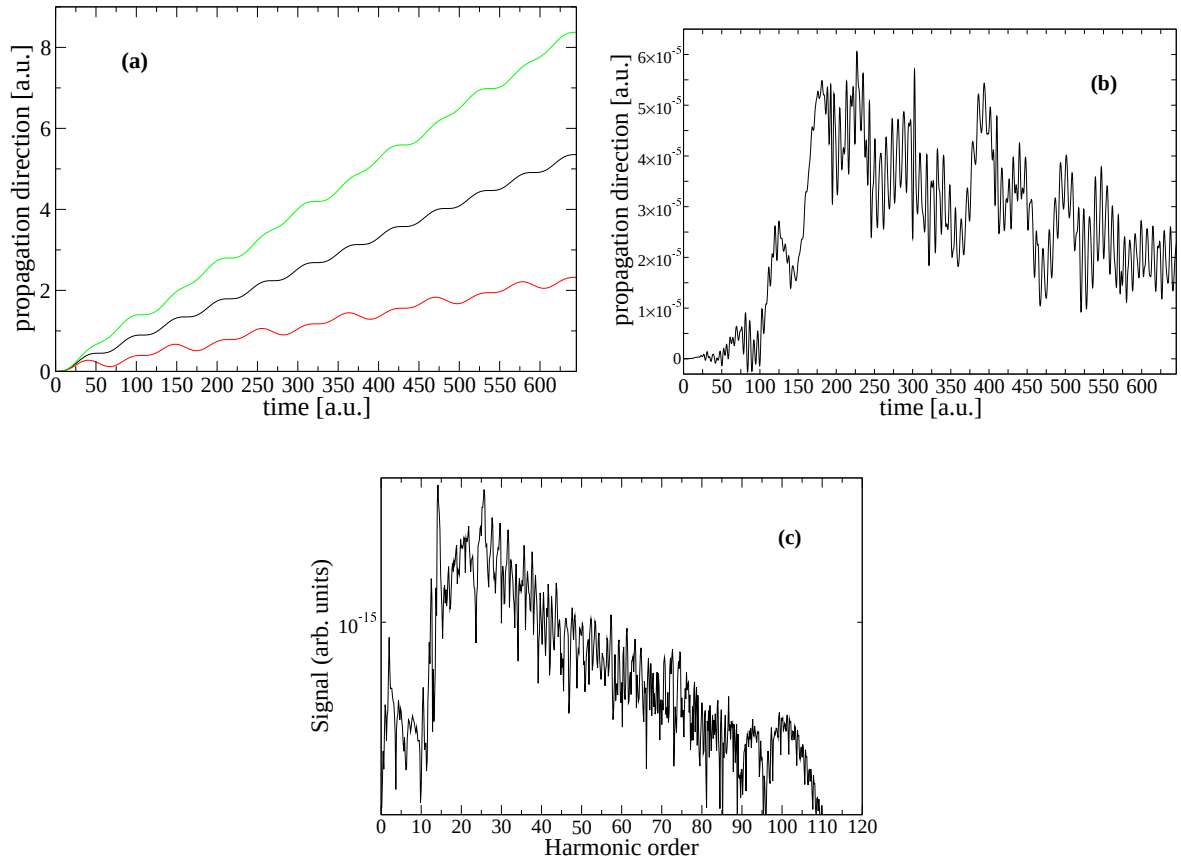

Figure 4.1: (a): Drift motion of a classical free electron subjected to a six-cycle cosine laser pulse (black curve). The electron was initially at rest. The red and the green curve show the trajectory of the classical electron if a static magnetic field of 30 T directed out of the x-y-plane and into it, respectively, is added to the laser pulse. (b): Wiggly electron motion along the laser propagation direction as a result of the interplay between the drift and the attraction of the nucleus. The electron is initially in the ground state of He^+ and is subjected to a 1-4-1-cycle trapezoidal laser pulse of 780 nm. The peak intensity of the pulse is $5.48 \cdot 10^{14} \frac{W}{cm^2}$. The expectation value of the electronic wave function is shown versus the time of interaction. (c): Harmonic spectrum arising from the electron motion in (b).

determined in different ways: On the one hand we have obtained it by building the second derivative of $\langle y \rangle(t)$ by means of a five-point formula. On the other hand, for comparison, we have computed the dipole acceleration via Ehrenfest's theorem (3.26). Hereby, we have only taken the force of the nucleus $-\langle \frac{\partial V_{ion}}{\partial y}(x,y) \rangle$ into consideration. Note, that there is no electric field component of the laser field in y-direction. To obtain the HHG-spectrum the dipole acceleration is multiplied by the Hanning window function and the modulus square of the Fourier transform of the windowed data is taken (see section (3.3)). A comparison of the spectra obtained by these different methods reveals that for the parameter regime presented here the spectra coincide quite well, apart from harmonic peaks of very low

order($< 10\omega_L$). This means that if one focuses on the higher harmonics, as usual, the magnetic field terms occurring as operators in Ehrenfest's theorem can be neglected [2].

Those terms only contribute to the lower harmonics. Note, that in spite of this, the magnetic fields are included in the Hamiltonian (4.3). Therefore they affect the wave function $\Psi(t)$ which results in an impact on the spectra even by employing Ehrenfest's theorem (simple version Eq. (3.26). Using numerical differentiation yields more noise in the spectra beyond the cut-off frequency than Ehrenfest's method does. However, for the parameter regime presented here, the noise beyond the cut-off remains two orders of magnitude beneath the signal strengths of the harmonics in the cut-off region. Therefore, we have decided to present here those spectra which are based on numerical differentiation.

It is well known that a classical free electron which is subjected to a linearly polarized laser field whose magnetic field component becomes important in a weakly or full relativistic regime follows a typical zig-zag trajectory (see section (2.1)). This is attributed to the fact that the electron oscillates along the polarization direction while it performs a drift in the propagation direction. For illustration, Fig. 4.1(a) (black line) shows this drift motion versus the interaction time for a classical free electron which is subjected, for simplicity, to a six-cycle cosine laser pulse. Initially, the electron was at rest. This drift in the propagation direction is a monotonous function of time if the electron is initially at rest.

Fig. 4.1(b) now depicts a result of our quantum simulations: the drift motion of the center of mass of the electronic wave packet that has been initially bound to the ground state is shown. The electron interacts with a 1-4-1-cycle trapezoidal laser pulse of 15.6 fs duration. The wavelength of the irradiated laser beam is 780 nm and its peak intensity has a value of $5.48 \cdot 10^{14} \frac{W}{cm^2}$. We have chosen this intensity with the idea in mind that on the one hand the laser field should be strong enough to obtain a discernible electron motion in propagation direction but on the other hand it should not be too strong so that a static magnetic field of 30 T is still able to compete with the laser peak magnetic field component having 214 T for this laser intensity. In contrast to a free electron subjected to a laser pulse, there is, in addition to the drift motion, the attraction of the nucleus. In Fig. 4.1(b) one can still recognize the drift motion which is characterized by a an oscillatory motion of large period. However, rapid oscillations that can be attributed to the presence of the nucleus are superimposed to the drift motion. The interplay between the drift and the attraction of the nucleus results in a wiggly motion in propagation direction. Due to the presence of highly nonlinear acceleration, this gives rise to HHG-radiation. Note, that this sort of radiation is emitted in directions

[2] In order to perform the computation of $\frac{d^2}{dt^2}\langle y\rangle(t)$ completely one would apply a generalized Ehrenfest's theorem, in which the magnetic fields (laser and static magnetic field) would appear explicitly as operators:

$$\frac{d^2}{dt^2}\langle y\rangle(t) = -\langle\frac{\partial V_{ion}}{\partial y}\rangle - \frac{1}{2c}\langle(\mathbf{v}\times\mathbf{B} - \mathbf{B}\times\mathbf{v})_y\rangle \tag{4.5}$$

$\mathbf{v}$ denotes the kinematic velocity operator and $\mathbf{B}$ the magnetic field consisting of laser and static magnetic field. Formula (4.5) is based on the notes in [71].

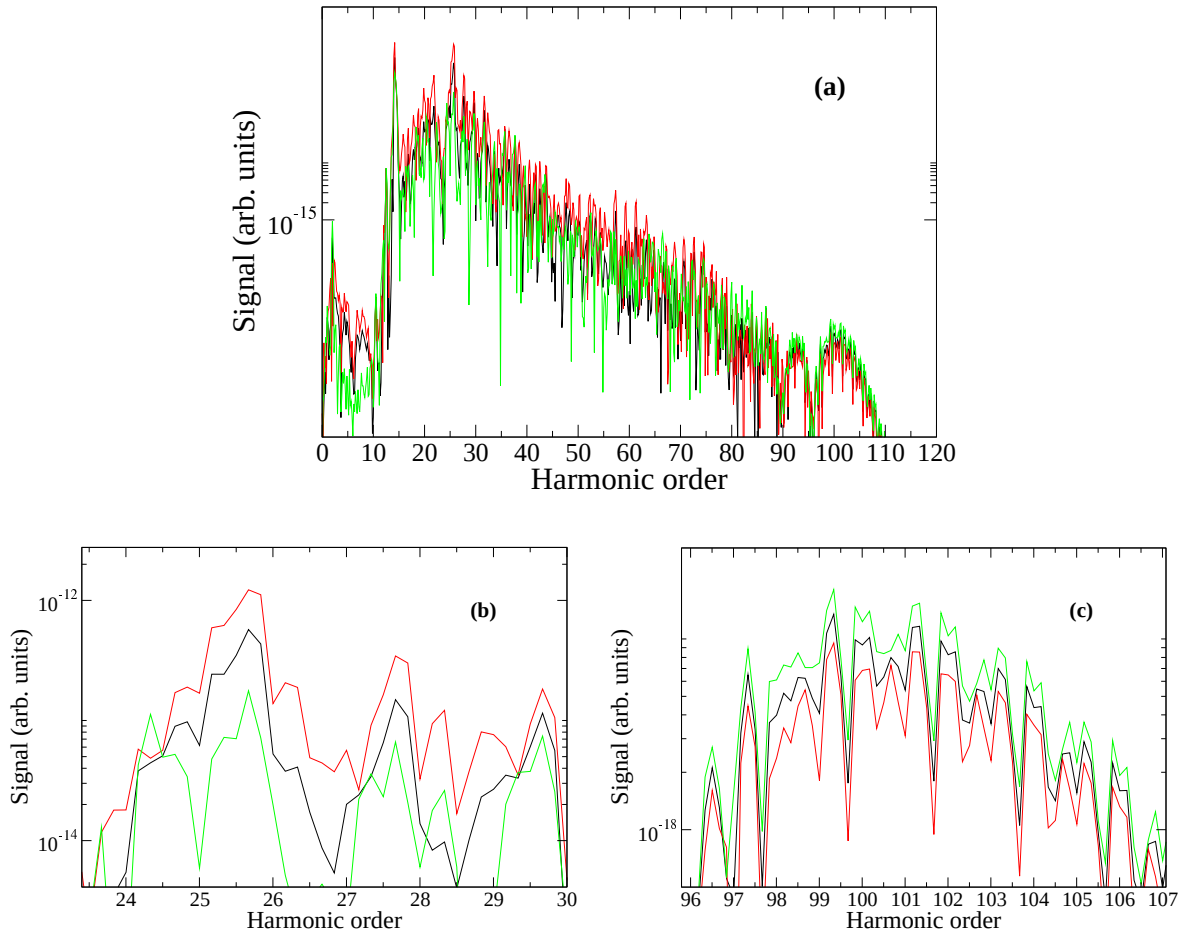

Figure 4.2: (a): Impact of a static magnetic field on the HHG-spectrum shown in Fig. 4.1(c). The black line represents the HHG- spectrum in the case of vanishing static magnetic field, whereas the red and the green line display the spectrum which occurs in the presence of a 30 T magnetic field pointing out of the x-y-plane and into it, respectively. The orientation of the static magnetic field turns out to be crucial.
(b): depicts a cut-out of (a) focusing on the range of frequencies around $25.7\omega_L$, whereas ω_L denotes the laser angular frequency.
(c): takes a closer look at the cut-off region of the HHG spectrum in (a).

perpendicular to the propagation direction. In a non-relativistic approach this radiation is polarized in propagation direction, see (10.7) in [36]. We confine ourselves to take the Fourier transform of the dipole acceleration in propagation direction belonging to the wiggly motion in this direction. We mention that already according to a semi-classical concept [69] the influence of the nucleus becomes relevant: A recolliding electron senses the attraction of the nucleus exactly at that moment, in which it passes the nucleus. This influence of the nucleus affects the motion in propagation direction and gives rise to HHG-radiation. An HHG-spectrum based on the electron motion in propagation direction has been presented in simulations in a quantum mechanical approach, too [65].

Fig. 4.1(c) displays the HHG-spectrum belonging to the wiggly electron motion in Fig. 4.1(b). The spectrum consists of a variety of peaks which are not always placed at integer numbers of harmonic order. This might be attributed to the relatively short pulse duration of six laser cycles [70]. In contrast to the normally considered HHG-spectrum that arises due to the electron motion in polarization direction this spectrum possesses an intensity in harmonic strength which is about six orders of magnitude lower.

By adding a static magnetic field which is directed perpendicular to the x-y-plane it is possible to affect the spectrum shown in Fig. 4.1(c). This is illustrated in Fig. 4.2(a). Here, we see the influence of a 30 T magnetic field whose orientation plays a significant role: The black line represents the spectrum in the case that the static magnetic field vanishes. The red line illustrates a spectrum which is generated in the presence of a 30 T magnetic field pointing out of the x-y-plane. The case of a static magnetic field of 30 T directed in the opposite direction is depicted by the green line. Note, that for all pictures shown below an analogous assignment of the colors is valid. Depending on the orientation of the static magnetic field the harmonic peaks experience an increase and a decrease, respectively. The harmonic peaks in the front and the middle part of the spectrum, beginning with a frequency of $10\omega_L$, are mainly reinforced by a 30 T magnetic field pointing out of the x-y-plane; ω_L denotes the laser angular frequency. The opposite orientation of the magnetic field mainly leads to a decrease of the harmonic signals in this frequency range. For the frequency range just below the cut-off the situation is vice versa. Here, a magnetic field pointing into the x-y-plane is more advantageous for the generation of harmonics. A shifting of the cut-off frequency is not observed. There are no major changes induced by the static magnetic field concerning the shape and the position of the harmonic peaks.

We now study the changes in harmonic intensity in more detail and have a closer look at two salient peaks: Fig. 4.2(b) shows a cut-out of Fig. 4.2(a) around the peak situated at a frequency of $25.7\omega_L$. The peak placed at this frequency experiences an enhancement by a factor of 2.1 and a decrease by a factor of 0.3, respectively, depending on the parallel and anti-parallel alignment of the static magnetic field, respectively (red and green line, respectively).

The increase of the harmonic signal by a factor of 1.3 at the peak placed at a frequency of $99.3\omega_L$ is illustrated in Fig. 4.2(c). Here, the static magnetic field points into the x-y-plane. The decrease by a factor of 0.7 at the same peak is achieved by the opposite alignment of the magnetic field. Here, however, the changes in the signal strengths are not so distinct any more than at the peak situated at $25.7\omega_L$ (Fig. 4.2(b)).

In order to make the impact of the static magnetic field on the spectrum (Figs. 4.2 (a),(b),(c)) plausible we consider the changes the static magnetic field causes with regard to the center of mass trajectory of the electronic wave packet (Fig. 4.3) and the dipole acceleration (Figs. 4 (a),(b),(c)). In Fig. 4.3 we find both an increase and a decrease of the amplitude of the motion in propagation direction. Apart from the very beginning, the temporal pattern of oscillations in this direction is hardly affected. Classically, the Lorentz drift in propagation direction is changed in the presence of a static magnetic field as illustrated in Fig. 4.1(a) (red and green lines). From this classical consideration we

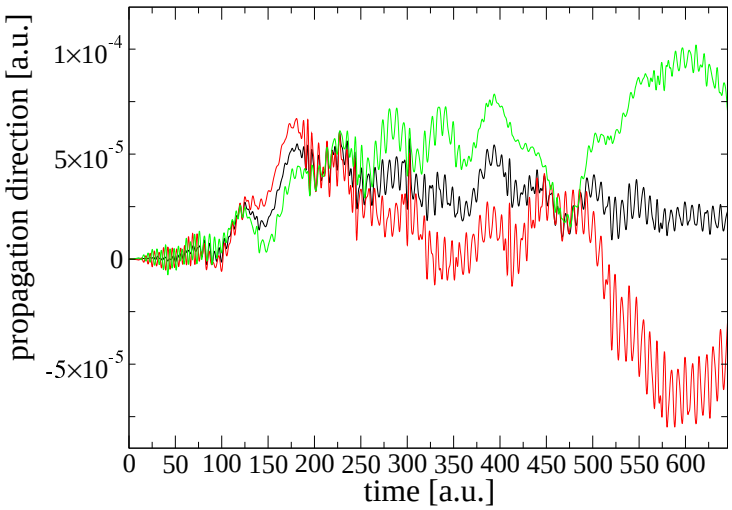

Figure 4.3: Center of mass motion of the electronic wave packet in the presence of an additional static magnetic field. The black line represents the electron motion for vanishing static magnetic field, as already depicted in Fig. 1 (b). The red and green curve show the cases, in which a static magnetic field of 30 T is added pointing out of the x-y-plane and into it, respectively.

see that the classical free electron experiences an additional spatial shift of the order of magnitude of a few atomic units since the static magnetic field induces a supplementary Lorentz force acting on the electron most effectively in laser propagation direction.

The same is true an electron wave packet ejected into the continuum during the ionization process. This means that ejected wave packets sense a Lorentz drift which is modified by the static magnetic field. Depending on the velocity of the wave packets and the orientation of the static magnetic field the wave packets are spatially shifted in laser propagation direction due to the Lorentz drift induced by the static magnetic field. Additionally, brought to a different position the wave packets also sense a slightly different phase of the laser field leading to an altered wave packet dynamics. The modified wave packet dynamics is responsible for the increased or decreased amplitudes in the center-of-mass motion $\langle y \rangle(t)$ of the electronic wave packet. The large amplitudes of the center of mass trajectory of the electronic wave packet occurring at the end of the laser interaction in the case of a static magnetic field (see Fig. 3, last laser cycle beginning at 538 a.u.) can be attributed to the fact that the static magnetic field becomes more influential compared to the laser magnetic field as the laser field is turned off during the last optical cycle.

The additional spatial shifting of ionized wave packets in laser propagation direction which is induced by the static magnetic field also changes the overlap between returning wave packets and the ground state wave function. This is illustrated in Fig. (4.4). Depending on whether this overlap is increased or decreased the recombination process of HHG is made more effective or less effective resulting in an enhanced or diminished HHG photon emission (see Fig.4.4), i.e: Different ionized and recolliding wave packets belong to different frequencies in the harmonic spectrum (for example the frequencies 25.7 ω_L

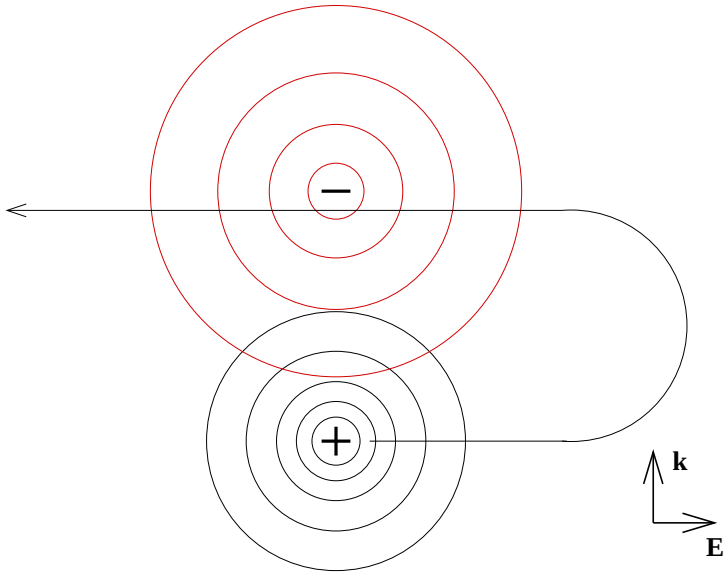

Figure 4.4: Schematic diagram of the recollision process affected by the static magnetic field. Shown is the overlap between the recolliding wave packet (red) and the initial state (black) at the position of the nucleus (indicated by +). The overlap is increased or decreased by the displacement of the recolliding wave packet in the laser propagation direction (**k**-direction), **E** indicates the laser polarization direction. The displacement induced by the laser magnetic field is changed by the static magnetic field. As a consequence, the static magnetic field alters the intensity of the harmonic radiation polarized in the laser propagation direction.

and 99.3 ω_L) according to the recollision model of high harmonic generation. These wave packets follow different trajectories in the combined laser and static magnetic field until the recollision of the wave packet at the site of the nucleus and subsequent recombination into the ground state takes place by emitting a photon of appropriate frequency. Owing to different trajectories the wave packets experience a different shift in the laser propagation direction. This shift results from the Lorentz force which is additionally induced by the static magnetic field. Thus, this shift depends on the specific trajectory (depending again on the harmonic frequency) and on the strength and the orientation of the static magnetic field. This implies that at the recollision event the overlap of the recolliding wave packet with the ground state depends both on the specific trajectory of the recolliding wave packet and on the strength and the orientation of the static magnetic field. Therefore, it becomes clear that for the same orientation of the static magnetic field certain harmonics are enhanced while others may be diminished in intensity. If the orientation of the static magnetic field is changed the overlap of the recolliding wave packet with the atomic ground state is increased or decreased so that one finds a contrary situation: The harmonics which have been enhanced are weakened if the orientation of the static magnetic field is tilted. The harmonics which have been weakened are increased in intensity if the orientation of the static magnetic field is inverted. These effects are also reflected in the dipole acceleration. At the time of recollision, an oscillation in the dipole acceleration occurs

with a frequency at which a harmonic peak in the spectrum is situated. The amplitude of the oscillation depends on the overlap of the recolliding wave packet with the ground state. Therefore, we now consider the dipole acceleration and the impact on it induced by the static magnetic field due to the modified recollision process in the laser propagation direction. The corresponding parts of the dipole acceleration which are responsible for the frequencies 25.7 ω_L and 99.3 ω_L can be found by means of a Morlet wavelet analysis of the dipole acceleration [64]:
A Morlet wavelet analysis provides a time-frequency analysis of a temporal signal, i.e., it gives an answer to the question at which time in the course of the signal a specific frequency occurs. The question which frequencies are contained in a temporal signal at all is answered by Fourier transformation. A Morlet wavelet transform provides information about *when* a certain frequency occurs in the signal.

In our situation the time-dependent dipole acceleration in the laser propagation direction $a_y(t)$ represents the temporal signal of interest. The harmonic spectrum pertaining to this dipole acceleration depicts the spectral range which this temporal signal contains at all. The question *when* a certain harmonic is emitted can thus be answered by the Morlet wavelet transform of the dipole acceleration:

$$S(t,\omega) = \frac{\sqrt{\omega}}{\sqrt{\tau}} \int dt' e^{i\omega(t'-t)} e^{-\frac{\omega^2(t'-t)^2}{2\tau^2}} a_y(t'). \tag{4.6}$$

The quantity $|S(t,\omega)|^2$ indicates for which time t the frequency ω is contained in the signal $a_y(t)$. Formula (4.6) means that for a given time t a Gaussian window is applied to the signal $a_y(t')$. For this windowed signal the spectral information is determined via subsequent Fourier transformation. The parameter τ helps to decide whether the Morlet transform is sensitive to time or to frequency. A narrow Gausssian results in a better resolution with respect to time but in a worse with regard to frequency. For our purpose, τ=10 has turned out to be appropriate. For a fixed frequency ω the quantity $|S(t,\omega)|^2$ represents the time-profile of the signal $a_y(t)$ for the harmonic with frequency ω. The peaks in the time-profile indicate the times when the harmonic frequency ω is emitted.

Fig. 4.5(a) illustrates the dipole acceleration versus time during the interaction of the electron with the laser pulse in all three cases of magnetic field orientation (black, red and green lines). One recognizes that the amplitude of the dipole acceleration is increased or decreased by the static magnetic field. Furthermore, the temporal pattern of the dipole acceleration remains essentially unaltered. Mainly at the beginning, when the influence of the laser field is still weak a relative shifting of the dipole accelerations takes place. The observations made above are corroborated by a Morlet wavelet analysis [64]. Moreover, this wavelet analysis made the following considerations possible: The blue and the pink line show the scaled time profiles of the harmonic peaks at frequencies of $25.7\omega_L$ and $99.3\omega_L$, respectively. For clarity, only the time profiles for these frequencies in the case of a vanishing static magnetic field are depicted. The blue line marks the time intervals that the radiation with frequencies around $25.7\omega_L$ is emitted in. At these times the configuration, in which the static magnetic field points out of the x-y-plane, yields the largest amplitudes of the dipole acceleration. The pink line indicates the time interval that the fastest oscillations happen in. Essentially there, the harmonics around the peak placed

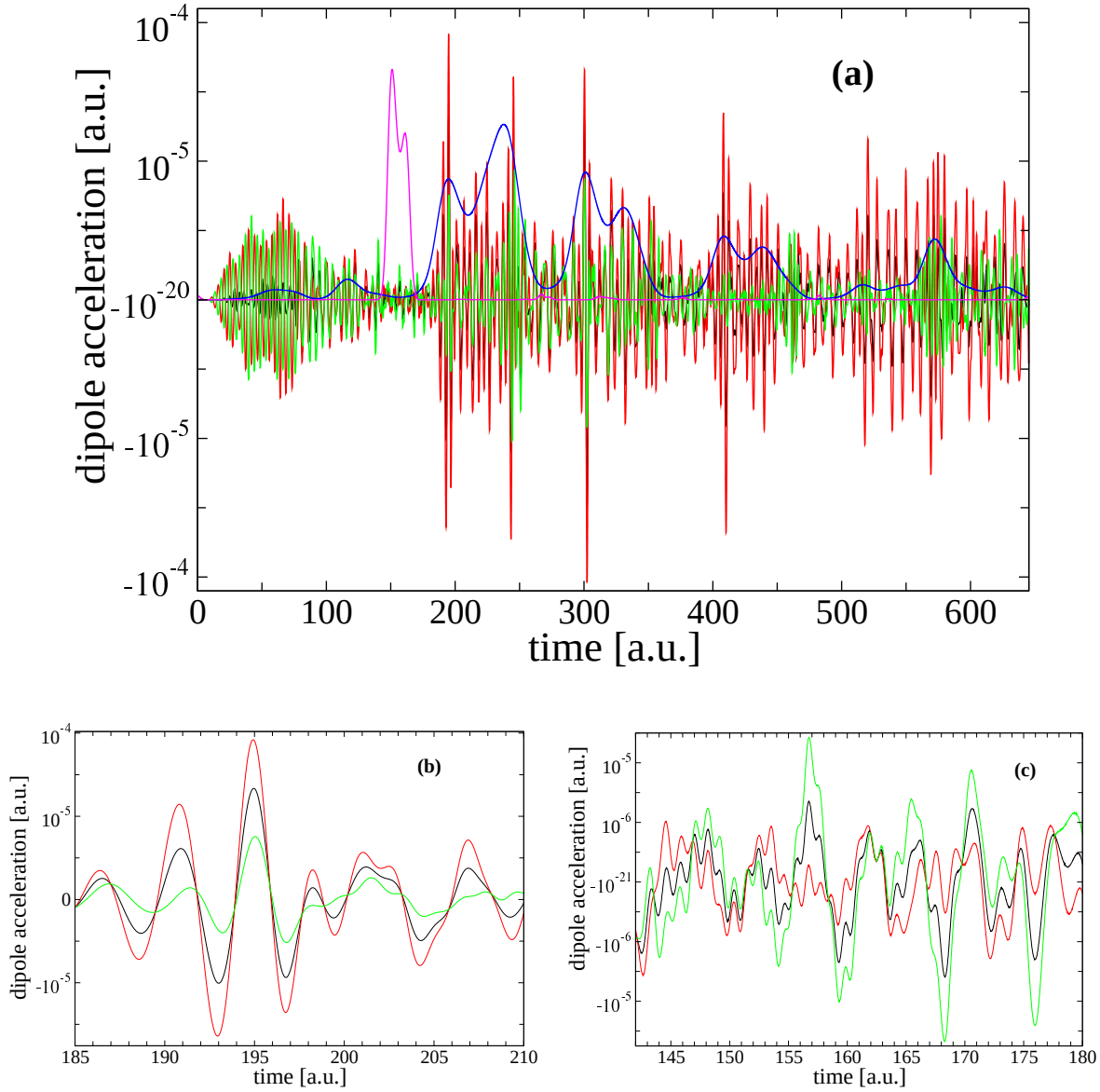

Figure 4.5: (a): Dipole acceleration and time profiles. The black, red and green line represent the dipole acceleration during the interaction with the laser pulse: black: no static magnetic field, red: static magnetic field of 30 T pointing out of the x-y-plane, green: static magnetic field of 30 T directed into the x-y-plane. These dipole accelerations belong to the wiggly center of mass motion of the electronic wave packet depicted in Fig. 4.3. The blue and the pink curve represent the scaled time profiles of the frequency ranges centered at $25.7\omega_L$ and $99.3\omega_L$, respectively. For clarity, only the time profiles in the case of vanishing static magnetic field are depicted. The peaks of the time profiles indicate the times when radiation of the corresponding frequency range is emitted.
(b): Cut-out of (a) focusing on the dipole acceleration in the time interval at 195 a.u..
(c): Cut-out of (a) for the dipole accelerations in the time interval at 160 a.u..

at $99.3\omega_L$ in the cut-off region are generated. As to this time interval the amplitudes of the dipole acceleration have the largest values if the static magnetic field points into the x-y-plane (green line).

In order to illustrate the relations explained above we have a closer look at two time intervals: those at time 160 a.u. and 195 a.u..

Fig. 4.5(b) depicts a time interval around 195 a.u., which frequency components around a frequency of $25.7\omega_L$ are emitted in. It is evident that a static magnetic field pointing out of the x-y-plane enhances the amplitude of the oscillation of the dipole acceleration while the opposite orientation of the magnetic field results in a decrease of the amplitudes. The same is true for the other frequency intervals which this frequency range is emitted in. Thus, it is clear that the HHG-peaks placed around a frequency of $25.7\omega_L$ are increased by a static magnetic field which is directed out of the x-y-plane. Correspondingly, these peaks are diminished in strength by the opposite magnetic field orientation.

Fig. 4.5(c) shows the time interval in which the main contribution to the radiation of frequencies around the $99.3\omega_L$ peak in the cut-off region is generated. Here, we have the contrary situation. As one can recognize the amplitude of acceleration is enhanced by a static magnetic field which points into the x-y-plane. Correspondingly, we recognize a decrease of the amplitude for the opposite alignment of the static magnetic field. Hence, it becomes apparent that the peaks in this region of the HHG-spectrum are correspondingly reinforced or weakened by the static magnetic field.

By means of a Morlet wavelet analysis the behavior of the dipole acceleration with regard to the static magnetic field orientation, as depicted above, can be confirmed by computing the integral over each time-profile that belongs to the corresponding harmonic frequency ($25.7\omega_L$ or $99.3\omega_L$).

Now we focus on the question how the signal of a certain harmonic varies with the strength of the static magnetic field, i.e. to employ our scheme as a device to measure strong static magnetic fields. Therefore, we have performed simulations in which the value of the static magnetic field is modified gradually from -30 T up to 30 T. A negative sign is to signify that the magnetic field points into the x-y-plane, whereas a positive one indicates that the magnetic field is directed out of this plane. We have observed no change of the temporal pattern of trajectories $\langle y \rangle(t)$, the dipole accelerations and the HHG-spectra on principle. Merely, the amplitudes and signal strengths modify gradually if the magnetic field is changed. For illustration, Figs. 4.6(a),(b) show the dependence of harmonic peaks placed at $25.7\omega_L$ and $99.3\omega_L$ on the magnetic field strength. As expected, the signal strengths seem to lie on a smooth curve, for the static magnetic field changes smoothly the amplitudes of $\langle y \rangle(t)$ and thereby the curvature as well. In certain regions of weaker magnetic fields (from -5 T up to 5 T) there seems to exist a linear dependence. This might be employed in order to measure the strengths of magnetic fields. Having this purpose in mind the signal of a certain harmonic should be measured. By means of the dependence depicted above the actually present magnetic field can be determined.

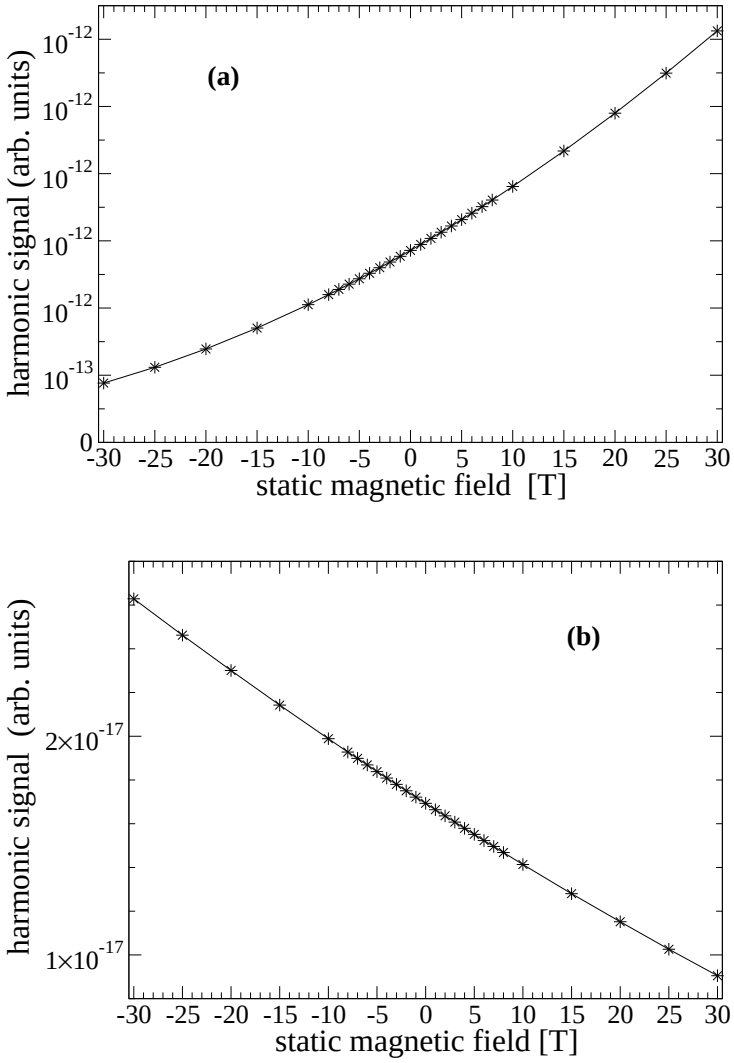

Figure 4.6: Dependence of the harmonic signal on the strength of the applied static magnetic field:
(a) for the harmonic signal at a frequency of $25.7\omega_L$.
(b) for the harmonic signal at a frequency of $99.3\omega_L$.

Chapter 5

Results II: Antisymmetry and magnetic-field effects

In the field of high-intensity laser-matter interactions the recollision dynamics of electrons ejected by a strong laser pulse is the basis of various strong-field phenomena like high-order harmonic generation (HHG) [74], nonsequential double ionization [75] and above-threshold [76] ionization. For instance, high-order harmonic generation in molecules is of particular interest in both theoretical and experimental studies at present. In recent investigations it has been shown that high-order harmonic radiation serves as a means to reconstruct molecular orbitals from HHG-spectra [77]. Whereas for both *atoms* and *molecules* a three-step mechanism is responsible for HHG (see section 2.3), additional signatures in HHG-spectra of molecules are found which permit to draw conclusions about the separation of the nuclei (see section 2.3.4) and even about their vibrational motion. Additionally, the anisotropy of molecular orbitals is reflected in the dependence of the corresponding HHG-spectra on the orientation of the orbital to the laser polarization direction [45, 78]. As discussed in detail in section (2.3), the underlying three-step process consists first in the ejection of an electron as an atom or a molecule is subject to a strong laser pulse. This is accomplished by electron tunneling through the potential barrier tilted by the laser field. In the second step the tunneled electron performs a quasi free oscillatory motion in the laser field. When the laser field changes its sign the electron wave packet is driven back to the nucleus. In the third step which represents the recollision event the wave packet recombines at the positions of the nuclei into the initial state under emission of high-harmonic radiation. Considering this last step, it becomes plausible that the additional molecular degrees of freedom as vibration of the nuclei and the anisotropy of molecular orbitals may sensitively affect this recombination process. Therefore, signatures of molecular structure can be found in HHG-spectra. We would like to emphasize that the investigation of orientation-dependent characteristics in HHG-spectra and their relation to molecular symmetry opens up an interesting field of research [79]. This is particularly interesting in terms of the alignment techniques [80] which allow to bring a molecule in the desired orientation with regard to the polarization direction of a strong laser field. In this chapter we will propose a novel mechanism by showing that the peculiarities of the momentum distribution of antisymmetric molecular and atomic orbitals,

which give rise to a lateral drift of electrons ejected by the laser field, can be employed to efficiently compensate for the electron drift induced by the laser magnetic field of a very intense laser field [72, 73]. As a result, there is an enhancement of recollisions. From a different point of view on this mechanism, it is shown that the electron drift induced by the laser magnetic field which has been considered as rather detrimental to the recollision dynamics as yet (see section (2.3.1)) gives rise to enhanced recollisions and with this leads to an increased harmonic emission.

However, if one focuses on the generation of extreme short-wavelength harmonic radiation and if one therefore subjects molecules to very intense fields, one faces the problem that molecules whose outermost electrons are weakly bound are substantially ionized already during the turn-on phase of the laser pulse, i.e., the laser interaction with the molecules takes place in the over-the-barrier ionization (OTBI) regime. As a result, the common 3.17-cut-off rule is not obeyed for weakly bound molecular systems as the results for H_2^+ in section (5.2) demonstrate. Facing this problem of rapid ionization it is advantageous to use antisymmetric *atomic* ions that withstand very intense laser fields. This permits an efficient recollision dynamics and with this the generation of extreme short-wavelength high-order harmonic radiation, i. e. these antisymmetric atomic systems comply with the 3.17-cut-off rule and allow of higher harmonic signals in comparison with H_2^+.

Thus, this chapter is structured as follows: In section 5.1 we explain in detail the underlying physical mechanism and the basic concept, i.e. the electron drift induced by the laser magnetic field, the properties of wave functions with mirror antisymmetry with respect to a nodal line and the combination of both in order to enhance recollisions and the harmonic signal. The results for H_2^+ are presented in section (5.2). Section (5.3) is dedicated to the results for hydrogen-like *atomic* ions. Concluding this chapter with section (5.4) novel effects with respect to two-center interference structures are presented as an outlook for future work in this field.

5.1 Basic concept

In this section we apply the concept of harnessing the properties of antisymmetric wave functions in order to compensate for the electron drift induced by the laser magnetic field. This concept is applied to H_2^+ and to atomic ions. As for the latter, we consider excited eigenstates of hydrogen-like ions with antisymmetry with regard to a nodal line. These states have a similar shape as the antisymmetric wave function of the first electronically excited state of H_2^+ and they therefore possess the same properties of the momentum wave functions. We make use of them to compensate for the electron drift induced by the laser magnetic field. We obtain our results by numerical integration of the time-dependent Schrödinger equation on a 2D grid with and without employing the dipole approximation for very intense laser fields, respectively (see chapter (3)). Our model states in the atomic case are equivalent to real $2p$-atomic wave functions. The results for H_2^+ show the success of our method by the enhancement of high-order harmonic generation as an important

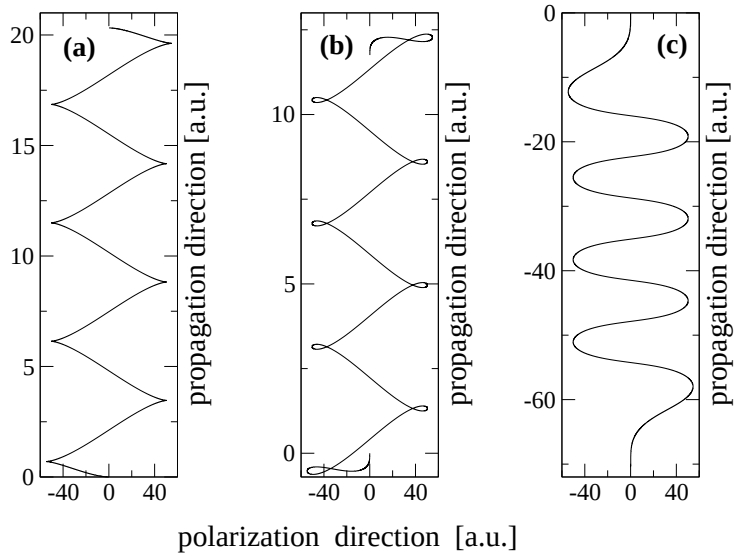

Figure 5.1: (a): Typical zig-zag motion of a classical electron subject to the trapezoidal laser pulse of an intensity $I = 1.4 \cdot 10^{17}\,\mathrm{W/cm^2}$ employed in the following quantum calculations. The electron has been initially at rest. The drift in the laser propagation direction which is induced by the magnetic component of the laser field becomes more important for stronger fields.
(b): The drift in the laser propagation direction is reduced by choosing appropriate initial conditions. In this figure the initial momentum in the laser propagation direction takes a value of -0.05 a.u. causing the electron to launch in the negative laser propagation direction. According to the momentum distribution due to antisymmetry in Fig.5.3 there is a small but appreciable likelihood for this initial momentum.
(c): The drift in the laser propagation direction is over-compensated by the choice of an initial momentum of -0.53 a.u., for which there is the largest likelihood according to Fig.5.3.

recollision-related process. But in the wake of the interplay of antisymmetry and the drift induced by the laser magnetic field new effects concerning two-center interference structures in HHG-spectra are found (see section (5.4)).

For illustration, Fig. 5.1(a) shows the drift motion in the laser propagation direction of a free electron subject to an intense laser pulse whose magnetic field component is responsible for this drift (see section (2.1)). The electron is initially at rest at the origin. If one is interested in the reduction of this drift in the laser propagation direction one can choose appropriate initial conditions, i.e. with an initial velocity directed in the negative laser propagation direction. In Fig. 5.1(b) the initial velocity in the laser propagation direction is -0.05 a.u. As a result, the drift in laser propagation direction can be reduced. Fig. 5.1(c) shows an over-compensation for the laser-induced drift due to an initial velocity of -0.53 a.u. which is the most probable initial velocity (momentum) in the laser propagation direction for the lowest antisymmetric state of H_2^+ according to Fig. 5.3. This classical

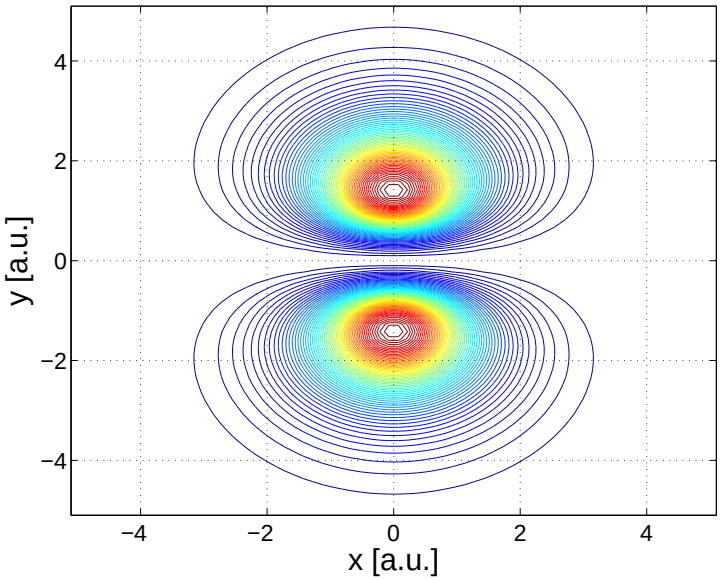

Figure 5.2: Density of the first excited antisymmetric state of a 2D H_2^+ molecule. The nuclei are at positions $(0, 1)$ and $(0, -1)$ modelled by soft-core potentials (Eq.(3.11)). The salient feature is the nodal line parallel to the $y = 0$-axis. Note that also the density of the first excited antisymmetric eigenstate of a hydrogen-like ion modelled by a single soft-core potential Eq.(3.10) has a similar shape.

picture suggests a method to compensate for the drift induced by the laser magnetic field. In the following quantum-mechanical considerations, however, the drift counteracting the laser-induced one is provided by antisymmetry. It is known for some time that this drift, which is induced by the laser magnetic field, is also relevant for electron wave packets ejected from an atom in a strong laser field. This process gives rise to a shift of the electron wave packet in the laser propagation direction. As discussed in the context of the three-step model of HHG, this implies for the generation of high-order harmonics that the overlap of recolliding wave packets with the initial wave function is reduced, which results in a decrease in the harmonic signal as a consequence of the laser magnetic field. Obviously, this detrimental influence of the laser magnetic field is not only relevant for HHG but also for other recollison-related effects like nonsequential double ionization and high-order above threshold ionization. We point out in this section that the magnetic-field drift can be compensated by another drift which originates from the essence of antisymmetric wave functions. From a different viewpoint on the same mechanism, it becomes evident that the magnetically induced drift is able to increase recollisions and therefore can significantly support harmonic generation.

The properties of the momentum distribution of antisymmetric wave functions are in the focus of the following considerations. They are employed to affect the magnetically induced electron drift. Fig. 5.2 shows the density of the first excited state of a 2D H_2^+ molecule. The density of the corresponding momentum wave function is shown in Fig.

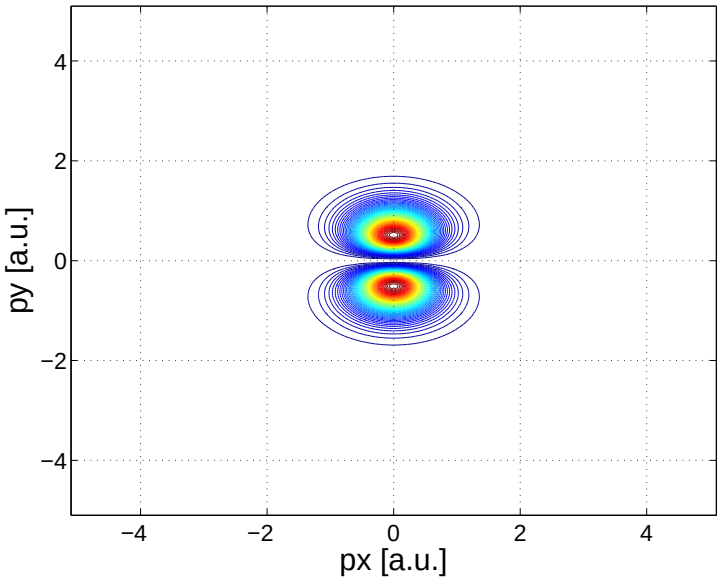

Figure 5.3: Density of the momentum wave function belonging to the wave function in position space depicted in Fig. 5.2. It is obtained as the modulus square of the Fourier transform of the wave function in Fig. 5.2. The anisotropy of this momentum distribution is responsible for the drift exhibited by electrons after field-assisted ejection: The figure illustrates clearly that the initial momentum of the electron is preferably directed in y-direction. The nodal line in this momentum distribution is responsible for the circumstance that there is no likelihood of momentum vectors directed strictly parallel to the x-axis. This means that no electrons are ejected strictly parallel to the x-axis during the interaction with the laser field.

5.3. This density illustrates the momentum distribution of the momenta p_x and p_y with regard to the x-axis and the y-axis, respectively. It is the modulus square of the Fourier transform of the wave function in coordinate representation shown in Fig. 5.2. The orientation of the nodal line ($p_x = 0$) is retained in the momentum distribution. Crucially, it is discernible that the probability for momentum vectors (p_x, p_y) which are oriented strictly parallel to the p_x-axis, i.e., with no p_y-component, vanishes. This means that, if one considers such a wave function subject to a strong laser field as a reservoir of electrons, the ejected electrons have an initial drift perpendicular to the nodal line. This lateral drift which is due to the antisymmetry of the wave function affects sensitively all recollision-related effects, i.e., in particular HHG. If one considers a scenario in which an antisymmetric wave function as shown in Fig. 5.2 is subject to an intense linearly polarized laser field with polarization direction being the x-axis and the propagation direction being the y-axis, the recollision of ejected electrons and correspondingly HHG is suppressed. The tunneled electron is driven along the x-axis by the laser field. However, the electron has an initial drift in y-direction owing to the momentum distribution. Due to this drift the electron has been shifted in the positive or the negative y-direction, respectively, when the electron is accelerated back towards the nucleus again. From a classical point of view a recollision is precluded. However, also in a quantum picture, in

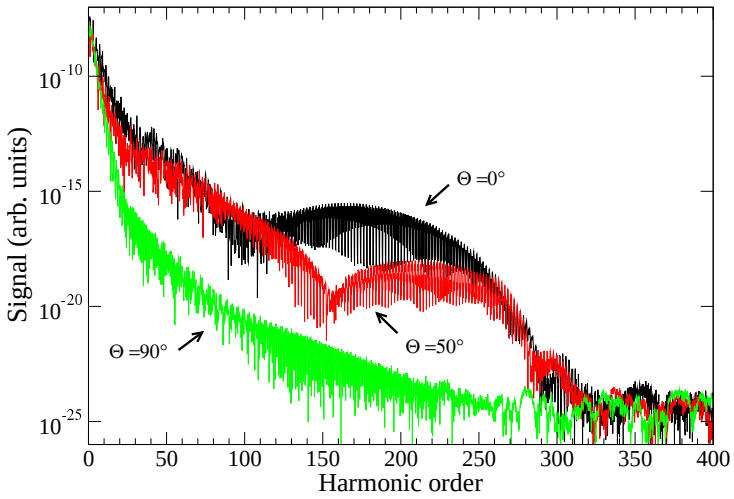

Figure 5.4: The drift due to antisymmetry impedes an efficient harmonic generation. These simulations have been obtained in the dipole approximation, i.e. there is no electron drift in the laser propagation direction owing to the laser magnetic field. The initial wave function is the first excited antisymmetric state of 2D H_2^+. The angle Θ denotes the angle between the laser polarization direction and the molecular axis (which is perpendicular to the nodal line). The laser pulse consists of one cycle linear turn-on phase, four cycles of constant intensity and one cycle linear turn-off. The laser peak intensity is $1.4 \cdot 10^{17}\,\mathrm{W/cm^2}$. The laser wavelength is 248 nm. For $\Theta = 0°$ (black line) the drift due to antisymmetry is directed along the laser polarization direction and therefore it does not hamper HHG. Increasing Θ results in a stronger impediment of HHG because the drift induced by antisymmetry becomes important. Therefore, the harmonic signal for $\Theta = 50°$ (red line) is lowered in comparison with the $\Theta = 0°$-spectrum. The lowest harmonic signal is obtained for $\Theta = 90°$ (green line), since in this constellation the drift due to antisymmetry takes most effect on the recollision dynamics.

which the wave packet spreading in y-direction has to be taken into account, an efficient recollision process is prevented. Keeping the x-axis as the laser polarization direction and the y-axis as the laser propagation direction and rotating the antisymmetric initial wave function by 90°, so that the nodal line is finally parallel to the y-axis, results in an initial drift of ejected electrons along the laser polarization direction. However, the laser electric field prevails in this direction. As a result, the drift induced by the antisymmetry of the wave function plays a minor role and HHG remains unaffected. The explanations above suggest that HHG is hampered the more parallel the nodal line is oriented to the laser polarization direction. These considerations are only valid in the dipole approximation. Simulations performed in the dipole approximation confirm the detrimental impact of the drift induced by antisymmetry on high-order harmonic generation, as Fig. 5.4 illustrates. The more the nodal line of the first excited antisymmetric state is aligned along the laser polarization direction the more the drift due to antisymmetry can reduce the harmonic signal.

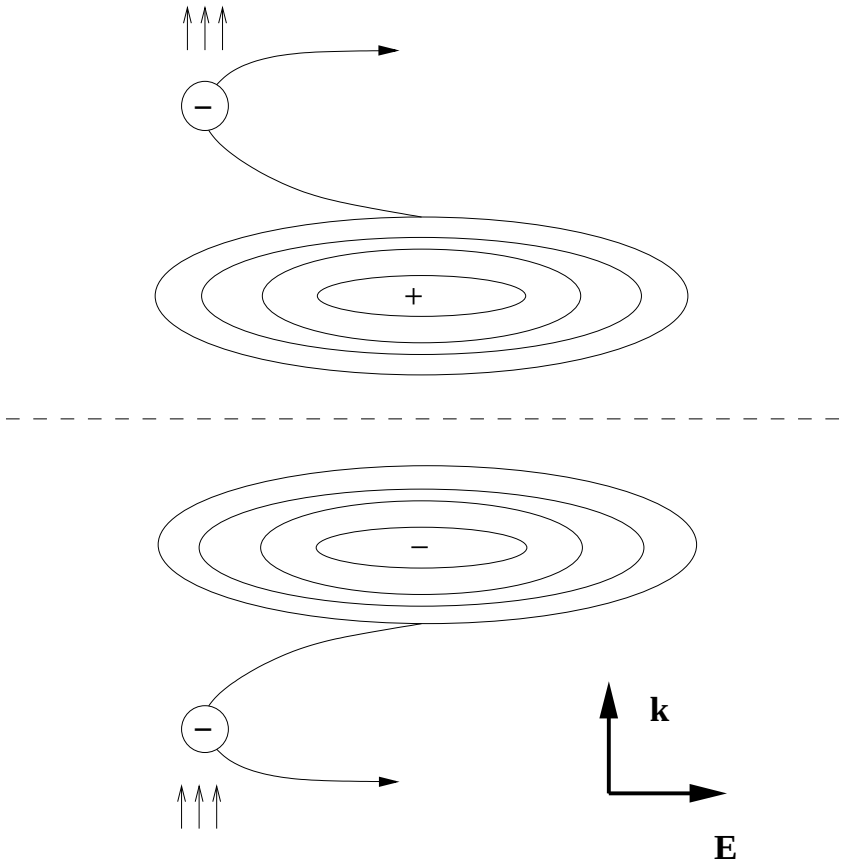

Figure 5.5: Schematic diagram of an antisymmetric wave function subject to a linearly polarized laser field with polarization vector **E** and propagation direction **k**. The dashed line symbolizes the nodal line. Ejected electrons travel preferably along the laser propagation direction. The magnetically induced electron drift helps to transfer the electron towards the core(s), as indicated by the small arrows in the lower part of the figure.

After having discussed the two basic effects, each in itself is detrimental to HHG, we introduce the concept of combining these two effects in order to increase recollisions and HHG. Fig. 5.5 shows an antisymmetric wave function subject to a strong laser field. The nodal line is parallel to the laser polarization direction. Thus, the ejected electrons exhibit an initial lateral drift orthogonal to the nodal line, i.e., *along* the laser propagation direction. We harness this drift in order to compensate for the magnetically induced drift, which is indicated by the small arrows in the figure. Hence, this leads to increased recollisions and an enhanced harmonic emission. Note that in the lower part of the figure the electron is transferred *towards* the nucleus (nuclei) as a result of the magnetically induced drift, while this drift supports the drift induced by antisymmetry *away* from the nucleus (nuclei) in the upper part of the figure. However, our results demonstrate that, as a net effect, this constellation gives rise to increased recollisions and enhanced harmonic signals. If one rotates the initial wave function so that the nodal line is oriented in a certain angle to the laser polarization direction the drift induced by antisymmetry can less successfully

counteract the magnetically induced drift. In the case that the nodal line is orthogonal to the laser polarization direction the drift caused by antisymmetry is parallel to the laser electric field. Thus, the magnetically induced drift hampers, as usual, the recollision process and HHG.

5.2 Results for H_2^+

In order to furnish evidence of the functioning of the concept outlined in the previous section we solve the time-dependent Schrödinger equation for the first excited antisymmetric state of 2D H_2^+ subject to an intense short laser pulse of linear polarization, respectively (for details of this model system see chapter (3)). The Hamiltonian which rules the electron dynamics is given by Eq. (3.9) for H_2^+. The simulations are carried out for different fixed angles Θ between the molecular axis and the laser electric field. The nuclear separation R is set at 2 a.u. The soft-core parameter ϵ (see Eq. (3.11)) has been determined to 0.58 in order to reproduce the electronic eigenenergy of -0.67 a.u. of the first excited electronic state of H_2^+ (see section (3.4)). All simulations have been accomplished with a grid spacing of 0.15 a.u. in each direction. The grid size is 3072 a.u. in the laser polarization direction and 614 a.u. in the laser propagation direction, respectively. Each propagation is performed with 2048 time steps per optical cycle.

5.2.1 Enhanced harmonic yields for H_2^+

In order to demonstrate that the drift induced by the laser magnetic field can be employed to alter the recollision process and the harmonic radiation we have performed various simulations for different angles Θ, with and without the use of the dipole approximation. Figures 5.6(a) and (b) show the harmonic spectrum obtained for a laser peak intensity of $1.4 \cdot 10^{17}\,\mathrm{W/cm^2}$ for $\Theta = 90°$ and $\Theta = 0°$, respectively. For this laser intensity the electron velocity estimated by the classical quiver velocity is in the order of 10% of the speed of light. In this regime magnetic-field effects are important but higher-order relativistic effects can be neglected [29]. In Fig. 5.6(a) it becomes evident that the harmonic signal is enhanced by several orders of magnitude by the impact of the laser magnetic field. Hence, the electron drift in the laser propagation direction which is induced by the laser magnetic field improves the recollision process and increases the overlap of the re-colliding electron with the initial bound wave function and other bound states repopulated during the pulse. This gives rise to an enhanced recombination process resulting in an increased harmonic emission, in accordance with the ideas depicted in the previous section. Our simulations show that the enhancement of the harmonic signal decreases for smaller angles Θ. But for angles Θ ranging from 70° to 90° the simulations render a considerable enhancement of the harmonic intensity for the non-dipole case compared to the dipole case. For $\Theta = 70°$ the enhancement is up to two orders of magnitude, as Fig. 5.7 shows. Fig. 5.8 illustrates that for an increased angle $\Theta = 80°$ the enhancement is up to three orders of magnitude. For $\Theta = 90°$ the largest enhancement up to six orders of magnitude is given as illustrated in Fig. 5.6(a). These results imply that although the enhancement for $\Theta = 90°$ is at maximum, there is a wide range of orientations possible for which a substantial enhancement of the harmonic signal is given. This means for practical purposes that a strict $\Theta = 90°$-alignment of the molecules is not required in order to be able to observe a considerably enhanced harmonic signal (non-dipole spectra) which is unexpectedly a few orders of magnitude higher than the theoretically predicted by the corresponding dipole spectra.

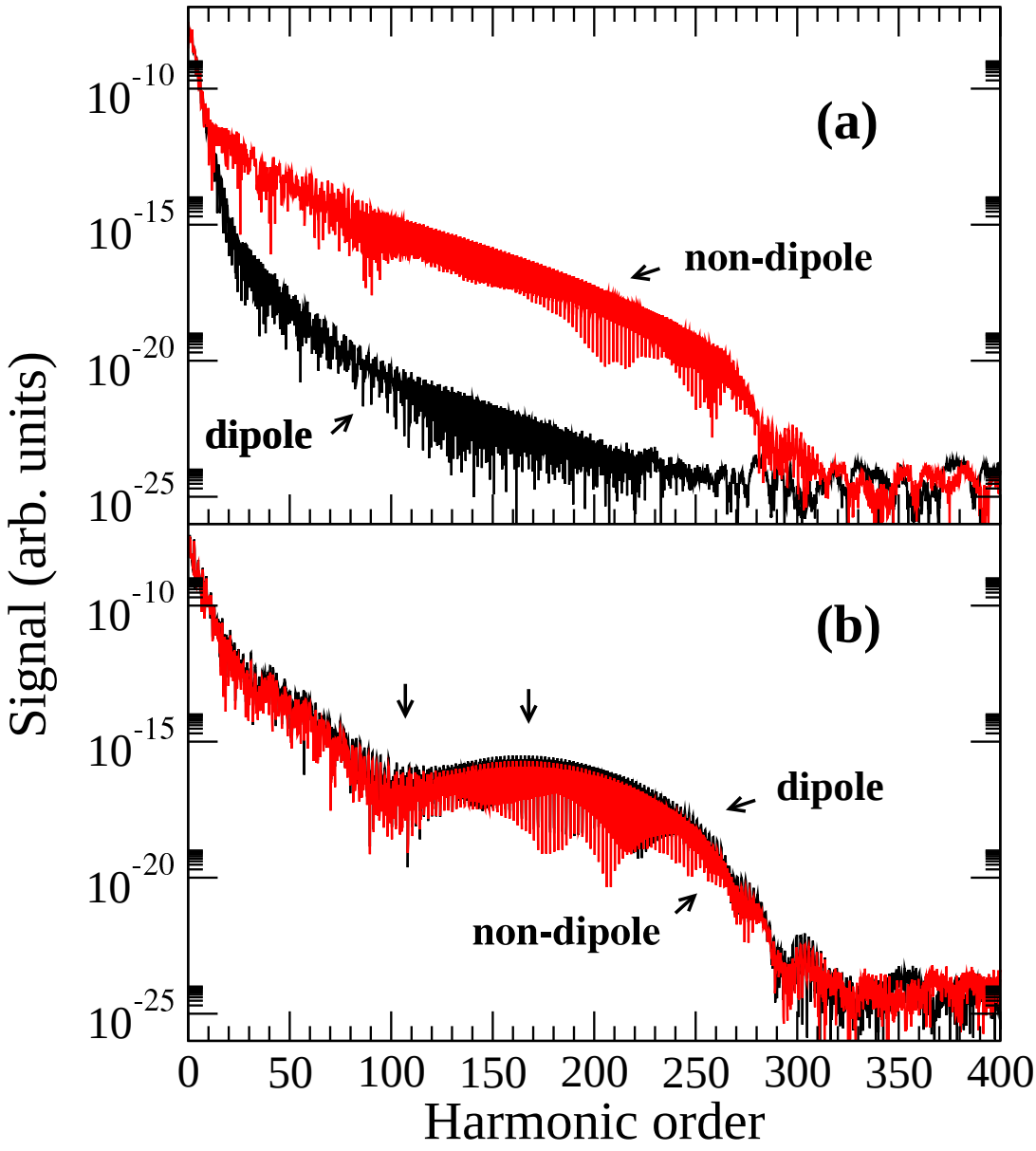

Figure 5.6: Harmonic spectrum for $\Theta = 90°$ (a) and for $\Theta = 0°$ (b) at a laser intensity of $1.4 \cdot 10^{17}\,\mathrm{W/cm^2}$ and a laser wavelength of 248 nm. The laser pulse comprises one cycle linear turn-on phase, four cycles of constant laser intensity and one cycle linear turn-off. The black line depicts the spectrum of a computation accomplished in dipole approximation, while the red one shows the harmonic signal for a simulation performed without the dipole approximation. The arrows in (b) indicate a minimum and a maximum of a two-center interference structure.

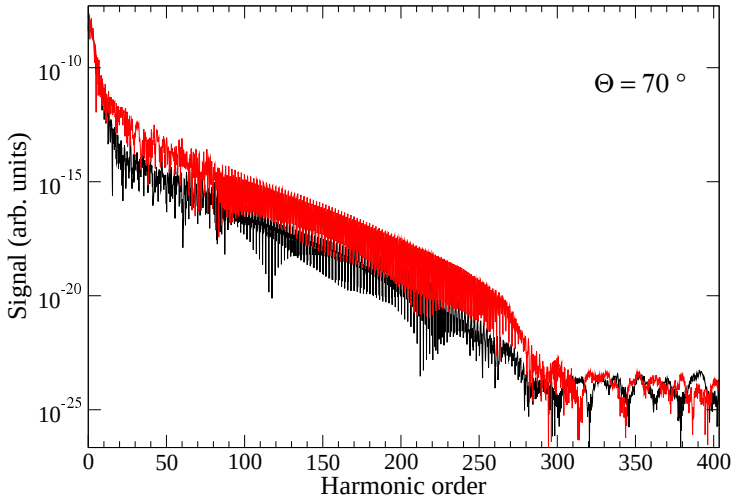

Figure 5.7: Harmonic spectra for $\Theta = 70°$. The laser parameters are the same as in Fig. 5.6. The black line illustrates the spectrum within the dipole approximation, while the red one represents the spectrum obtained beyond the dipole approximation. The laser magnetic field drift allows of an enhancement of the harmonic signal up to two orders of magnitude.

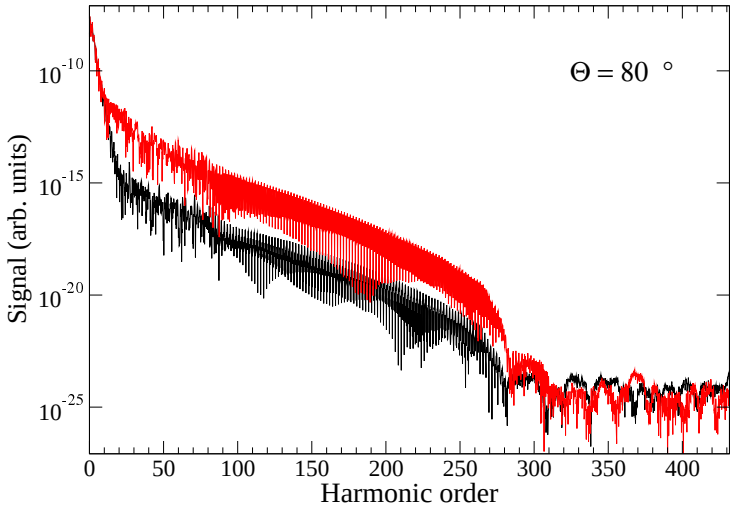

Figure 5.8: Harmonic spectra for $\Theta = 80°$. The laser parameters are the same as in Fig. 5.6. The black line illustrates the spectrum within the dipole approximation, while the red one represents the spectrum obtained beyond the dipole approximation. The laser magnetic field drift permits an enhancement of the harmonic signal up to three orders of magnitude.

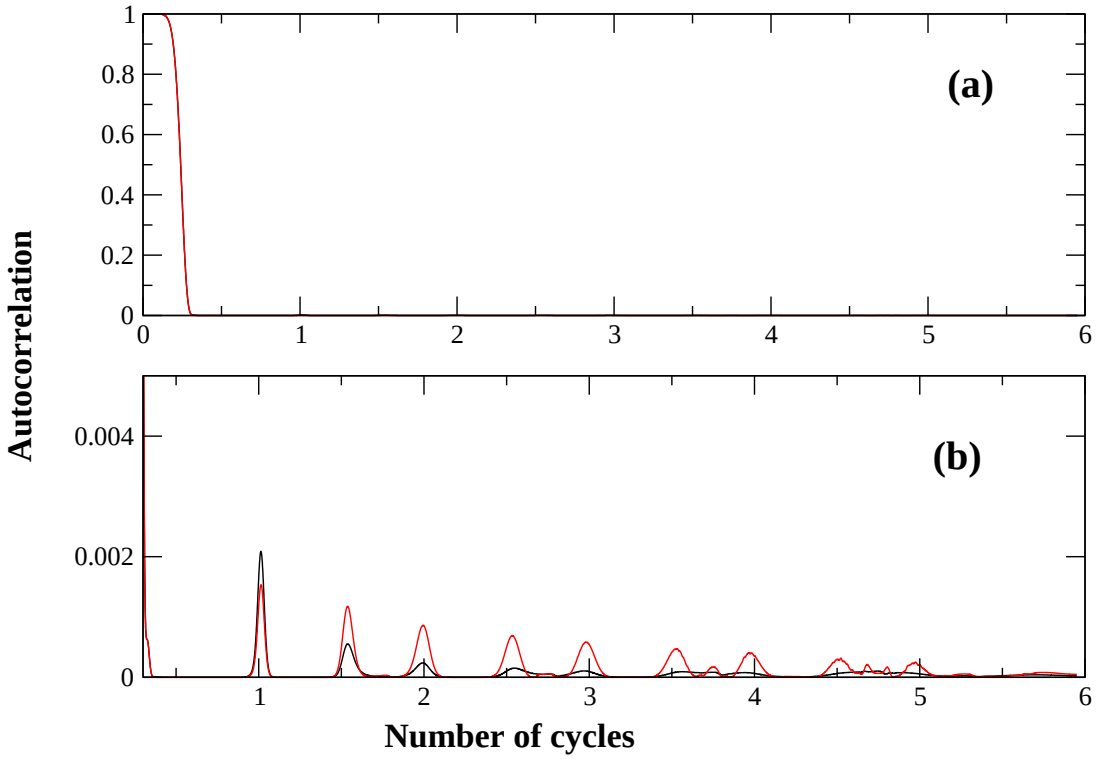

Figure 5.9: Modulus square of the autocorrelation function pertaining to the spectra presented in Fig. 5.6(a). The angle Θ is 90°.The black line illustrates the dipole result, whereas the red one depicts the result beyond the dipole approximation. The laser pulse possesses a peak intensity of $1.4 \cdot 10^{17}\,\mathrm{W/cm^2}$. The laser wavelength is 248 nm. The pulse comprises one cycle linear turn-on phase, four cycles of constant intensity and one cycle linear turn-off. For better visibility the figure is split into two parts. Part (a) illustrates the depletion of the initial first excited antisymmetric state of H_2^+ in the region of 0.3 laser cycles. Part (b) shows a stronger re-population of the initial state for larger times in the non-dipole case. This can be ascribed to the transfer of continuum population towards the nuclei due to the drift induced by the laser magnetic field.

For angles in the vicinity of $\Theta = 0°$ the harmonic signal is weakened by the magnetically induced drift, as expected and described in the previous section. Figure 5.6 (b) illustrates this for $\Theta = 0°$. There, the electron drift due to the antisymmetry of the molecular orbital is irrelevant, but signatures of two-center interference occur, as indicated by arrows. We remark that the spectra shown in Figs. 5.6(a),(b), Fig. 5.7 and Fig. 5.8 do not obey the common 3.17-cut-off rule Eq. (2.8) which would predict a cut-off harmonic order of 515. This can be attributed to the rapid depopulation of the weakly bound initial state already during the rising edge of the pulse. Note that we are in the over-the-barrier, i.e. not in the tunneling regime.

This results in the alternate depletion and re-population of the initial state, as the modulus square of the autocorrelation function illustrates in Fig. 5.9. This figure belongs to the simulations depicted in Fig. 5.6(a). The black line represents a simulation performed

within the dipole approximation, while the red one shows the situation beyond the dipole approximation. The angle Θ is 90°. For better visibility the figure is split into part (a) and (b). Part (a) illustrates the rapid depletion of the initial state within the first 0.3 laser cycles in the turn-on phase of the pulse. Calculating classical trajectories (with vanishing initial velocities starting at the origin and birth times in the region of 0.3 laser cycles) for this laser pulse, in the spirit of the Corkum model (2.3.2), yields cut-off harmonic orders in the range of 250, which corresponds to the situations in the spectra of Fig. 5.6, Fig. 5.7 and Fig. 5.8. Part (b) of Fig. 5.9 shows the further course of the autocorrelation. Comparing the red line with the black indicates an enhanced re-population of the initial state in the course of the interaction with the laser pulse. This can be attributed to the fact that the laser magnetic field transfers, as a net effect, continuum population towards the nuclei leading to an enhanced re-population of the initial state.

Projecting the propagated wave function onto other bound states reveals also the depletion and re-population of these states during the pulse. Fig. 5.10 shows the population of the symmetric ground state over the duration of the laser pulse. These data belong to the spectra depicted in Fig. 5.6(a). The black line which represents the result within the dipole approximation lies on the population=0-axis. This means that in the case of the dipole approximation no population of the symmetric ground state takes place, which can be attributed to the conservation of antisymmetry of the propagated wave function. The red line shows the population the ground state beyond the dipole approximation. In this case the antisymmetry of the propagated wave function is not conserved, since the magnetically induced drift transfers, as a net effect, continuum population *towards* the nuclei, i.e. in the direction perpendicular to the nodal line. (This corresponds to the situation outlined in the lower part of the schematic diagram Fig. 5.5).

Fig. 5.11 shows the population of the second excited state during the interaction with the laser pulse. This figure belongs also to the harmonic spectra depicted in Fig. 5.6(a). As in the previous figure, the second excited state is not populated within the dipole approximation (black line). The red line shows alternate population and depletion of this state over the duration of the laser pulse in the non-dipole case.

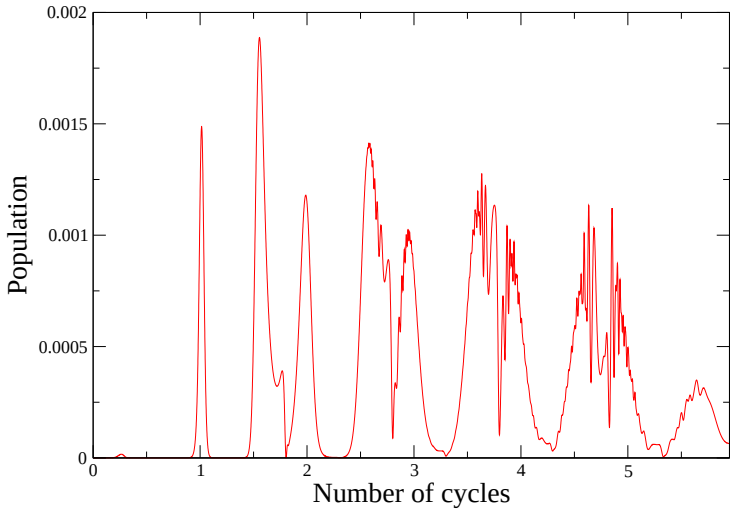

Figure 5.10: Population of the symmetric ground state during the interaction of a laser pulse with a peak intensity of $1.4 \cdot 10^{17}\,\mathrm{W/cm^2}$ with the first excited antisymmetric state of H_2^+ for $\Theta = 90°$. The same pulse as in Fig. 5.6(a) is applied. These results belong to the spectra shown in Fig. 5.6(a). Within the dipole approximation, the ground state is not populated, as the black line which is identical to zero over the entire pulse duration shows. Beyond the dipole approximation the ground state is populated as the red line illustrates. The reason for this is the enhanced recollision dynamics according to our concept.

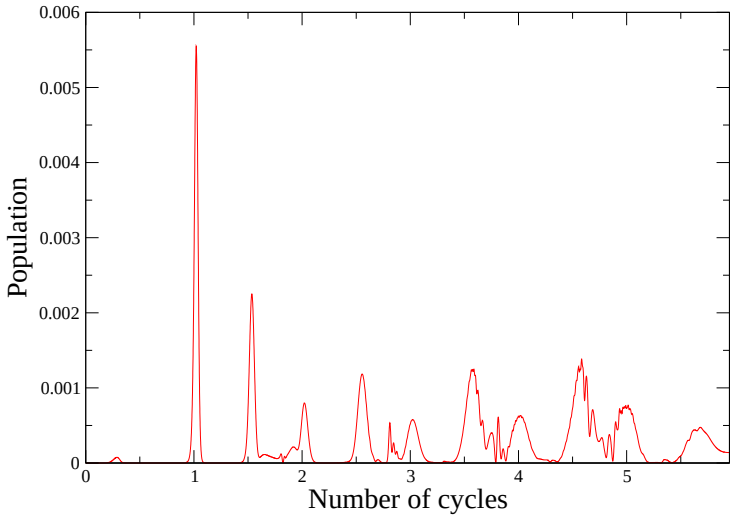

Figure 5.11: Population of the second excited state during the interaction with the same laser pulse as in Fig. 5.6(a) for $\Theta = 90°$. These results belong to the harmonic spectra shown in Fig. 5.6(a). Within the dipole approximation there is no population of the second excited state (black line), while beyond this approximation the enhanced recollision dynamics due to the laser magnetic field leads to the population of this state (red line).

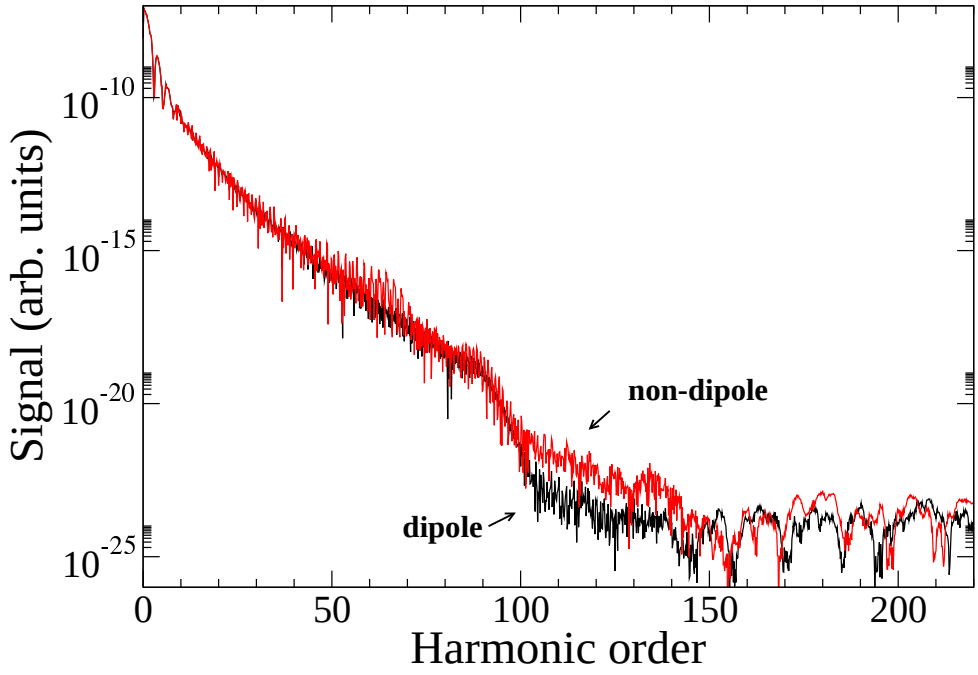

Figure 5.12: Harmonic spectrum for $\Theta = 90°$ at a laser intensity of $3.51 \cdot 10^{16}\,\mathrm{W/cm^2}$ and a laser wavelength of 248 nm. The black and the red line represents the harmonic spectrum obtained with and without the application of the dipole approximation, respectively. The laser pulse comprises one cycle linear turn-on phase, four cycles of constant intensity and one cycle linear turn-off.

Even for a lower laser intensity of $3.51 \cdot 10^{16}\,\mathrm{W/cm^2}$ we find that for the antisymmetric molecular orbital investigated in this section the laser magnetic field can still notably contribute to an enhancement of the harmonic signal if the angle Θ is 90°. This is illustrated in Fig. 5.12. A distinct enhancement of the harmonic signal is discernible. This implies that, depending on the orientation of the molecular axis, recollision effects in antisymmetric molecular orbitals are very sensitive to magnetic-field effects.

We now focus on the illustration of the enhancement mechanism of the recollision process. We show in Figs. 5.13(a) and (b) a snapshot of the density of the electronic wave function after 3.75 optical cycles. The simulation has been carried out in the dipole approximation for Fig. 5.13(a), while Fig. 5.13(b) has been obtained without employing the dipole approximation. Due to the rapid depopulation of the initial state the initial wave function is not visible in the figures. Considering the symmetry of the density with regard to the nodal line ($y = 0$) one recognizes in Fig. 5.13(a) that the antisymmetry of the wave function is conserved. The lateral spreading of the wave packet along the molecular axis increases considerably during the interaction with the laser field; in Fig. 5.13(a) it extends roughly up to 150 a.u. along the y-axis. In contrast, in the non-dipole case in Fig. 5.13(b) the antisymmetry of the wave function is broken.

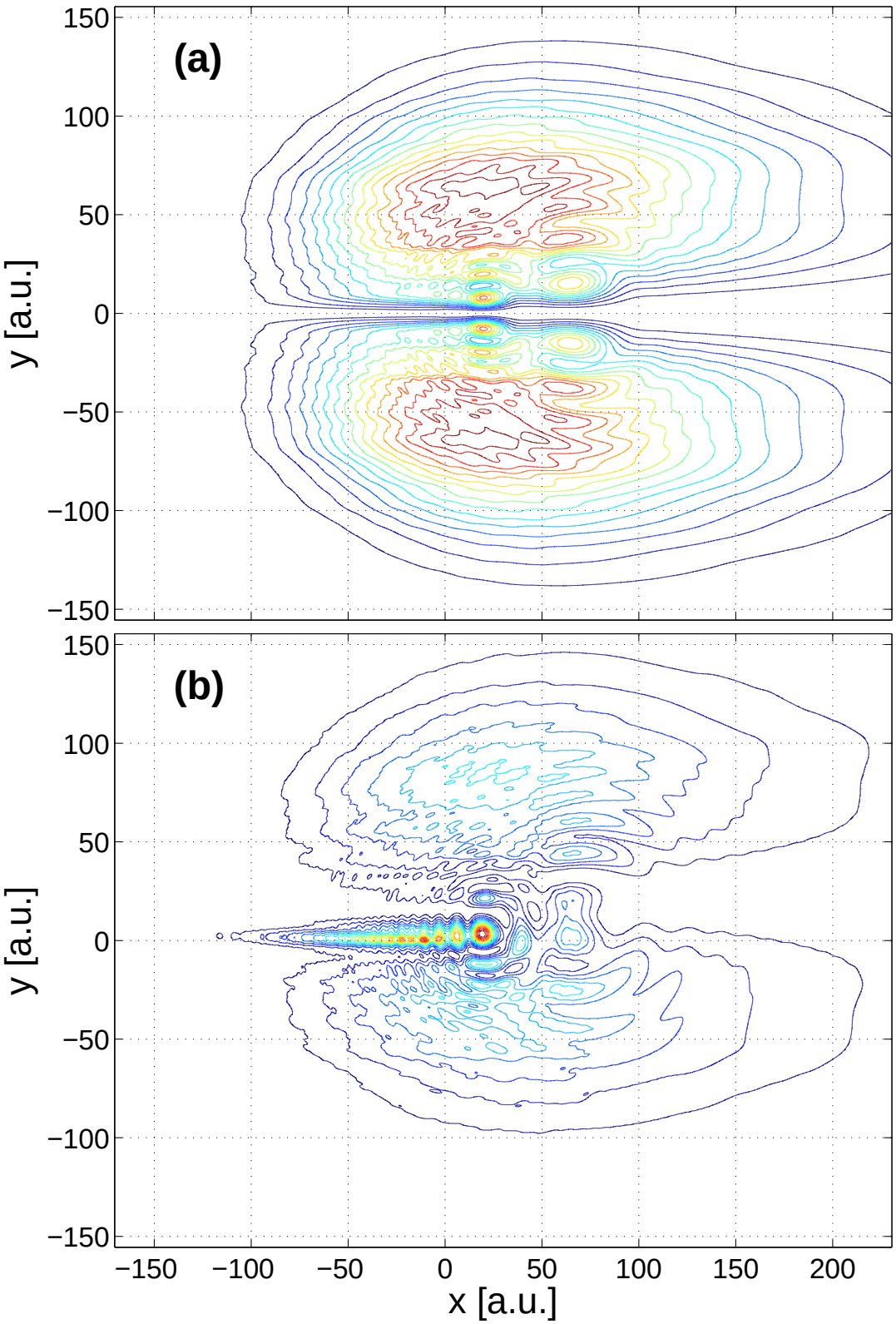

Figure 5.13: Contour plot of the density of the electronic wave function for $\Theta = 90°$ and a laser intensity of $1.4 \cdot 10^{17}\,\mathrm{W/cm^2}$ (molecular axis along the y-axis) after 3.75 laser cycles: (a) in dipole approximation and (b) beyond the dipole approximation.

A distinct drift of the wave packet towards the laser propagation direction is clearly discernible in comparison with the dipole-case in Fig. 5.13(a). Supplementary classical Monte Carlo simulations, where the initial conditions have been determined according to the initial densities of the antisymmetric wave function and its counterpart in momentum space, do confirm the wave packet spreading depicted in Figs. 5.13(a), (b) (see the following section (5.2.2)). In addition, Fig. 5.13(b) illustrates a concentration of density in the vicinity of the former nodal line ($y = 0$), suggesting that bound states are re-populated during the action of the pulse. The combination of both effects leads, in comparison with the results obtained in dipole approximation, to a highly more efficient recollision of the wave packet with the population in the core region.

In conclusion, we have seen that, depending on the orientation of the molecular axis, the electron drift induced by the laser magnetic field can be harnessed to increase the recollision probability of electrons for antisymmetric molecular orbitals. In particular, the harmonic signal can be considerably enhanced by means of the magnetically induced electron drift.

5.2.2 Monte Carlo simulations

We have performed complementary Monte Carlo simulations in order to mimic the spreading of the quantum wave packet in the OTBI regime. Hereby, the initial positions and momenta have been drawn according to the distribution given by the electronic density of the initial state and the Fourier transform of the initial wave function, respectively (see section (3.5)). After having drawn the initial conditions, the classical canonical equations have been solved for the same laser pulse as in the quantum simulations (Fig. 5.13) with and without employing the dipole approximation. The initial quantum state is, as in Fig. 5.6(a) and Fig. 5.13, the first excited state of H_2^+ with the nodal line being parallel to the laser polarization direction. We have performed the Monte Carlo simulations with 5 000 classical trajectories. The results are shown in Fig. 5.14 and Fig. 5.15: Fig. 5.14 has been obtained within the dipole approximation, whereas Fig. 5.15 represents results without having carried out the dipole approximation. Note that in the latter case the symmetry of the ensemble with regard to the y =0-line is disturbed. The still recognizable (disturbed) nodal line has moved in the laser propagation direction.
The ratio of the width in laser propagation direction to the one in laser polarization direction of the Monte Carlo "wave packet" is similar to the corresponding ratio of the quantum wave packet depicted in Figs. 5.13 (a), (b). As expected, wave packet spreading can be reliably mimicked in the OTBI regime by means of the Monte Carlo method. However, the population of bound states as suggested by Fig. 5.13(b) cannot be modelled via this Monte Carlo approach which is based on classical mechanics.

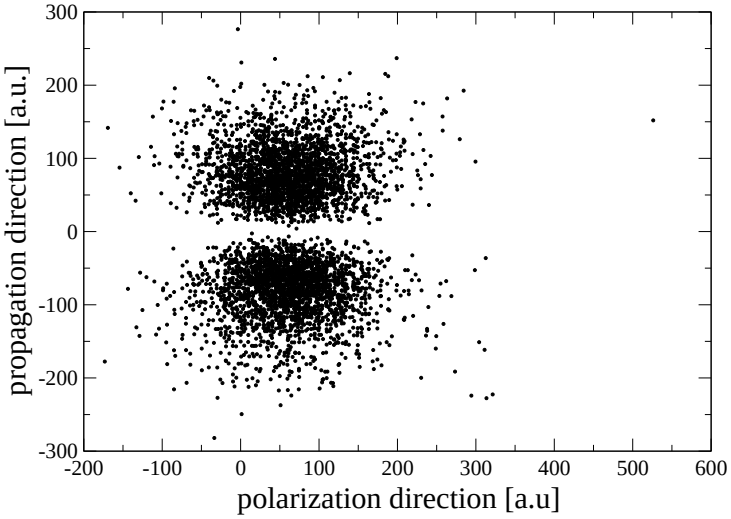

Figure 5.14: Classical Monte Carlo ensemble with 5000 classical trajectories after 3.75 cycles for the scenario and the parameters of Fig. 5.13(a). The dipole approximation is carried out. The quantum wave packet spreading can be reliably mimicked by means of the Monte Carlo method. The conservation of the nodal line can also be modelled via the Monte Carlo technique.

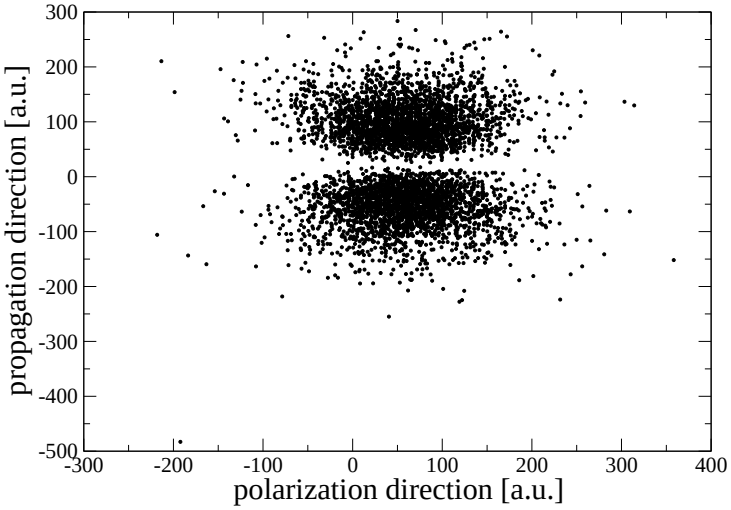

Figure 5.15: Classical Monte Carlo ensemble with 5000 classical trajectories after 3.75 cycles for the scenario and the parameters of Fig. 5.13(b). In this case the laser magnetic field is taken into account. The Monte Carlo wave packet is displaced in the laser propagation direction corresponding to the situation in Fig. 5.13(b). However, the population of bound states, as also suggested by Fig. 5.13(b), cannot be mimicked by this Monte Carlo approach based on classical mechanics.

5.2.3 Alignment and optimization

Fig. 5.16(a),(b) show the spectra of an H_2^+ model ion subject to a laser pulse of a peak intensity of $4.3 \cdot 10^{17}\,\mathrm{W/cm^2}$. The trapezoidal envelope of the pulse comprises one cycle linear turn-on, two cycles of constant intensity and one cycle linear turn-off. The wavelength of the laser pulse is 248 nm, corresponding to a KrF-laser system. The solid line depicts the spectrum obtained in the dipole approximation, whereas the dashed line represents a spectrum calculated without having employed the dipole approximation. Fig. 5.16(a) demonstrates for $\Theta = 90°$ a considerable enhancement of the harmonic signal up to six orders of magnitude as a result of the circumstance that in this constellation the drift due to antisymmetry counteracts the laser induced drift - in accordance with the concept presented. This is attributed to the compensation of both drifts. Evidently, the maximum enhancement of the harmonic signal is found for the $\Theta = 90°$-orientation.
Figs. 5.16(b), (c) address an issue that becomes relevant for the experimental realization. The question is for which orientation of the orbital the harmonic radiation is dominant in a sample of randomly oriented molecules. If the harmonic radiation for the $\Theta = 0°$-orientation prevailed over other directions a pre-alignment of the molecules selecting angles in the range of $\Theta = 90°$ would be required in order to be able to observe a harmonic signal which would be higher than simulations in the dipole approximation would predict. Fig. 5.16(b) shows the non-dipole spectra for a laser peak intensity of $4.3 \cdot 10^{17}\,\mathrm{W/cm^2}$ for $\Theta = 0°$ and $\Theta = 90°$, respectively. For this high laser intensity the enhancement of the harmonic signal due to the magnetically induced drift is so high that the harmonic signal for $\Theta = 90°$ exceeds the one for $\Theta = 0°$ in a wide range of harmonic orders. In this case a pre-alignment of the orbitals is not necessary.
Decreasing the laser intensity to $1.4 \cdot 10^{17}\,\mathrm{W/cm^2}$ leads to a weaker enhancement of the harmonic signal for $\Theta = 90°$. The simulation shows that in this case the harmonic radiation for $\Theta = 0°$ prevails in the cut-off regime, as depicted in Fig. 5.16(c).

We now address a question that arises from the classical trajectory depicted in Fig. 5.1(c). This figure suggests that the drift due to the antisymmetry of the orbital over-compensates the drift induced by the laser magnetic field, also in the quantum case. The question comes up whether for a given antisymmetric orbital the increase of the laser magnetic field would result in a even better recollision dynamics. For this purpose, we have varied the intensity of the applied laser pulse, which changes the strength of the laser magnetic field. For an orientation of $\Theta = 90°$, Fig. 5.17 illustrates the harmonic spectra for laser intensities ranging from $1.4 \cdot 10^{17}\,\mathrm{W/cm^2}$ to $5.6 \cdot 10^{17}\,\mathrm{W/cm^2}$. These results are obtained beyond the dipole approximation; except the black line depicts a dipole spectrum for an intensity of $1.4 \cdot 10^{17}\,\mathrm{W/cm^2}$ in order to assess the magnitude of all dipole spectra. The question of an optimal laser intensity, i.e. of a laser intensity for which the harmonic signal reaches a maximum, cannot be simply answered because the maximum depends on the harmonic order considered. For a harmonic order around 100 a laser intensity of $2.2 \cdot 10^{17}\,\mathrm{W/cm^2}$ yields the highest signal. In the region of the 150th harmonic order an intensity of $3.2 \cdot 10^{17}\,\mathrm{W/cm^2}$ is recommendable. Furthermore, there is a range of harmonic orders around 400 for which an intensity of $4.3 \cdot 10^{17}\,\mathrm{W/cm^2}$ is favorable. Increasing the laser intensity further results in an over-all decline in harmonic intensity. This information given might be relevant for an experimental detection of the harmonic radiation.

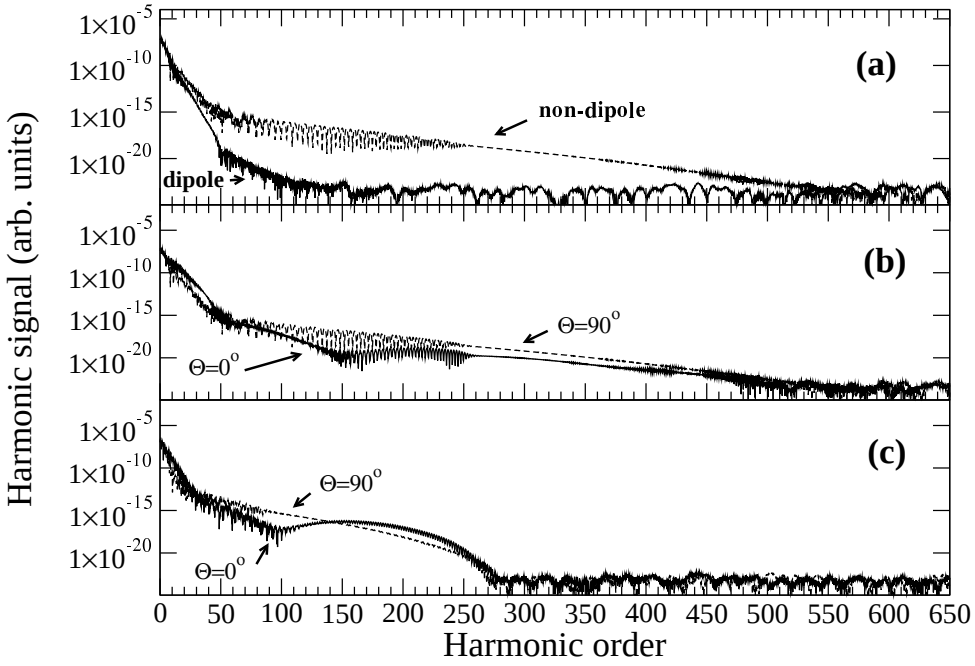

Figure 5.16: Harmonic spectra for the first excited antisymmetric state of H_2^+ exposed to a trapezoidal laser pulse which comprises a one-cycle linear turn-on phase, two cycles of constant intensity and one-cycle linear turn-off.
(a): Harmonic spectra for $\Theta = 90°$ obtained within the dipole approximation (solid line) and without this approximation (dashed line), respectively, are shown. The laser peak intensity is $4.3 \cdot 10^{17}\,\mathrm{W/cm^2}$. The comparison of both spectra illustrates the enhancement of the harmonic signal up to six orders of magnitude owing to the enhanced recollision dynamics caused by the magnetically induced drift in the laser propagation direction.
(b): Comparison of the harmonic spectra for $\Theta = 0°$ (solid line) and $\Theta = 90°$ (dashed line) for a laser peak intensity of $4.3 \cdot 10^{17}\,\mathrm{W/cm^2}$. Both spectra are obtained without employing the dipole approximation. The enhancement of the harmonic signal owing to the magnetically induced drift is such that the $\Theta = 90°$-radiation is dominant.
(c): For a decreased laser intensity of $1.4 \cdot 10^{17}\,\mathrm{W/cm^2}$ the harmonic radiation for $\Theta = 0°$ (solid line) prevails in the cut-off region over the one for $\Theta = 90°$ (dashed line). Both spectra are computed beyond the dipole approximation.

But one may ask the rather academic question whether the strength of the laser magnetic field which is naturally present for a given specific laser intensity is optimal for the recollision dynamics. As the following considerations show, this question must be answered in the negative, in general.

In a numerical experiment we change artificially the strength of the laser magnetic field for a given laser electric field. The mere increase in intensity of a laser field would lead to an enhancement of the laser magnetic field but the corresponding harmonic spectra would also change due to an altered ionization-recombination dynamics with a strongly enhanced ionization rate. Thus, these harmonic spectra should not be compared with each

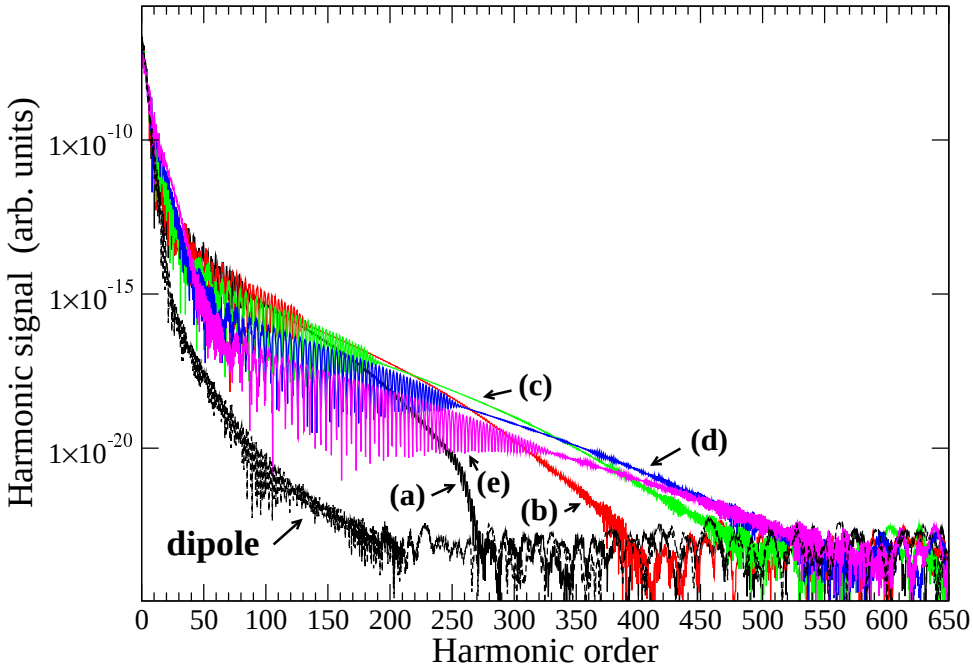

Figure 5.17: Harmonic spectrum of the first excited antisymmetric state of H_2^+ subject to a linearly polarized laser pulse of trapezoidal shape which comprises one cycle linear turn-on phase, two cycles of constant intensity and one cycle linear turn-off. The orbital is oriented in an angle of $\Theta = 90°$. The laser wavelength is 248 nm. The laser intensity is varied from $1.4 \cdot 10^{17}\,\mathrm{W/cm^2}$ to $5.6 \cdot 10^{17}\,\mathrm{W/cm^2}$. All spectra shown are obtained without employing the dipole approximation, except the one indicated by "dipole". This dipole spectrum for an intensity of $1.4 \cdot 10^{17}\,\mathrm{W/cm^2}$ serves to show the orders of magnitude of the dipole spectra. The labels (a)-(e) help to identify the spectra pertaining to various laser intensities I: (a): $I = 1.4 \cdot 10^{17}\,\mathrm{W/cm^2}$ (black), (b): $I = 2.2 \cdot 10^{17}\,\mathrm{W/cm^2}$ (red), (c): $I = 3.2 \cdot 10^{17}\,\mathrm{W/cm^2}$ (green), (d): $I = 4.3 \cdot 10^{17}\,\mathrm{W/cm^2}$ (blue), (e): $I = 5.6 \cdot 10^{17}\,\mathrm{W/cm^2}$ (pink).
For different harmonic orders there is an optimal intensity yielding the highest harmonic signal (see text).

other from a purely theoretical point of view. Therefore, we intend to change artificially the laser magnetic-field drift by changing the laser magnetic field itself, however, without changing the ionization process. A laser field in dipole approximation is applied by means of a spatially independent vector potential $A_x^{laser}(t)$. In order to tune the laser magnetic field artificially the term $A_x^{art}(y,t) - A_x^{art}(t)$ which yields an artificial laser magnetic field [1] whose strength can be tuned independently of the actual laser field (given by $A_x^{laser}(t)$) is added. The vector potential $A_x^{art}(y,t)$ and its counterpart in the dipole approximation $A_x^{art}(t)$ describe additional laser fields whose electric peak amplitude e_a can be employed to define the artificial magnetic field.

[1] The term $A_x^{art}(y,t) - A_x^{art}(t)$ also yields an electric field. But this is negligible for not too large y. The ionization-recollision dynamics and the velocity of recolliding wave packets in laser polarization direction is determined by the dominant laser electric field belonging to $A_x^{laser}(t)$.

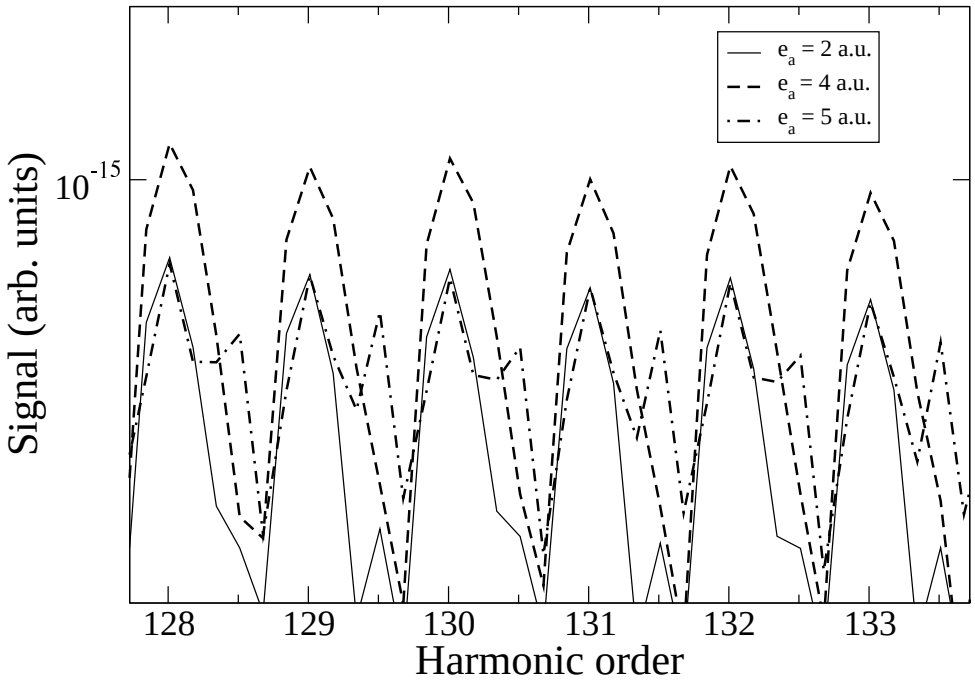

Figure 5.18: Cut-out of harmonic spectra. For a given laser electric field with a peak amplitude of 2 a.u. the laser magnetic field is changed artificially. The strength of this magnetic field is tuned by the peak amplitude e_a of a combination of artificial auxiliary laser fields (see text). Note that e_a =2 a.u. yields a laser magnetic field which is identical to the naturally induced one. If the artificial laser magnetic field is not too strong it leads to a higher harmonic signal than the naturally given magnetic field can provide.

Fig. 5.18 shows a cut-out [2] of harmonic spectra with different e_a, i.e. with differently strong drifts in the laser propagation direction. For these simulations the laser electric peak amplitude implemented in $A_x^{laser}(t)$ is 2 a.u. For e_a =2 a.u. (see legend in the figure) the strength of the laser magnetic field corresponds to the naturally given one for this laser field. A different simulation without the dipole approximation (without artificial fields) yields the same spectrum. Thus, the spectrum in Fig. 5.18 with e_a =2 a.u. is to be considered as a reference spectrum to which spectra with artificial laser magnetic fields are compared. If the laser magnetic field strength is artificially doubled (e_a =4 a.u in Fig. 5.18) the harmonic signal strength can still be enhanced by one order of magnitude. This means that the natural laser magnetic field does not provide an optimal recollision dynamics. Increasing the artificial magnetic field further to e_a =5 a.u results in a reduced harmonic signal. In this case the laser magnetic field drift over-compensates the drift induced by antisymmetry.
These considerations make antisymmetric orbitals particularly attractive for even stronger laser fields entering a regime where higher-order relativistic effects become important and an efficient recollision process is desired.

[2] For better visibility we have picked out a cut-out of the spectra but the observations discussed in the context of Fig. 5.18 remain in principle valid for the entire spectra.

5.3 Results for excited states of hydrogen-like ions

In this section we demonstrate how the concept depicted in section (5.1) can be successfully transferred to atomic ions. A too rapid depletion of the initial state is suppressed by the high binding energies of the ions. Therefore, in comparison with molecules, atomic ions exhibit a higher harmonic signal strength and an easier realization of the 3.17-formula. We investigate atomic orbitals that are antisymmetric with respect to a nodal plane. In order to study the influence of the laser magnetic field we perform our simulations with and without employing the dipole approximation for the laser field. Our simulations consist in the direct numerical integration of the time-dependent Schrödinger equation in two dimensions. The antisymmetric atomic orbitals under consideration are the 2D-equivalents of real the 2p-orbitals of hydrogen-like ions.

We make use of the crucial property of antisymmetric wave functions: The density of the corresponding momentum wave function which belongs to the antisymmetric initial wave function in coordinate space possesses also a nodal line. The atomic antisymmetric 2D-eigenfunctions possess in coordinate space a quite similar shape as the 2D-eigenfunctions of H_2^+. Therefore, the atomic ones also exhibit the discussed properties of the momentum wave function. This means that the concept which is delineated in section (5.1) and which is applied to H_2^+ in the previous section should also work for antisymmetric orbitals of atomic ions.

Before we confirm the concept by simulations, we would like to note that the preparation of the real 3D 2p-orbitals can be accomplished by a modestly intense preparation pulse of appropriate frequency and polarization according to the common dipole selection rules ($\Delta l = \pm 1$, $\Delta m = 0, \pm 1$), neglecting the fine structure. Starting from the ground state of a hydrogen-like system with quantum numbers $(n = 1, l = 0, m = 0)$ one can, for instance, excite the $(n = 2, l = 1, m = 0)$-state by means of light which is polarized along the chosen z-axis. The nodal plane of this state is perpendicular to this axis. By choosing the polarization direction of this preceding pulse it is possible to obtain the desired orientation of the wave function with regard to the polarization direction of the following strong laser pulse. In order to establish the 3D scenario of our concept one would have to irradiate the strong laser pulse perpendicular to the nodal plane of the $(n = 2, l = 1, m = 0)$-state.

For the purpose of the comparison with atomic ions, Figs. 5.19 (a), (b) show the spectra of an H_2^+ model ion subject to a laser pulse of a peak intensity of $1.0 \cdot 10^{17}\,\mathrm{W/cm^2}$. The black lines depict spectra obtained in the dipole approximation, whereas the red lines represent spectra calculated without having employed the dipole approximation. Fig. 5.19 (a) shows the corresponding dipole and nondipole results for an orientation of the molecular axis of $\Theta = 0^\circ$ to the laser polarization direction, respectively. In the nondipole case the drift due to antisymmetry and the magnetically induced drift take effect in different directions. The magnetically induced drift which is detrimental to harmonic generation cannot be compensated by the drift due to antisymmetry since this drift is directed in laser polarization direction. As a result, the decrease in efficiency of the recollision process

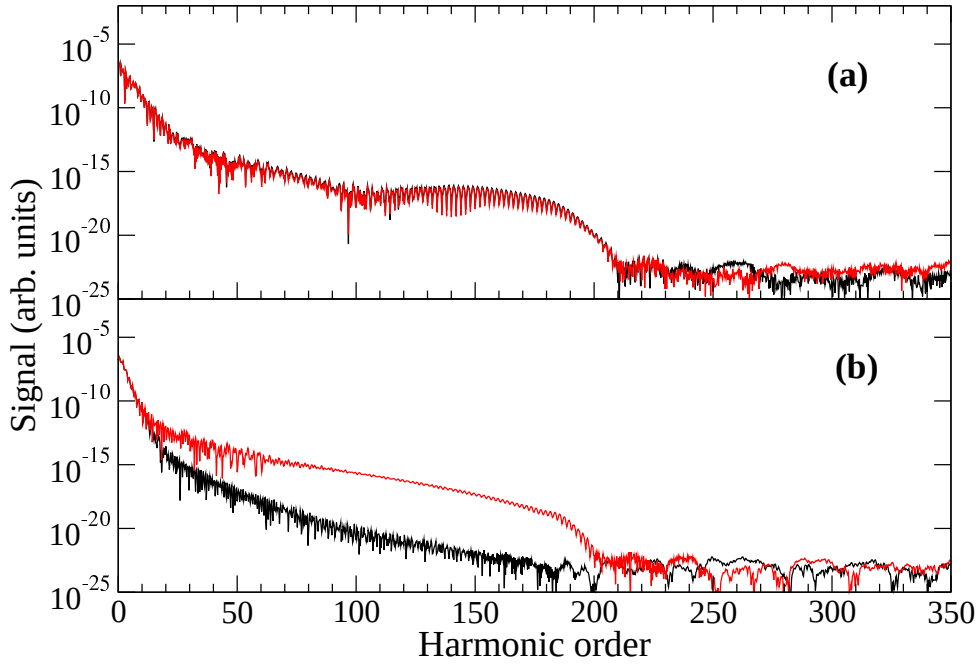

Figure 5.19: Harmonic spectra of the first excited antisymmetric state of H_2^+ subject to a linearly polarized laser pulse of $1.0 \cdot 10^{17}\,\mathrm{W/cm^2}$. The trapezoidal shape of the pulse comprises one cycle linear turn-on phase, two cycles of constant intensity and one cycle linear turn-off. The laser wavelength is 248 nm. The numerical grid comprises 3072 a.u. in the laser polarization direction and 614 a.u. in the laser propagation direction. The black lines describe spectra obtained in the dipole approximation, whereas the red ones represent calculations beyond this approximation. Note that the cut-off (N_{max} =373) predicted by Eq. (2.8) is not attained owing to the rapid depletion of the initial wave function already in the turn-on phase of the pulse. (a): $\Theta = 0°$: The magnetically induced drift results in a slight decrease in harmonic intensity, (b): $\Theta = 90°$: Dramatic enhancement in harmonic intensity due to the compensation of both drifts.

leads to a decrease in harmonic intensity (see Fig. 5.19 (a)). In contrast to this, Fig. 5.19 (b) demonstrates for $\Theta = 90°$ a notable enhancement of the harmonic signal as a result of the circumstance that in this constellation the drift due to antisymmetry counteracts the laser induced drift - in accordance with the concept presented. However, as Fig. 5.19 points out, the application of very intense laser pulses to weakly bound molecular systems like H_2^+ leads to the problem that the harmonic spectra do not obey the cut-off rule (2.8) due to the rapid depletion of the initial state in the turn-on phase of the pulse. The spectra drop prior to the cut-off harmonic order N_{max}=373 predicted by Eq. (2.8). This means that wave packets which give rise to the emission of the highest cut-off harmonics are not ejected.
This problem can be avoided by employing strongly bound systems like hydrogen-like atomic ions.

Fig. 5.20 illustrates the realization of the cut-off rule for the first excited antisymmetric

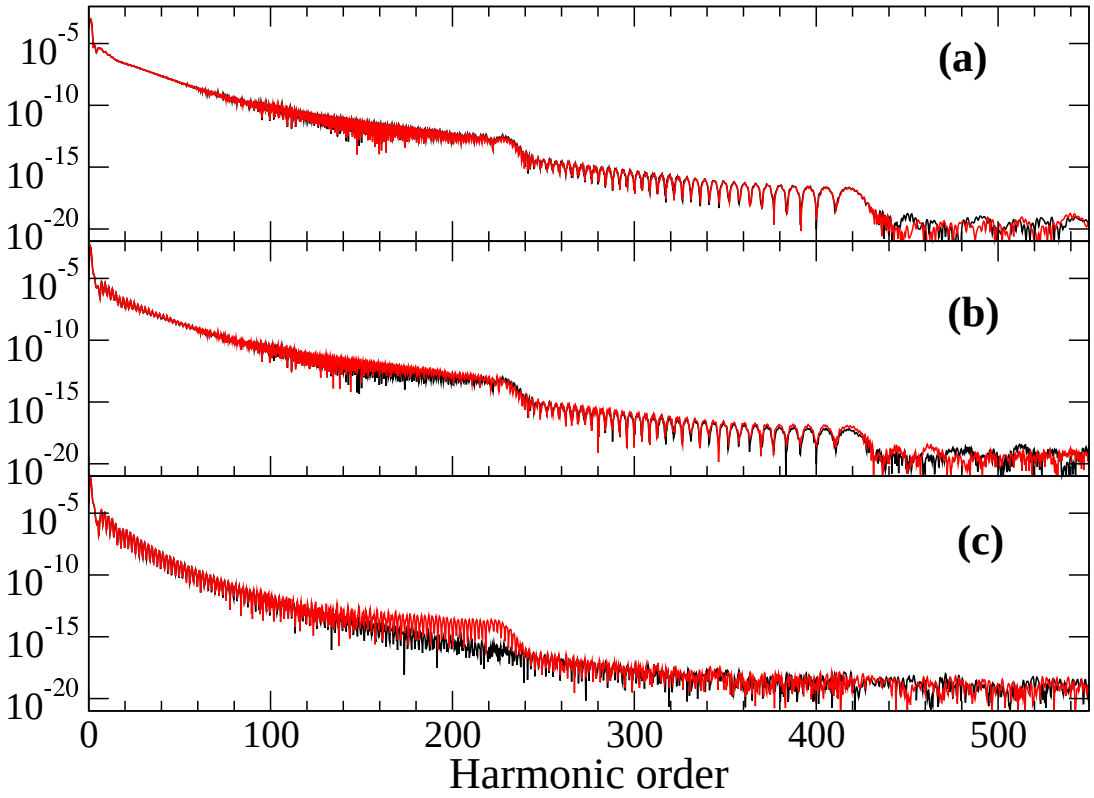

Figure 5.20: Harmonic spectra of the first excited antisymmetric state of N^{6+} subject to a linearly polarized sine laser pulse of $1.0 \cdot 10^{17}\,\mathrm{W/cm^2}$. The trapezoidal shape of the pulse comprises one cycle linear turn-on, two cycles of constant intensity and one cycle linear turn-off. The laser wavelength is 248 nm. The grid consists of 3072 a.u. in the laser polarization direction and 614 a.u. in the laser propagation direction. The black lines describe results computed in the dipole approximation, beyond-dipole results are represented by red lines. The cut-off predicted by Eq. (2.8) is achieved for this highly charged ion. (For the definition of Θ see text.)
(a): $\Theta = 0°$: Slightly reduced harmonic signal due to magnetically induced drift,
(b): $\Theta = 45°$: Partially enhanced harmonic signal. The two drifts start to counteract.
(c): $\Theta = 90°$: Considerable enhancement in harmonic intensity due to the most efficient compensation of both drifts for this alignment.

state of N^{6+} subject to the same laser intensity of $1.0 \cdot 10^{17}\,\mathrm{W/cm^2}$ as in Fig. 5.19. Different orientations of this atomic wave function with regard to the laser polarization direction are taken into consideration. The core potential is symmetric around the origin for this *atomic* system and therefore the only distinguished direction is represented by the nodal line of the wave function. The angle Θ describes the orientation of the wave function. It is the angle between the line perpendicular to the nodal line and the laser polarization direction (x-axis). The core potential is modelled by a soft-core potential

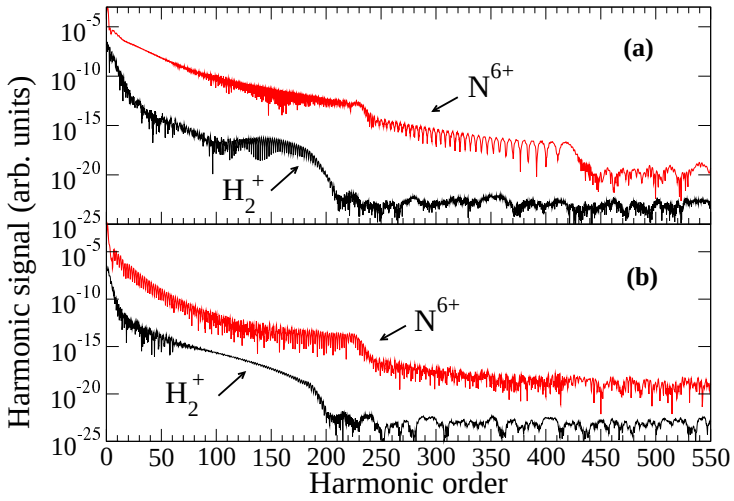

Figure 5.21: Comparison of harmonic spectra of N^{6+} with H_2^+. Both substances are found in the first excited antisymmetric state prior to the interaction with the same laser pulse as in Fig. 5.19 and Fig. 5.20. The red lines depict N^{6+}-spectra, while the black ones represent H_2^+-spectra. In part (a) the nodal line of the corresponding wave function is perpendicular to the laser polarization direction ($\Theta = 0°$); in part (b) it is parallel to it ($\Theta = 90°$). All spectra have been obtained without employing the dipole approximation. The figure demonstrates the enhanced harmonic emission in the case of the atomic ion N^{6+} owing to the higher binding energy (see text).

(see Eq. (3.10):

$$V_{ion}(x,y) = -\frac{10.96}{\sqrt{1+x^2+y^2}} \quad . \tag{5.1}$$

This choice of the soft-core parameters in (5.1) ensures that the eigenenergy of -6.1 a.u. of the corresponding first excited initial state coincides with the value of the real (3D) first excited state of the hydrogen-like system N^{6+}.

Figs. 5.20 (a), (b) demonstrate that the cut-off harmonic order N_{max}=403 is now achieved, where I_p=6.1 a.u., U_P=21.4 and ω_L=0.18 a.u., as the simulations for $\Theta = 0°$ and $\Theta = 45°$ yield. As expected, there is a decrease in the harmonic signal for $\Theta = 0°$ owing to the magnetically induced drift, while in the case of $\Theta = 45°$ both drifts start to mutually counteract already leading to a partial enhancement of the harmonic signal. For $\Theta = 90°$ a maximum enhancement of the harmonic signal by two orders of magnitude is found (see Fig. 5.20 (c)). In this constellation the drift due to the antisymmetry of the wave function appears to prevail which gives rise to the fact that no efficient harmonic generation in the cut-off regime is possible.

Another advantage of applying atomic ions consists in the over-all increase in the harmonic signal in comparison with H_2^+. Fig. 5.21 compares harmonic spectra of N^{6+} and H_2^+; both subject to the same laser pulse as in Fig. 5.20. The results have been achieved without the

dipole approximation. As in Fig. 5.20, the first excited antisymmetric state with $I_p = 6.1$ a.u. is taken into consideration for N^{6+}, while in the case of H_2^+ the first electronically excited state with $I_p = 0.67$ a.u. is investigated. In part (a) of the figure the nodal lines of both the H_2^+ state and the N^{6+} state are orthogonal to the laser polarization direction, whereas in part (b) the corresponding nodal lines are parallel to the laser polarization direction. The red lines represent the N^{6+}-spectra and the black ones illustrate the H_2^+-spectra.

Note that the N^{6+} and the H_2^+-results have been obtained with the same code, merely in the case of H_2^+ we have a double-well soft-core potential instead. In contrast to the H_2^+-spectra, the N^{6+}-spectra exhibit a considerably enhanced harmonic signal by many orders of magnitude. This makes the investigation of antisymmetric states of atomic ions particularly interesting in view of experiments. The enormous difference in the signal strengths can be attributed to the higher binding energies of atomic ions, since they do not suffer from rapid depletion despite the very high laser intensity. This gives rise to the circumstance that the matrix element $\langle\psi_{\text{init}}(t)|-\frac{\partial V_{\text{ion}}}{\partial x}|\psi_{\text{rec}}(t)\rangle$ ($|\psi_{\text{init}}(t)\rangle$ denotes the initial wave function and $|\psi_{\text{rec}}(t)\rangle$ represents the recolliding wave packet), which is decisive for the recombination process, turns out to be considerably larger, since the occupation of $|\psi_{\text{init}}(t)\rangle$ at the time t of recollision is substantially higher for highly charged atomic ions. This is responsible for the enhanced harmonic emission observed.

For the illustration of the electron dynamics in N^{6+} in the case of an orientation with the nodal line parallel to the laser polarization direction , Fig. 5.22 shows snapshots of the logarithm of the electronic density during the interaction with the laser pulse. The snapshots are taken after one cycle ((a),(c)) and after 1.4 cycles ((b),(d)), respectively. Parts (a),(b) are obtained in the dipole approximation, while parts (c),(d) represent non-dipole results. In all four snapshots it is clearly visible that the major part of the population remains at the position of the nucleus with the nodal line parallel to the laser polarization direction (x-axis). This shows that the ion is able to withstand the strong laser pulse, i.e. only a minor part of the population is transferred into the continuum. Therefore, it becomes directly obvious that rapid initial ionization is suppressed in the case of atomic ions. This clearly represents an advantage of antisymmetric atomic ions over fragile molecules. (Density plots in the molecular case are given in Fig. 5.13, where substantial ionization occurs already in the turn-on phase of the laser pulse. Note that in Fig. 5.13 the logarithm of the electron density is not required to be taken, whereas in Fig. 5.22 this measure is necessary in order to be able to observe the dynamics of the tunneled wave packets.)
Fig. 5.22(a) illustrates the ejection of wave packets in the laser polarization direction. It demonstrates clearly by its sickle-shaped density distribution (indicated by "sickle") the drift along the laser propagation direction (y-axis) owing to antisymmetry. Moreover, the symmetry of the density distribution with regard to the nodal line (y-axis) expresses the conservation of antisymmetry of the wave function (Fig. 5.22(a),(b)) in the dipole case. In contrast to this, the antisymmetry is broken beyond the dipole approximation; the density is displaced in the laser propagation direction (towards the positive y-axis), see Fig. 5.22(c),(d). Figs. 5.22(b)(d) show on the one hand new ejection of wave packets, going out left (indicated by "sickle"), as the laser field has changed its sign. On the other hand, even more interestingly, one can directly see the interplay of the drift due to anti-

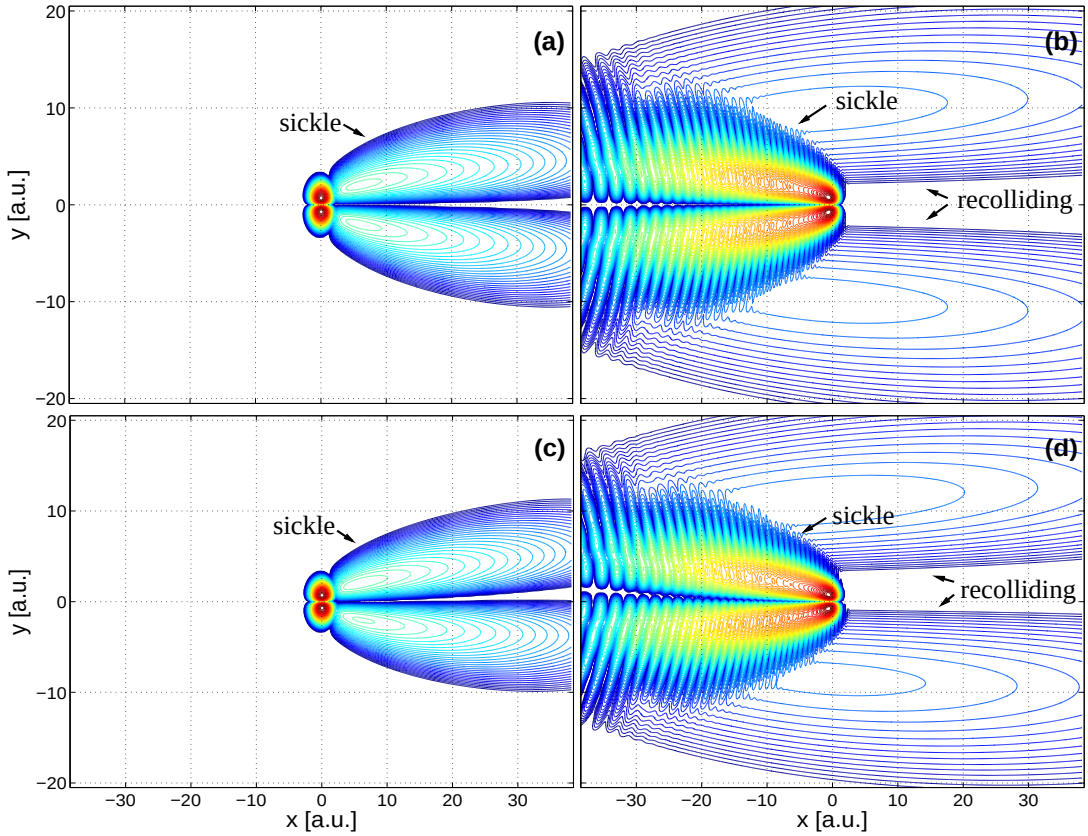

Figure 5.22: Snapshots of the logarithm of the electronic density during the laser pulse interaction after one cycle ((a),(c)) and 1.4 cycles ((b),(d)). Plots with 60 contour lines are shown, only values of the density above 10^{-12} are taken into account. Parts (a),(b) depict dipole results, whereas parts (c), (d) illustrate the non-dipole case. The sickle-shaped density distribution of outgoing wave packets (indicated by "sickle") towards the right side in parts (a), (c) and towards the left in part (b), (d) show directly the lateral drift due to antisymmetry. In parts (b), (d) the broad wave packet (indicated by "recolliding") recollides with the wave packets in the vicinity of the nucleus. Comparing (b) with (d) shows that the enhanced recollision dynamics owing to the interplay of the drift due to antisymmetry and the magnetically induced drift in the laser propagation direction (y-axis) is clearly visible; note the distance between the widespread recolliding wave packet and the $y = 0$-line.

symmetry and the drift induced by the laser magnetic field: The widespread wave packets in parts (b),(d) (indicated by "recolliding") represent wave packets which are accelerated back towards the core and which have been ejected in the laser cycle before. Comparing part (b) with (d) shows that the distance of the widespread wave packet to the $y = 0$-line in the lower part of Fig. 5.22(d) is smaller than the corresponding one in 5.22(b). This illustrates clearly the enhanced recollision dynamics of the returning wave packet with the initial state if one compares the density of Fig. 5.22(b) with the one of Fig. 5.22(d) in the vicinity of the origin. The fringes in the density distribution in Fig. 5.22(b),(d) suggest

interference of wave packets ejected towards the left with the widespread recolliding wave packets.
The enhanced recollision dynamics for antisymmetric atomic wave functions gives rise to an increased emission of high-order harmonic radiation, where the realization of the cut-off formula (2.8) and a substantially larger harmonic signal in comparison to molecular orbitals is possible in spite of the very high laser intensities.

5.4 Two-center-interference effects beyond the dipole approximation

To conclude this chapter, we present novel aspects found in two-center interference structures (see also section (2.3.4)). This section is to be regarded as an outlook for future research, since not all questions raised in this section can be answered.

Fig. 5.23 sheds new light on two center-interference effects in HHG-spectra which can be attributed to the presence of two nuclei. Two-center interference effects lead to typical minima and maxima in harmonic spectra. The location of these extrema is strongly dependent on the orientation of a diatomic molecule to the polarization direction of a strong laser pulse. The occurrence of these structures is due to the interference of the recolliding wave packets with the initial state at the positions of the nuclei. This interference is strongly dependent on the orientation of the nuclei. Thus, different orientations of the molecule result in different positions of these extrema in the spectra. One obtains simple formulas predicting the positions of the extrema (see section (2.3.4)). These formulas have been confirmed for the symmetric ground state wave function of H_2^+ in a situation where the dipole approximation has been justified [45]. If we transfer these formulas to our situation of first excited antisymmetric state of H_2^+ the minima N_{min} would be sited at harmonic orders (with $\lambda = 2\pi/v$, where v is the electron velocity, and $v^2/2 = N_{min}\,\omega$):

$$N_{min} = \frac{2\pi^2 m^2}{R^2 \cos^2\Theta\,\omega_L} \quad m = 0, 1, 2..., \tag{5.2}$$

where ω_L=0.18 a.u. denotes the laser frequency. Fig. 5.23 shows the positions of conspicuous interference minima for $\Theta = 0°$ and $\Theta = 50°$ for laser intensities of $I = 1.0{\cdot}10^{17}\,\mathrm{W/cm^2}$ and $I = 1.4 \cdot 10^{17}\,\mathrm{W/cm^2}$, respectively. The black lines represent spectra in the dipole approximation, while the red ones illustrate non-dipole spectra. For $m = 2$ Eq. (5.2) yields $N_{min} = 107$ for the $\Theta = 0°$-alignment. This is in accordance with the spectra shown in Fig. 5.23(a),(c) for both the dipole and the non-dipole case, as indicated by the arrows. However, for angles Θ different from 0° the positions of the minima in the spectra do not comply with Eq.(5.2) (For $\Theta = 50°$: $N_{min} = 65$ for $m = 1$ or $N_{min} = 260$ for $m = 2$). Instead, for $\Theta = 50°$ Fig. 5.23(b) yields a minimum at the 131st harmonic order in the dipole approximation or at the 151st harmonic order in the non-dipole case for a laser intensity of $I = 1.0 \cdot 10^{17}\,\mathrm{W/cm^2}$, as indicated by arrows. For a higher laser intensity of $I = 1.4 \cdot 10^{17}\,\mathrm{W/cm^2}$ (Fig. 5.23(d)) the minimum is found at the 153rd harmonic order in the dipole case and at the 181st harmonic order in the non-dipole case.
Thus, we remark two new characteristics for these two-center interference minima: First, we find clear signatures of magnetic-field effects in two-center interference structures. For $\Theta \neq 0°$ we see a displacement of the minima towards higher harmonic orders in the non-dipole case. This might be attributed to the circumstance that the recolliding wave packets which are responsible for the interference minima gain additional kinetic energy by momentum transfer of the laser photons. For $\Theta = 0°$ the displacement in the laser propagation direction of the recolliding wave packet does not seem to affect the interference but merely reduces the harmonic signal.

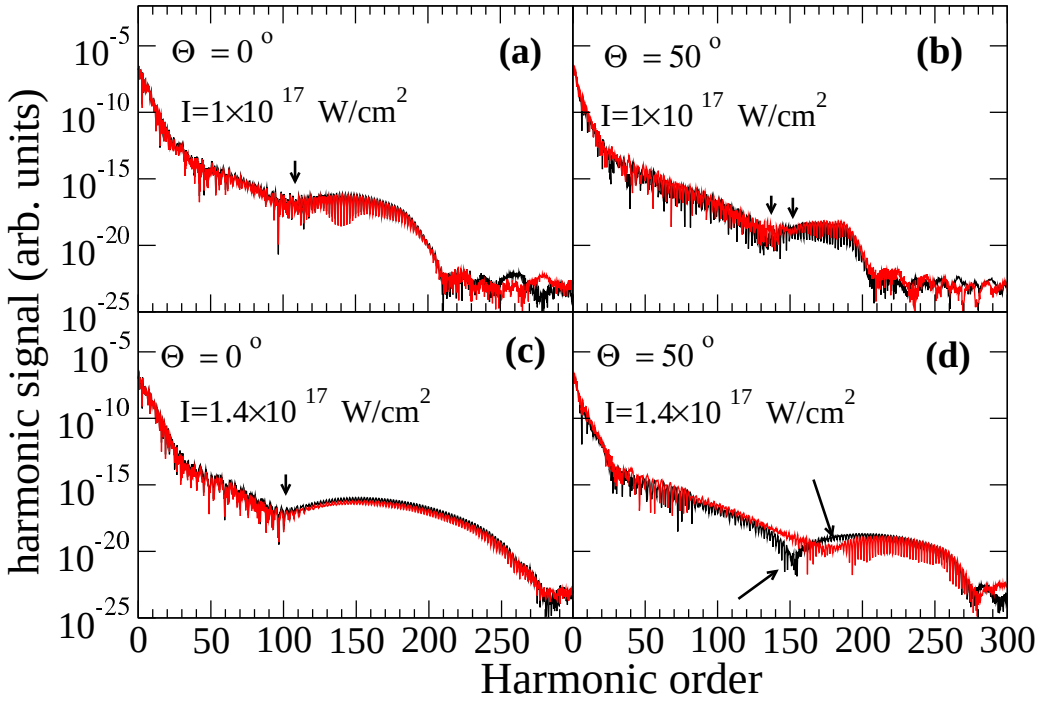

Figure 5.23: High-harmonic spectra for the antisymmetric first excited state of H_2^+. The black lines show spectra obtained in the dipole approximation, while the red ones illustrate non-dipole results. The arrows indicate the positions of two-center interference minima. For $\Theta = 0°$ these minima lie in the vicinity of the 107th harmonic order which is predicted by Eq. (5.2), see parts (a),(c). Part (b) shows that for $\Theta = 50°$ and an laser intensity of $I = 1.0 \cdot 10^{17}\,\mathrm{W/cm^2}$ the conspicuous minimum is located at the 135th harmonic order (dipole case) or at the 151st harmonic order (non-dipole case), respectively. For a higher laser intensity of $I = 1.4 \cdot 10^{17}\,\mathrm{W/cm^2}$, see part (d), the minimum is found at the 153rd harmonic order (dipole case) or at the 181st harmonic order (non-dipole case). This shows the dependence of two-center interference structures on the laser intensity for *antisymmetric* molecular orbitals. Furthermore, the drift induced by the laser magnetic field turns out to be responsible for a displacement of these interference structures towards higher harmonic orders in this high-intensity regime.

Second, for the first excited *antisymmetric* state of H_2^+ the positions of the minima do not correspond to the positions predicted by Eq.(5.2) for $\Theta \neq 0°$ (even in the dipole approximation). One reason for this might be that for antisymmetric initial states the ionization dynamics depends strongly on the orientation, i.e. the shape and the structure of the continuum wave packet depends strongly on how the electron is promoted into the continuum. In the succeeding recollision-recombination process the details of the recolliding wave packets might play a decisive role for the interference with the initial state.

This is backed by our observation that the positions of these minima depend also on the intensity of the laser pulse (Fig. 5.23(b),(d)).

Further research should be dedicated to these two-center interference effects for *antisymmetric* states. However, the dependence of the interference minima on the laser intensity suggests that an analytical description would be challenging.

Chapter 6

Conclusion and outlook

In this thesis, the interaction of strong laser pulses with atomic and molecular orbitals has been investigated. In particular, we have focused on high-order harmonic generation (HHG). New mechanisms for the enhancement of this radiation, which provides a source of highly coherent short-wavelength light and which represents the basis for the generation of attosecond pulses, have been presented. Numerical integration of the time-dependent Schrödinger equation has been used to achieve these findings.

The theoretical basis for the understanding of HHG in a single atom or molecule has been reviewed in chapter (2) of this thesis. We have surveyed the three-step recollision model of HHG which has been employed to account for the novel mechanisms studied in the framework of this thesis. Furthermore, the electron drift in the laser propagation direction which electrons exhibit after laser-induced ionization of atoms or molecules has been discussed. This drift is attributed to the Lorentz force which is due to the laser magnetic field. For the situations investigated in this thesis, the laser magnetic field has not been negligible. The electron drift in the laser propagation direction has been in the focus of this thesis. This drift leads, via the interplay with the attraction of the nucleus, to an oscillatory motion which gives rise to high-order harmonic generation.
In the first project, the impact of a static magnetic field on this kind of harmonic radiation [1] has been investigated. Thereby, it has been found that a relatively weak static magnetic field (on the order of 10T) may cause an increase or a decrease in the harmonic signal, depending on the harmonic order considered. The advantage of this method over other existing approaches is that weak static magnetic fields (around 10T) are sufficient to observe a significant effect in the spectrum, while other methods require static magnetic fields on the order of thousands of Tesla. The results show also the potential for our method to measure static magnetic fields.

In the second project, the electron drift in the laser propagation direction has been studied in the context of the properties of antisymmetric wave functions subject to intense laser pulses. Exposed to a strong laser pulse, wave functions with mirror antisymmetry with

[1] Usually HHG from the electron motion in the laser polarization direction is considered.

respect to a nodal line give rise to a drift of ejected wave packets perpendicular to the nodal line. In this thesis a novel concept of enhancing the recollision dynamics via the combination of the drift in the laser propagation direction and the electron motion due to antisymmetry has been proposed. Corresponding numerical simulations have revealed that an increase in the harmonic signal up to several orders of magnitude is possible. This mechanism has been proven for antisymmetric states of both H_2^+ and hydrogen-like atomic ions. Furthermore, it has been pointed out that the drift due to antisymmetry can be employed to compensate for the drift induced by the laser magnetic field in order to allow of enhanced recollisions and HHG. This is possible in a regime of laser parameters where the magnetically induced drift alone would result in a significant decrease in recollisions. The mechanism investigated has clear potential to permit recollisions for even higher laser intensities than the ones applied in this thesis. In other words, there is evidence that our method yields recollisions for highly relativistic laser-ion interactions despite the severe impact of the drift induced by the laser magnetic field. Atomic ions would be most appropriate for this scenario. As we have shown, our method works still for antisymmetric states of atomic ions. Although our method depends on the orientation of the antisymmetric wave function, we have shown that it can be used for a wide range of orientations. This means that a strict alignment of antisymmetric molecular orbitals with regard to the laser polarization direction is not compulsory, which would facilitate an experimental realization. For H_2^+ we have found that for very high laser intensities an alignment of the molecules in a sample is not necessary, since the signal from molecules oriented perpendicular to the laser polarization direction (i.e. the molecular axis is orthogonal to the laser polarization direction) prevails over signals from other directions. For weaker laser pulses alignment (but not strict alignment) is required as our simulations have shown.
Moreover, we have indicated optimal laser intensities with respect to the maximum harmonic signal. The alignment of antisymmetric atomic orbitals can be even more easily accomplished by irradiating a sample of atoms in the ground state with a weak pre-pulse with appropriate frequency and polarization.

The main results in this thesis have been obtained by the direct numerical integration of the time-dependent Schrödinger equation for a 2D model atom/molecule. A detailed discussion of this 2D model and the numerical split-operator technique is given in chapter (3).

Concluding this thesis we would like to point out future research possibilities.
A lot of theoretical work (see the survey given in section (4.1)) has been dedicated to the investigation of atoms or molecules subject to a combination of laser and static magnetic field. Our approach has revealed that distinct effects in the harmonic spectra due to a static magnetic field of the order of 10T are observable, while other studies require much stronger magnetic fields. Therefore, we hope that our work will prod an experimental realization of our scheme.

In the context of antisymmetric molecular orbitals exposed to intense laser pulses, the nuclear motion has not been included in the model of H_2^+ which has been employed in

this thesis. If one took the full nuclear motion into account one would have to solve the time-dependent Schrödinger equation in three dimensions: one dimension would be claimed by the nuclear degree of freedom and two dimensions would be needed for the electron motion in the laser polarization direction and the laser propagation direction. As yet, this is not feasible numerically for the parameter regime in the focus of this thesis, i.e. long laser wavelengths and high intensities which require large numerical grids. Further progress in this direction would be desirable in order to assess the influence of the nuclear motion. Although our concept of enhancing the recollision dynamics via a combination of the drift induced by the laser magnetic field and the drift due to antisymmetry works regardless the nuclear motion, the nuclear motion is expected to result in an overall decrease in the harmonic signal for both the spectra within the dipole approximation and beyond [81]. A better assessment of the impact of the nuclear motion would be desirable. As an alternative approach to the numerical method, it is conceivable that an extension of the Lewenstein model would help to evaluate the effect of the nuclear motion. Attempts to include the nuclear motion within the Lewenstein formalism have already been made (see the first two references in [81]). However, this has been carried out in the dipole approximation for the laser field. On the other hand, the Lewenstein model has already been formulated beyond the dipole approximation, i.e. magnetic-field effects have been included [44]. The future task would be to bring both achievements together in a new Lewenstein formalism taking both the laser magnetic field and the nuclear motion into account.

Moreover, new effects with regard to two-center interference in H_2^+ have been found in this thesis. Antisymmetric states exhibit interference minima in the harmonic spectrum. These are located at positions that cannot be predicted by the theory (see section (2.3.4)) which has been only tested for the symmetric ground state so far [45]. These effects have been present already within the dipole approximation. Our simulations have revealed that the positions of the minima depend on the laser intensity. This suggests that the shape of the recolliding continuum wave packets may be vital for antisymmetric initial orbitals. Therefore, a derivation of an analytic formula describing the positions of the minima would be complex. Alternatively, a numerical experiment could be performed by modelling a wave packet which recollides with the initial antisymmetric orbital. This approach has been attempted in preliminary simulations for section (5.4) but the problem of modelling an appropriate shape of the recolliding wave packet, which is believed to be essential, is still open. Progress in this direction would be desirable.

Finally, we have found in this thesis that the laser magnetic field gives rise to a displacement of the interference minima. A new approach beyond the dipole approximation which fully accounts for this effect would be interesting.

Bibliography

[1] K. W. Madison,*et al.* , Phys. Plasmas **11**, 270 (2004);
H. Popescu, *et al.*, Phys. Plasmas **12**, 063106 (2005);
S. Ter-Avetisyan *et al.*, Phys. Plasmas **12**, 012702 (2005);
S. Karsch *et al.*, Phys. Rev. Lett. **91**, 015001 (2003);
S. Dobosz, *et al.*, Phys. Rev. Lett. **95**, 025001 (2005);
S. B. Hansen *et al.*, Phys. Rev. E **71**, 016408 (2005);
U. Teubner *et al.*, Phys. Rev. Letters **92**, 185001 (2004);
Th. Ergler, *et al.*, Phys. Rev. Lett., **97** 193001 (2006).

[2] D. Strickland and G. Mourou, Opt. Commun. **56** 219 (1985).

[3] D. E. Spence, P. N. Kean and W. Sibbet, Opt. Lett. **16** 42 (1991);
L. Xu, C. Spielmann, F. Krausz and R. Szipöcs, Opt. Lett. **21** 1259 (1996).

[4] J. Andruszkow *et al.*, Phys. Rev. Lett. **85**, 3825 (2000);
V. Ayvazyan *et al.*, Phys. Rev. Lett. **88**, 104802 (2003);
V. Ayvazyan *et al.*, Nucl. Instrum. Methods Phys. Res. A *507*, 368 (2003);
XFEL-STI Interim Report, Jan 11, 2005, web: `http://xfel.desy.de`, DESY, Hamburg (2005).

[5] T. Brabec and F. Krausz, Rev. Mod. Phys. **72** 545 (2000).

[6] P. Agostini and L. F. DiMauro, Rep. Prog. Phys. **67**, 813 (2004);
M. Drescher, M. Hentschel, R. Kienberger, G. Tempea, C. Spielmann, G. A. Reider, P. B. Corkum, and F. Krausz, Science **291**, 1923 (2001); M. Hentschel *et al.*, Nature **414**, 509 (2001);
R. López-Martens *et al.*, Phys. Rev. Lett. **94**, 033001 (2005).

[7] R. Kienberger, E. Goulielmakis, M. Uiberacker, A. Baltuska, V. Yakovlev, F. Bammer, A. Scrinzi, Th. Westerwalbesloh, U. Kleinberger, U. Heinzmann, M. Drescher, and F. Krausz, Nature **427**, 817 (2004);
E. Goulielmakis, M. Uiberacker, R. Kienberger, A. Baltuska, V. Yakovlev, A. Scrinzi, Th. Westerwalbesloh, U. Kleinberger, U. Heinzmann, M. Drescher, and F. Krausz, Science **305**, 1267 (2004).

[8] A. Modena *et al.*, Nature **377** 606 (1995).

[9] T. Ditmire *et al.* Nature **398** 489 (1999);
E. E. B. Campbell *et al.*, Phys. Rev. Lett. **84**, 2128 (2000);
H. Wabnitz *et al.*, Nature **420**, 482 (2002);
E. Cormier, P.-A. Hervieux, R. Wiehle, B. Witzel, and H. Helm, Eur. Phys. J. D **26**, 83 (2003).

[10] Gy. Farkas, Cs. Tóth, S. D. Moustaizis, N. A. Papadogiannis, and C. Fotakis, Phys. Rev. A **46** (1992) R3605;
P. A. Norreys *et al.*, Phys. Rev. Lett. **76**, 1832 (1996).

[11] Y. I. Salamin, S. X. Hu, K. Z. Hatsagortsyan, and C. H. Keitel, Phys. Rep. **427**, 41 (2006);
D. B. Milošević and F. Ehlotzky, Adv. At., Mol., Opt. Phys. **49**, 373 (2003);
W. Becker, F. Grasbon, R. Kopold, D. B. Milošević, G. G. Paulus, and H. Walther, Adv. At., Mol., Opt. Phys. **48**, 35 (2002).

[12] Molecules in Laser Fields, edited by A.D. Bandrauk (M. Dekker, Publisher, NY, 1994);
Th. Ergler *et al.*, Phys. Rev. Lett. **95**, 093001 (2005);
D. Zeidler *et al.*, Phys. Rev. Lett. **95**, 203003 (2005);
A. S. Alnaser *et al.*, Phys. Rev. Lett. **93**, 183202 (2004);
H. Niikura *et al.*, *ibid.* **417**, 917 (2002);
T. Seideman, M. Yu. Ivanov, and P. B. Corkum, Phys. Rev. Lett. **75**, 2819 (1995).

[13] P. Agostini, F. Fabre, G. Mainfray, G. Petite and N. K. Rahman, Phys. Rev. Lett. **42**, 1127 (1979);
P. Kruit, J. Kimman, H. G. Muller and J. van der Wiel, Phys. Rev. A **28**, 248 (1983).
G. G. Paulus *et al.*, Phys. Rev. Lett. **91** 253004 (2003).

[14] M. Ferray *et al.*, J. Phys. B **21**, L31 (1988);
A. L'Huillier, K. J. Schafer and K. C. Kulander, J. Phys. B **24**, 3315 (1991);
A. L'Huillier and P. Balcou, Phys. Rev. Lett. **70**, 774 (1993).

[15] K. Kondo, A. Sagisaka, T. Tamida, Y. Nabekawa and S. Watanabe, Phys. Rev. A **48**, R2531 (1993);
D. N. Fittinghoff, P. R. Bolton, B. Chang and K. C.Kulander, Phys. Rev. Lett. **69**, 2642 (1992); Phys Rev. A **49**, 2174 (1994).
B. Feuerstein *et al.*, Phys. Rev. Lett. **87** 043003 (2001).

[16] J. Zanghellini, M. Kitzler, Z. Zhang and T. Brabec, J. Mod. Opt. **52**, 479 (2005).

[17] C. A. Ullrich and E. K. U. Gross, Comm. At. Mol. Opt. Phys. **33**, 211 (1997);
M. Petersilka and E. K. U. Gross, Laser Phys. **9**, 105 (1999).

[18] R. Panfili, J. H. Eberly und S. L. Haan, Opt. Expr. **8**, 431 (2001);
R. Panfili, S. L. Haan and J. H. Eberly, Phys. Rev. Lett. **89**, 113001 (2002);
P. J. Ho, R. Panfili, S. L. Haan and J. H. Eberly, Phys. Rev. Lett. **94**, 093002 (2005).

[19] R. M. Potvliege and R. Shakeshaft Phys. Rev. A **41** 1609 (1990).

[20] C. H. Keitel and S. X. Hu, Appl. Phys. Lett. **88**, 541 (2002).

[21] J. C. Solem and G. C. Baldwin, Science **218**, 229 (1982);
M. H. Vos and J.-L. Martin, Annu. Rev. Biophys. Biomol. Struct., **21**, 199 (1992);
K. Boyer, J. C. Solem, J. W. Longworth, A. B. Borisov, and C. K. Rhodes, Nat. Med. (N. Y.) **2**, 939 (1996);
C. Rose-Petruck *et al.*, Nature (London) **398**, 310 (1999).

[22] D. B. Bauer, D. B. Milošević and W. Becker, Phys. Rev. A 72, 023415 (2005);
M. Klaiber, K. Z. Hastsgortsyan and C. H. Keitel, Phys. Rev. A **73**, 053411 (2006).

[23] K. C. Kulander, Phys. Rev A **35** 445 (1987).

[24] P. B. Corkum, Phys. Rev. Lett. **71**, 1994 (1993).

[25] A. D. Bandrauk and H. Z. Lu, Phys. Rev. A **73**, 013412 (2006).

[26] R. Grobe and J. H. Eberly, Phys. Rev. A **48**, 4664 (1993).

[27] S. X. Hu and C. H. Keitel, Europhys. Lett. **47**, 318 (1999);
N. J. Kylstra, R. M. Potvliege, and C. J. Joachain, J. Phys. B **34**, L55 (2001);
J.R. Vázquez de Aldana and L. Roso, Phys. Rev. A **61**, 043403 (2000).

[28] G. R. Mocken and C.H. Keitel, Phys. Rev. Lett. **91**, 173202 (2003);
N. J. Kylstra, A. M. Ermolaev and C. J. Joachain, J. Phys. B **30** L449 (1997);
J. W. Braun, Q. Su and R. Grobe, Phys. Rev. A **59** 604 (1999);
U. W. Rathe, C. H. Keitel, M. Protopapas and P. L. Knight, J. Phys. B **30** L531 (1997).

[29] S. X. Hu and C. H. Keitel, Phys. Rev. A **63**, 053402 (2001).

[30] G. R. Mocken and C. H. Keitel, J. Phys. B **37**, L275 (2004);
C. C. Chirila, C. J. Joachain, N. J. Kylstra, and R. M. Potvliege, Phys. Rev. Lett. **93**, 243603 (2004).

[31] M. Klaiber, K. Z. Hatsagortsyan, and C. H. Keitel, Phys. Rev. A **74**, 051803(R) (2006).

[32] N. Milosevic, P. B. Corkum, and T. Brabec, Phys. Rev. Lett. **92**, 013002 (2004).

[33] B. Henrich, K. Z. Hatsagortsyan, and C. H. Keitel, Phys. Rev. Lett. **93**, 013601 (2004);
K. Z. Hatsagortsyan, C. Müller, and C. H. Keitel, Europhys. Lett. **76**, 29 (2006).

[34] F. V. Hartemann *et al.*, Phys. Rev. E **51** 4833 (1995);
Y. I. Salamin, F. H. M. Faisal, Phys. Rev. A **62** 053809 (2000).

[35] M. Verschl and C. H. Keitel, Laser Phys. **15**, 529 (2005);
S. X. Hu and C. H. Keitel, Europhys. Lett. **47**, 318 (1999).

[36] M. Protopapas, C. H. Keitel, and P. L. Knight, Rep. Prog. Phys. **60**, 389 (1997).

[37] Classical electrodynamics, J. D. Jackson, 2d. edition 1975 (John-Wiley&Sons, New York).

[38] B. Sundaram and P. W. Milonni,Phys. Rev. A **41** 6571 (1990).

[39] J. W. G. Tisch *et al.*, J. Phys. B **30**, L709 (1997).

[40] V. Averbukh, O. E. Alon and N. Moiseyev, Phys. Rev. A **60** 2585 (1999).

[41] D. B. Milošević, G. G. Paulus, D. Bauer and W. Becker, J. Phys. B **39** R203 (2006).

[42] M. Lewenstein, *et al.*, Phys. Rev. A **49**, 2117 (1994).

[43] C. C. Chirila and M. Lein, J. Phys. B **39**, S437 (2006);
M. Lein, Phys. Rev. Lett. **94**, 053004 (2005).

[44] M. W. Walser *et al.*, Phys. Rev. Lett. **85**, 5082 (2000).

[45] M. Lein *et al.*, Phys. Rev. A **66**, 023805 (2002).

[46] K. Z. Hatsagortsyan and C. H. Keitel, J. Phys. B **35**, L175 (2002);
see also: K. Z. Hatsagortsyan and C. H. Keitel, Phys. Rev. A **72**, 023812 (2005).

[47] T. W. B. Kibble, Phys. Rev. **138** B740 (1965).

[48] J. Javanainen, J.H. Eberly, and Q. Su, Phys. Rev. A **38**, 3430 (1988).

[49] J. Fleck, J. Morris, and M. Feit, Appl. Phys. **10**, 129 (1976); R.W. Heather, Comp. Phys. Comm. **63**, 446 (1991).

[50] A. D. Bandrauk, H. Shen, Chem. Phys. Lett. **176**, 428-432 (1991), J. Chem. Phys. **99**, 1185 (1993);
A.D. Bandrauk, E. Dehghanian, H. Z. Lu, Chem. Phys. Lett. **419**, 346 (2006).

[51] E. S. Smyth, J. S. Parker and K. T. Taylor, Comput. Phys. Commun. **114**, 1 (1998).

[52] see the *Numerical Recipes*: http://www.nr.com/

[53] K. Burnett *et al.*, Phys. Rev. A **45**, 3347 (1992);
T.-F. Jiang and S.-I. Chu, Phys. Rev. A **46**, 7322 (1992).

[54] M. D. Feit, J. A. Fleck, Jr. and A. Steiger, J. Comput. Phys. **47**, 412 (1982).

[55] R. Kosloff and H. Tal-Ezer, Chem. Phys. Lett. **127** 223 (1986).

[56] S. I. Chu and Y. R. Yin, J. Opt. Soc. Am. B **4** 720 (1987);
G. A. Kyrala, J. Opt. Soc. Am. B **4** 731 (1987);
M. Gajda et. al., Phys. Rev. A **46** 1638 (1992);
Keitel C H , J. Phys. B **29** L873 (1996);
H. Schmitz, K. Bouke and H. J. Kull, Phys. Rev. A **57** 467 (1998).

[57] H. R. Schwarz, Numerische Mathematik, B. G. Teubner Stuttgart (1997).

[58] C. Figueira de Morisson Faria and J.-M. Rost, Phys. Rev. A **62**, 051402(R) (2000).

[59] T. Zuo, A.D. Bandrauk, M. Ivanov, and P.B. Corkum, Phys. Rev. A **51**, 3991 (1995).

[60] J.-P. Connerade and C. H. Keitel, Phys. Rev. A **53**, 2748 (1996).

[61] Y. I. Salamin and F. H. M. Faisal, Phys. Rev. A **58**, 3221 (1998).

[62] R. E. Wagner, Q. Su and R. Grobe, Phys. Rev. A **60**, 3233 (1999);
R. E. Wagner, Q. Su and R. Grobe, Phys. Rev. Lett. **84**, 3282 (2000);
P. Krekora, R. E. Wagner, Q. Su and R. Grobe, Phys. Rev. A **63**, 25404 (2001);
R. E. Wagner, S. Radovich, J. Gillespie, Q. Su and R. Grobe, Phys. Rev. A **66**, 43412 (2002);
R. E. Wagner, Q. Su and R. Grobe, Laser Phys. **13**, 414 (2003).

[63] D. B. Milošević and A. F. Starace, Phys. Rev. Lett. **82**, 2653 (1999);
D. B. Milošević and A. F. Starace, Phys. Rev. A **60**, 3160 (1999).

[64] X. M. Tong and S. I. Chu, J. Phys. B **32**, 5593 (1999).

[65] R. M. Potvliege, N. J. Kylstra, and C. J. Joachain, J. Phys. B **33**, L743 (2000);
S. X. Hu and C. H. Keitel, Phys. Rev. A **63**, 53402 (2001).

[66] R. Fischer, C. H. Keitel, R. Jung, G. Pretzler, O. Willi, Phys. Rev. A **75**, 033401 (2007).

[67] T. Shinada *et al.*, Nature **437**, 1128 (2005);
Y. Shude *et al.*, Surface and Coatings **158**, 412 (2002);
M. Koh *et al.*, Appl. Phys. Lett. **68**, 1552 (1996).

[68] M. Motokawa, Rep. Prog. Phys. **67**, 1995 (2004).

[69] D. J. Urbach and C. H. Keitel, Phys. Rev. A **61**, 043409 (2000).

[70] J. B. Watson, A. Sanpera, K. Burnett, and P. L. Knight, Phys. Rev. A **55**, 1224 (1997);
J. B. Watson, A. Sanpera, and K. Burnett, Phys. Rev. A **51**, 1458 (1995).

[71] L. I. Schiff, *Quantum mechanics*, 3rd edition, McGraw-Hill (1968), p. 179.

[72] R. Fischer, M. Lein, and C. H. Keitel, Phys. Rev. Lett. **97**, 143901 (2006);
R. Fischer, M. Lein, and C. H. Keitel, J. Mod. Opt. *accepted* (2007)

[73] R. Fischer, M. Lein, C. H. Keitel, J. Phys. B **40**, F113(2007).

[74] T. Kanai, S. Minemoto, and H. Sakai, Nature **435**, 470 (2005);
H. Niikura *et al.*, Nature **417**, 917 (2002);
A. D. Bandrauk and H. Z. Lu, Phys. Rev. A **73**, 013412 (2006).

[75] R. Dörner, *et al.*, Adv. At., Mol., Opt. Phys. **48**, 1 (2002);
P. J. Ho, R. Panfili, S. L. Haan, and J. H. Eberly, Phys. Rev. Lett. **94**, 093002 (2005);
J. Prager and C. H. Keitel, J. Phys. B **35**, L167 (2002).

[76] D. B. Milošević, G. G. Paulus, D. Bauer, and W. Becker, J. Phys. B **39**, R203 (2006);
F. Lindner *et al.*, Phys. Rev. Lett. **95**, 040401 (2005);
G. G. Paulus, F. Zacher, H. Walther, A. Lohr, W. Becker, and M. Kleber, Phys. Rev. Lett. **80**, 484 (1998).

[77] J. Itatani *et al.*, Nature **432**, 867 (2004).

[78] M. Lein, N. Hay, R. Velotta, J.P. Marangos, and P.L. Knight, Phys. Rev. Lett. **88**, 183903 (2002);
M. Lein, N. Hay, R. Velotta, J.P. Marangos, and P.L. Knight, Phys. Rev. A **66**, 023805 (2002);
M. Lein, J.P. Marangos, and P.L. Knight, Phys. Rev. A **66**, 051404(R) (2002);
D. G. Lappas and J. P. Marangos, J. Phys. B **33**, 4679 (2000);
R. Velotta, N. Hay, M. B. Mason, M. Castillejo, and J. P. Marangos *et al.*, Phys. Rev. Lett. **87**, 183901 (2001);
C. Vozzi *et al.*, Phys. Rev. Lett. **95**, 153902 (2005).

[79] X. X. Zhou, X. M. Tong, Z. X. Zhao, and C. D. Lin, Phys. Rev. A **72**, 033412 (2005);
X. X. Zhou, X. M. Tong, Z. X. Zhao, and C. D. Lin, *ibid.* **71**, 061801(R) (2005);
B. Shan, S. Ghimire, and Z. Chang, *ibid.* **69**, 021404(R) (2004);
T. K. Kjeldsen, C. Z. Bisgaard, L. B. Madsen, and H. Stapelfeldt, Phys. Rev. A **68**, 063407 (2003);
M. Lein, J. Phys. B **36**, L155 (2003).

[80] H. Stapelfeldt and T. Seideman, Rev. Mod. Phys. **75**, 543 (2003);
F. Rosca-Pruna and M. J. J. Vrakking, J. Chem. Phys. **116**, 6567 (2002);
J. J. Larsen, K. Hald, N. Bjerre, H. Stapelfeldt, and T. Seideman *et al.*, Phys. Rev. Lett. **85**, 2470 (2000).

[81] M. Lein, Phys. Rev. Lett. **94**, 053004 (2005);
C. C. Chirila and M. Lein, J. Phys. B **39**, S437 (2006);
W. Qu, Z. Chen, Z. Xu, and C. H. Keitel, Phys. Rev. A **65**, 013402 (2001);
S. Baker *et al.*, Science **312**, 424 (2006).

Thanks

First of all, I would like to thank Christoph H. Keitel for both the opportunity to do this Ph.D. project at the MPIK and for supervision. I acknowledge the collaboration with the group of Prof. Willi from the university of Düsseldorf.

I am grateful to Manfred Lein for fruitful discussions.

I enjoyed the pleasant atmosphere in the Keitel group. For this I say "thank you" to all group members.

Special thanks go to my roommates Martin Haas, Mario Verschl, Martin Kiffner, Henrik Hetzheim and Peter Orth who provided a good atmosphere in our office and shared the same sense of humor with me.

I am especially grateful to Andreas Staudt for discussions and friendship since I have joined the group in Freiburg. Special thanks go also to Carsten Müller for friendship and table tennis practice. (I have really improved my table tennis a lot.)

I would like to thank Matthias Ruf and Stefan Pieper for exhilarating hours during the teaching period at the university.

Last but not least, I am grateful to David Stiff and Peter Brunner for the help with sometimes stupid computer problems. And thank you Peter for taking me so often down the hill with your car.

In this place, I would also like to express my gratitude to my parents who have supported me all the time.